ERROR ESTIMATION AND STABILIZATION FOR LOW ORDER FINITE ELEMENTS

A thesis submitted to the University of Manchester
for the degree of Doctor of Philosophy
in the Faculty of Engineering and Physical Sciences

2010

Qifeng Liao
School of Mathematics

Contents

Word count 17055

List of Tables

List of Figures

The University of Manchester

Qifeng Liao
Doctor of Philosophy
Error estimation and stabilization for low order finite elements
December 9, 2010

This thesis covers three topics—a posteriori error estimation, mixed finite element approximations for anisotropic meshes and the solution of the time-dependent Navier-Stokes equations using a stabilized $Q_1 - P_0$ approximation.

First, we find effective error estimators for (bi-)quadratic approximations for the diffusion problem, and (bi-)quadratic velocity and (bi-)linear pressure mixed approximations for incompressible flow problems. The efficiency and reliability of the error estimators are established in the case of the Stokes problem.

Second, since standard inf-sup stable mixed approximations typically become unstable for anisotropic meshes, we devote our attention to a stabilized $Q_1 - P_0$ approximation, which is introduced by Kechkar and Silvester [Math. Comp., 58, 1–10, 1992]. We establish a robust a priori error bound for this stabilized $Q_1 - P_0$ approximation for anisotropic meshes.

Finally, the stabilized $Q_1 - P_0$ approximation is applied to solving time dependent incompressible flow problems with an adaptive time stepping method introduced by Kay et al. [SIAM J. Sci. Comput., 32, 111–128, 2010]. The main contribution of this part is to find the optimal stabilization parameter, which is eventually shown to be inversely proportional to the Reynolds number of the flow.

Declaration

No portion of the work referred to in this thesis has been submitted in support of an application for another degree or qualification of this or any other university or other institute of learning.

Copyright Statement

i. The author of this thesis (including any appendices and/or schedules to this thesis) owns certain copyright or related rights in it (the "Copyright") and s/he has given The University of Manchester certain rights to use such Copyright, including for administrative purposes.

ii. Copies of this thesis, either in full or in extracts and whether in hard or electronic copy, may be made **only** in accordance with the Copyright, Designs and Patents Act 1988 (as amended) and regulations issued under it or, where appropriate, in accordance with licensing agreements which the University has from time to time. This page must form part of any such copies made.

iii. The ownership of certain Copyright, patents, designs, trade marks and other intellectual property (the "Intellectual Property") and any reproductions of copyright works in the thesis, for example graphs and tables ("Reproductions"), which may be described in this thesis, may not be owned by the author and may be owned by third parties. Such Intellectual Property and Reproductions cannot and must not be made available for use without the prior written permission of the owner(s) of the relevant Intellectual Property and/or Reproductions.

iv. Further information on the conditions under which disclosure, publication and commercialisation of this thesis, the Copyright and any Intellectual Property and/or Reproductions described in it may take place is available in the University IP Policy (see `http://www.campus.manchester.ac.uk/medialibrary/policies/intellectual-property.pdf`), in any relevant Thesis restriction declarations deposited in the University Library, The University Library's regulations (see `http://www.manchester.ac.uk/library/aboutus/regulations`) and in The University's policy on presentation of Theses.

Acknowledgements

First and foremost, I would like to express my most sincere thanks to my supervisor Prof. David Silvester, for his essential advice, guidance and patience throughout my three year PhD study. I also thank David for his essential help during my one year MSc course.

I am very grateful to my academic brother Gaurav Prinja, for his help both in study and daily life in Manchester.

A big thank for my parents and family for their continuous love and support.

Finally, I would like to formally acknowledge the financial support from the Secretary of State for Education and Science of the United Kingdom, and the School of Mathematics of the University of Manchester under the Overseas Research Studentship Award Scheme (ORSAS) during the last three years.

Chapter 1

Introduction

Since the 17th century, Newton (1643–1727) and Leibniz (1646–1716) created the world of modern mathematics by introducing calculus. With differentials in calculus, people started to think about differential equations. For instance, Newton's second law is a primary example. After that, lots of partial differential equation (PDE) models for different physics problems have been established by many great mathematicians. Two of these pioneers, Claude-Louis Navier (1785–1836) and George Stokes (1819–1903) contributed the fundamental equations for flow problems, which we now refer to as the Navier-Stokes equations.

There is no word to describe how important the Navier-Stokes equations are. These equations are the heart of many areas of science and technology. By accurately solving them, people can predict the weather, develop more efficient cars and aircraft, and even produce better medicines.

A crucial problem is how to accurately and efficiently solve the flow equations. Since PDEs can rarely be solved exactly, numerical schemes play an important role. There are typically three widely used numerical methods: finite differences, finite volumes and finite elements. Within these methods, the finite element method is the most robust, and has the most solid mathematical base—it is fully built on functional analysis which is one of the greatest mathematical achievements during the twentieth century. An increasing proportion of CFD (computational fluid mechanics) software utilizes this discretization approach, e.g. the commercial software COMSOL (COMSOL AB, http://www.comsol.com) and the free software OOMPH-LIB (http://oomph-lib.maths.man.ac.uk).

A number of different finite element methods have been developed for solving flow problems since the mid-20th century. However, the most widely used methods in practice are the low order methods—that are zero order (constant) approximations, (bi- or tri-)linear approximations and (bi- or tri-)quadratic approximations. This is because first, these low order elements are easy to implement; second, higher order approximations do not provide more accurate solutions when the exact solution is not regular enough (this is often the case in many practical problems). Due to these reasons, this thesis concentrates on low order elements.

Since finite element solutions are approximations of the exact solutions, there exist some errors. It is of interest to estimate these approximation errors. Generally speaking, there are two kinds of error estimation—a priori estimation and a posteriori estimation. The a priori error estimation typically gives convergence rates of finite element approximations before computing approximate solutions, but is not able to provide computable bounds for the errors. On the contrary, a posteriori estimation is processed after obtaining finite element solutions, and can provide computable bounds for the errors. This thesis will discuss both types of error estimation for low order approximations.

In the rest of Chapter 1, the mathematical setting of this thesis will be introduced with an example problem—the Stokes equations. After that, an outline of the thesis will be provided.

1.1 The Model Stokes Problem

In this section, we consider the model of viscous incompressible flow in an idealized, bounded, connected domain Ω in $\mathbb{R}^2$:

$$-\nabla^2\vec{u} + \nabla p = \vec{f} \quad \text{in} \quad \Omega, \tag{1.1}$$

$$\nabla \cdot \vec{u} = 0 \quad \text{in} \quad \Omega, \tag{1.2}$$

$$\vec{u} = \vec{g} \quad \text{on} \quad \partial\Omega_D, \tag{1.3}$$

$$\frac{\partial \vec{u}}{\partial n} - \vec{n}p = \vec{0} \quad \text{on} \quad \partial\Omega_N. \tag{1.4}$$

We assume that Ω has a polygonal boundary $\partial\Omega = \partial\Omega_D \cup \partial\Omega_N$, $\partial\Omega_D \cap \partial\Omega_N = \emptyset$, so that $\vec{n}$ is the usual outward-pointing normal vector and $\partial\vec{u}/\partial n$ is the directional derivative in the $\vec{n}$ direction. The vector field $\vec{u}$ is the velocity of the flow and the scalar variable p represents the pressure. If $\partial\Omega_N = \emptyset$, the flow problem models enclosed flow.

1.2 Function Spaces

1.2.1 Sobolev spaces

First, the space of continuous functions from Ω to real numbers is denoted by $C^0(\Omega)$. Next, $L^2(\Omega)$ is the space of functions which are square integrable over Ω in the sense of Lebesgue integration,

$$L^2(\Omega) := \left\{u : \Omega \to \mathbb{R}, \int_\Omega u^2 \, d\Omega < \infty\right\}. \tag{1.5}$$

The space $L^2(\Omega)$ is a Hilbert space, equipped with the inner product

$$(u, v) := \int_\Omega uv \, d\Omega, \tag{1.6}$$

and the associated norm

$$||u||_0 := (u, u)^{\frac{1}{2}}. \tag{1.7}$$

Moreover, $L_0^2(\Omega)$ is the factor space:

$$L_0^2(\Omega) := \left\{u \middle| u \in L^2(\Omega) \quad \text{and} \quad \int_\Omega u \, d\Omega = 0\right\}. \tag{1.8}$$

Then, we define the vector function space $L^2(\Omega)^2$,

$$L^2(\Omega)^2 := \left\{\vec{q} \mid q_i \in L^2(\Omega), i = 1 : 2\right\},$$

where $\vec{q} = (q_1, q_2)$. The inner product of $L^2(\Omega)^2$ is defined by

$$(\vec{p}, \vec{q}) = \int_\Omega \vec{p} \cdot \vec{q} \, d\Omega = \sum_{i=1}^{2} \int_\Omega p_i q_i \, d\Omega,$$

and the associated norm is also denoted by $|| \cdot ||_0$.

Given an integer $k \geq 0$ (i.e. $k \in \mathbb{N}_0$), we define the Sobolev space

$$H^k(\Omega) := \left\{ v | \, D^m v \in L^2(\Omega), m \in \mathbb{N}_0 \text{ and } 0 \leq m \leq k \right\},$$

where the operator D^m is

$$D^m v = \frac{\partial^m v}{\partial x^{m_1} \partial y^{m_2}}, \quad m_1, m_2 \in \mathbb{N}_0 \text{ and } m = m_1 + m_2. \tag{1.9}$$

The semi-norm and norm of $H^k(\Omega)$ are

$$|v|_k = \left(\sum_{m=k} \|D^m v\|_0^2 \right)^{\frac{1}{2}}, \quad \|v\|_k = \left(\sum_{k' \leq k} |v|_{k'}^2 \right)^{\frac{1}{2}}.$$

Note that in the notation of the above inner product and (semi-)norms, the integration domain Ω is ignored. However, if the integration area is some other area (e.g. ω) rather than the domain Ω, the inner product and norms are denoted by $(\cdot,\cdot)_\omega$, $\|\cdot,\cdot\|_{k,\omega}$ and $|\cdot,\cdot|_{k,\omega}$.

In addition, for a vector $\alpha = (\alpha_1, \alpha_2) \in \mathbb{N}_0^2$, the associated differential operator D^α is

$$D^\alpha(\cdot) = \frac{\partial^{\alpha_1}(\cdot)}{\partial x^{\alpha_1}} \frac{\partial^{\alpha_2}(\cdot)}{\partial y^{\alpha_2}}. \tag{1.10}$$

Analogously to the definition of $L^2(\Omega)^2$, the space $H^k(\Omega)^2$ is defined. For any vector function $\vec{v} = (v_1, v_2) \in H^k(\Omega)^2$, the operators D^m and D^α are defined as

$$D^m \vec{v} = (D^m v_1, D^m v_2); \quad D^\alpha \vec{v} = (D^\alpha v_1, D^\alpha v_2). \tag{1.11}$$

Finally, for the Dirichlet boundary $\partial\Omega_D$,

$$H^{1/2}(\partial\Omega_D)^2 := \left\{ \vec{v} \;\middle|\; \vec{v} = \vec{u}|_{\partial\Omega_D}, \; \vec{u} \in H^1(\Omega)^2 \right\}. \tag{1.12}$$

The boundary data $\vec{g}$ in (1.3) is assumed to be in the space $H^{1/2}(\partial\Omega_D)^2$.

1.2.2 Solution and test spaces

For simplicity, the two dimensional vector function spaces are denoted by

$$\boldsymbol{H}^k := H^k(\Omega)^2 \quad \forall k \in \mathbb{N}_0. \tag{1.13}$$

The velocity solution and test spaces are

$$\boldsymbol{H}_E^1 := \left\{ \vec{u} \in \boldsymbol{H}^1 \middle| \quad \vec{u} = \vec{g} \quad \text{on} \quad \partial\Omega_D \right\}, \tag{1.14}$$

$$\boldsymbol{H}_{E_0}^1 := \left\{ \vec{v} \in \boldsymbol{H}^1 \middle| \quad \vec{v} = \vec{0} \quad \text{on} \quad \partial\Omega_D \right\}. \tag{1.15}$$

In addition, the dual space $\boldsymbol{H}^{-1}$ is defined by

$$\boldsymbol{H}^{-1} := \left\{ \vec{u} \;\middle|\; \int_{\Omega} \vec{u} \cdot \vec{v} \, d\Omega < \infty, \ \forall \vec{v} \in \boldsymbol{H}^{1}_{E_0} \right\}. \tag{1.16}$$

The function $\vec{f}$ on the right hand side of (1.1) is assumed to be in $\boldsymbol{H}^{-1}$.

Lastly, the pressure space $\boldsymbol{P}$ is

$$\boldsymbol{P} = \begin{cases} L^2(\Omega) & \text{when } \int_{\Omega_N} ds > 0\,, \\ L^2_0(\Omega) & \text{when } \int_{\Omega_N} ds = 0\,. \end{cases} \tag{1.17}$$

1.3 Weak Formulation

The weak formulation of (1.1)–(1.4) is: find $\vec{u} \in \boldsymbol{H}^1_E$ and $p \in \boldsymbol{P}$ such that

$$\int_{\Omega} \nabla \vec{u} : \nabla \vec{v} - \int_{\Omega} p \nabla \cdot \vec{v} = \int_{\Omega} \vec{f} \cdot \vec{v} \quad \forall \vec{v} \in \boldsymbol{H}^1_{E_0}, \tag{1.18}$$

$$\int_{\Omega} q \nabla \cdot \vec{u} = 0 \qquad \forall q \in \boldsymbol{P}. \tag{1.19}$$

As is well known, see Girault & Raviart [24, pp. 59–61], a sufficient condition for the existence and uniqueness of a solution satisfying (1.18)–(1.19) is the continuous inf-sup condition that is stated below.

Definition 1.3.1 *Continuous inf-sup condition: there exists a positive constant γ dependent on the shape of the domain Ω such that,*

$$\inf_{0 \neq q \in \boldsymbol{P}} \sup_{\vec{0} \neq \vec{v} \in \boldsymbol{H}^1_{E_0}} \frac{|(q, \nabla \cdot \vec{v})|}{|\vec{v}|_1 \, \|q\|_0} \geq \gamma. \tag{1.20}$$

In the sequel, this continuous inf-sup condition will be assumed to be satisfied. To the author's knowledge, establishing this continuous inf-sup condition for an arbitrary domain Ω with a natural outflow condition (1.4) is an open problem. For enclosed flow problems there are some theoretical results for special domain types. For example, Chizhonkov and Olshanskii [15] prove that, for a channel domain, the continuous inf-sup constant γ decreases in proportion to the length of the channel. Herein, we assume that the domain Ω is fixed, so the degeneration of the continuous inf-sup constant is not an issue.

1.4 Notation for Meshes

1.4.1 Mesh structure

This thesis only concentrates on rectangular partitionings, except Chapter 2 where triangular partitionings are also considered. Note that, although we only consider domains Ω which are a union of rectangles throughout this thesis for simplicity, most of our results can be generalized to more general domains with quadrilateral or triangular partitions. A rectangular mesh is denoted by T_h. Any rectangle T in T_h is an open set and $\overline{T}$ is used to denote its closure. The mesh T_h is assumed to be regular, which implies that for two different rectangles T_1 and T_2 in T_h, $\overline{T}_1 \cap \overline{T}_2$ is either a common edge, a common vertex or an empty set.

As usual, $\mathcal{E}_h$ is used to denote the set of element edges of T_h. Then, $\mathcal{E}_{h,\Omega}$ is the set of element edges inside of Ω, $\mathcal{E}_{h,D}$ is the set of element edges on the boundary $\partial\Omega_D$ and $\mathcal{E}_{h,N}$ is the set of element edges on the boundary $\partial\Omega_N$. So, $\mathcal{E}_h = \mathcal{E}_{h,\Omega} \cup \mathcal{E}_{h,D} \cup \mathcal{E}_{h,N}$. For an element $T \in T_h$, $\mathcal{E}(T)$ is the set of edges of T, $\mathbf{N}(T)$ is the set of vertices of T. Also, for an edge $E \in \mathcal{E}_h$, $\mathbf{N}(E)$ is the set of vertices of E.

For any $T \in T_h$ and $E \in \mathcal{E}_h$, the following local patches are defined,

$$\overline{\omega}_T = \cup_{\mathcal{E}(T)\cap\mathcal{E}(T')\neq\emptyset}\overline{T'}, \quad T' \in T_h; \tag{1.21}$$

$$\overline{\tilde{\omega}}_T = \cup_{\mathbf{N}(T)\cap\mathbf{N}(T')\neq\emptyset}\overline{T'}, \quad T' \in T_h; \tag{1.22}$$

$$\overline{\omega}_E = \cup_{E\in\mathcal{E}(T')}\overline{T'}, \quad T' \in T_h; \tag{1.23}$$

$$\overline{\tilde{\omega}}_E = \cup_{\mathbf{N}(E)\cap\mathbf{N}(T')\neq\emptyset}\overline{T'}, \quad T' \in T_h. \tag{1.24}$$

Then,

$$\omega_T = \overline{\omega}_T \setminus \partial\overline{\omega}_T,\ \tilde{\omega}_T = \overline{\tilde{\omega}}_T \setminus \partial\overline{\tilde{\omega}}_T, \omega_E = \overline{\omega}_E \setminus \partial\overline{\omega}_E,\ \tilde{\omega}_E = \overline{\tilde{\omega}}_E \setminus \partial\overline{\tilde{\omega}}_E. \tag{1.25}$$

Note that for any area $\omega \subset \mathbb{R}^2$, $\partial\omega$ is the boundary of ω.

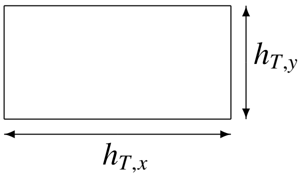

Figure 1.1: Element edge lengths: $h_{T,x}$ and $h_{T,y}$.

1.4.2 Mesh measurement

For a rectangle T in T_h, its edge lengths are measured by $h_{T,x}$ and $h_{T,y}$ (see Fig. 1.1). The element size of T is then measured by

$$h_{T,min} := \min(h_{T,x}, h_{T,y}), \tag{1.26}$$

$$h_{T,max} := \max(h_{T,x}, h_{T,y}), \tag{1.27}$$

and the global mesh size is

$$h := \max_{T \in T_h}(h_{T,max}). \tag{1.28}$$

In addition, without considering directions, $h_{T,E}$ is used to denote the length of $E \in \mathcal{E}(T)$ and $h_{T,E}^{\perp}$ is the length of the edge $E^{\perp} \in \mathcal{E}(T)$ where $E^{\perp}$ is perpendicular to E. For simplicity, without referring to elements, h_E is the length of an edge $E \in \mathcal{E}_h$.

Next, the aspect ratio of an rectangle T is

$$\rho_T := \frac{h_{T,max}}{h_{T,min}}, \tag{1.29}$$

whereas the global aspect ratio of T_h is

$$\rho := \max_{T \in T_h}(\rho_T). \tag{1.30}$$

Finally, the local grading factor κ_T and the global grading factor κ are defined by

$$\begin{aligned} \kappa_T &:= \max_{T' \subset \tilde{\omega}_T}\left(\max\left(\frac{h_{T',x}}{h_{T,x}}, \frac{h_{T,x}}{h_{T',x}}, \frac{h_{T',y}}{h_{T,y}}, \frac{h_{T,y}}{h_{T',y}}\right)\right), && (1.31) \\ \kappa &:= \max_{T \in T_h}(\kappa_T). && (1.32) \end{aligned}$$

For ρ and κ, it is easy to obtain the following inequality,

$$\kappa \leq \rho^2. \tag{1.33}$$

So, if a mesh is isotropic (its global aspect ratio ρ is a moderate constant), its global grading factor κ can not be large. However, the converse does not hold.

1.5 Mixed Finite Element Approximation

Mixed finite element approximations of (1.18)–(1.19) are obtained by taking finite dimensional subspaces X_E^h to approximate $\boldsymbol{H}_E^1$, X_0^h to approximate $\boldsymbol{H}_{E_0}^1$ and M^h to approximate $\boldsymbol{P}$. Then, the Galerkin formulation is: find $\vec{u}_h \in X_E^h$ and $p_h \in M^h$ such that,

$$\int_\Omega \nabla\vec{u}_h : \nabla\vec{v}_h - \int_\Omega p_h \nabla\cdot\vec{v}_h = \int_\Omega \vec{f}\cdot\vec{v}_h \quad \forall\vec{v}_h \in X_0^h, \tag{1.34}$$

$$\int_\Omega q_h \nabla\cdot\vec{u}_h = 0 \quad \forall q_h \in M^h. \tag{1.35}$$

We denote the basis functions of the space X_E^h by $\vec{\phi}_j,\ j = 1 : n_u + n_\partial$, such that

$$X_E^h = \left(\vec{u} \;\middle|\; \vec{u} = \sum_{j=1}^{n_u} a_j\vec{\phi}_j + \sum_{j=n_u+1}^{n_u+n_\partial} a_j\vec{\phi}_j,\ j\in\mathbb{R} \right), \tag{1.36}$$

where $X_0^h = \text{span}\{\phi_j\}_{j=1}^{n_u}$ and the additional coefficients $a_j : j = n_u+1,\ldots,n_u+n_\partial$ are associated with the Lagrange interpolation of the boundary data $\vec{g}$ on $\partial\Omega_D$. Collecting the coefficients $\{a_j\}_{j=1}^{n_u}$ into a vector $\mathbf{u}$ and associating a vector $\mathbf{p} \in \mathbb{R}^{n_p}$ with the coefficients in the expansion of p_h leads to a characteristic system of algebraic equations:

$$\begin{bmatrix} A & B^T \\ B & 0 \end{bmatrix} \begin{bmatrix} \mathbf{u} \\ \mathbf{p} \end{bmatrix} = \begin{bmatrix} \mathbf{f} \\ \mathbf{g} \end{bmatrix}. \tag{1.37}$$

In this thesis, we consider four typical low order finite element approximations associated with the rectangular mesh T_h: $\boldsymbol{Q}_2-\boldsymbol{Q}_1$, $\boldsymbol{Q}_2-\boldsymbol{P}_{-1}$, $\boldsymbol{Q}_2-\boldsymbol{P}_0$ and $\boldsymbol{Q}_1-\boldsymbol{P}_0$. In order to introduce these approximations, the polynomial spaces defined on a rectangle $T \in T_h$ are first defined as follows: $\boldsymbol{Q}_k(T)$ is the set of polynomials of maximal degree at most k and $\boldsymbol{P}_{-k}(T)$ ("–" implies the corresponding global functions may be discontinuous across element interfaces) is the set of polynomials of total degree at most k. As well, $\boldsymbol{Q}_k(T)^2$ is the set of vector functions whose components are in $\boldsymbol{Q}_k(T)$. Then the $\boldsymbol{Q}_1-\boldsymbol{P}_0$ approximation is associated with the following choices for X_0^h and M^h,

$$X_0^h = \left\{\vec{v}_h : \vec{v}_h|_T \in \boldsymbol{Q}_1(T)^2, \forall T \in T_h\right\} \cap \boldsymbol{H}_0^1, \tag{1.38}$$

$$M^h = \{q_h : q_h|_T \in \boldsymbol{P}_0(T), \forall T \in T_h\} \cap \boldsymbol{P}. \tag{1.39}$$

The other approximation methods are defined similarly. Fig. 1.2 shows the degrees of freedom for these low order elements.

Q_1 element Q_2 element

P_0 element P_{-1} element

Figure 1.2: Degrees of freedom for low order rectangular elements (→ and ↑ imply the x and y derivatives).

Analogously to the continuous situation, a sufficient condition for the unique solvability of the "saddle-point" system (1.37) is a (discrete–) inf-sup condition.

Definition 1.5.1 (Discrete inf-sup condition). *A mixed approximation $X_0^h \times M^h$ is inf-sup stable if*

$$\min_{0 \neq q_h \in M^h} \max_{\vec{0} \neq \vec{v}_h \in X_0^h} \frac{|(q_h, \nabla \cdot \vec{v}_h)|}{|\vec{v}_h|_1 \, \|q_h\|_0} = \gamma_h > 0 \tag{1.40}$$

where γ_h may depend on the mesh T_h and it is called the inf-sup constant.

As discussed in [21, section 5.5], the discrete inf-sup condition is equivalent to an algebraic problem. First, consider the following generalized eigenvalue problem,

$$BA^{-1}B^T \mathrm{x} = \lambda Q \mathrm{x}, \tag{1.41}$$

where the matrices B, A are those given in (1.37), and Q is the Grammian matrix associated with the basis functions spanning the pressure approximation space M^h. Arrange the eigenvalues of (1.41) as

$$\lambda_{n_p} \geq \lambda_{n_p - 1} \geq \ldots \geq \lambda_2 \geq \lambda_1 \geq 0. \tag{1.42}$$

Then γ_h in (1.40) satisfies

$$\gamma_h = \begin{cases} \sqrt{\lambda_2} & \text{if } \partial\Omega_N = \emptyset, \\ \sqrt{\lambda_1} & \text{if } \partial\Omega_N \neq \emptyset. \end{cases} \tag{1.43}$$

By computing the inf-sup constant γ_h, we can verify that $\boldsymbol{Q}_2 - \boldsymbol{Q}_1$, $\boldsymbol{Q}_2 - \boldsymbol{P}_{-1}$ and $\boldsymbol{Q}_2 - \boldsymbol{P}_0$ are inf-sup stable, whereas $\boldsymbol{Q}_1 - \boldsymbol{P}_0$ is unstable, since we found that $\lambda_2 = 0$ when $\partial\Omega_N = \emptyset$.

Any inf-sup stable method has the following a priori error estimate (see [21, p.253]):

$$||\vec{u} - \vec{u}_h||_1 + ||p - p_h||_0 \leq \tilde{C} \left(\inf_{\vec{v}_h \in X_E^h} ||\vec{u} - \vec{v}_h||_1 + \inf_{q_h \in M^h} ||p - q_h||_0 \right), \tag{1.44}$$

where $\tilde{C} = O(\frac{1}{\gamma_h})$. So, the bound (1.44) is not so useful, if γ_h degenerates.

In order to make progress, the rectangular meshes will be grouped into different families. For a specific inf-sup stable approximation, its inf-sup constant can be bounded below by some positive constant for some families, e.g. the family of isotropic meshes (ρ is bounded by some moderate constant). Then, the accuracy of the approximation is guaranteed for these mesh families. However, for mesh families including anisotropic meshes, the inf-sup constant often degenerates—a more detailed study is given in Chapter 4.

In the subsequent chapters, for simplicity, “bounded below” will be used instead of “bounded below by some positive constant”. Moreover, an approximation is said to be stable for some mesh families, if its inf-sup constant is bounded below for these families.

1.6 Outline of Thesis

Chapter 2 focusses on a posteriori error estimation for the diffusion problem. The methodology of local problem error estimation will be studied. The novel contribution of Chapter 2 is the development of effective error estimators for (bi-)quadratic elements.

Chapter 3 discusses a posteriori error estimation for the Stokes problem and the contents of this chapter have appeared in [32]. The strategy herein is still based on solving local problems. This chapter focusses on the inf-sup stable methods, e.g. the $\boldsymbol{Q}_2 - \boldsymbol{P}_{-1}$ and $\boldsymbol{Q}_2 - \boldsymbol{Q}_1$ approximations. The efficiency and reliability of the local problem estimators for these approximations will first be proven. Numerical results will suggest these error estimators are effective.

Chapter 4 studies the stability of the mixed approximations for anisotropic meshes. First some inf-sup stable methods will be discussed. Their inf-sup constants can degenerate as the mesh becomes anisotropic and then the constant $\tilde{C}$ in (1.44) may become very large. As a result, solution accuracy can not be guaranteed. Due to this reason, a local jump stabilized $\boldsymbol{Q}_1 - \boldsymbol{P}_0$ approximation introduced by Kechkar and Silvester[31] will be studied. The novel contribution of this chapter is the derivation of robust a priori error estimation for this stabilized method, which implies this method can work efficiently for anisotropic meshes. Finally, a posteriori error estimation for the stabilized $\boldsymbol{Q}_1 - \boldsymbol{P}_0$ method associated with anisotropic meshes will be discussed.

In Chapter 5, the stabilized $\boldsymbol{Q}_1 - \boldsymbol{P}_0$ method is used to solve two practical problems: the first problem is flow in a step domain and the second one is flow around a square cylinder in a channel. The focus is then switched to the time dependent Navier-Stokes equations in the case of small viscosity. The novel contribution of Chapter 5 is the identification of an optimal stabilization parameter, which is eventually shown to be independent of the time step and inversely proportional to the Reynolds number of the flow.

Finally, some open questions will be addressed in Chapter 6. Some MATLAB functions arising from this thesis will be introduced in Appendix A.

Chapter 2

A Posteriori Error Estimation for the Diffusion Problem

2.1 Introduction

In this chapter, effective a posteriori error estimators for (bi-)linear and (bi-)quadratic finite element approximations for the diffusion problem are presented. These error estimators are based on solving local problems—a methodology that was introduced by Bank and Weiser [6]. Generally speaking, local problem error estimators are quite accurate compared with other error estimators (e.g. standard widely used residual error estimators), since they are directly derived from error equations (see Section 2.1.2). However, most of the recent literature (e.g. Verfürth [47] and Elman et al. [21, pp.48–56]) on local problem error estimators only focusses on (bi-)linear approximations, whereas the effectivity of this kind of error estimators for (bi-)quadratic elements is unclear even for the simple diffusion problem. In addition, whilst Verfürth [46] theoretically establishes some local problem estimators for higher order elements, there are no numerical results to show their effectivity.

Moreover, we are interested in a posteriori error estimation for mixed approximations for incompressible flow problems. Standard inf-sup stable methods usually need (bi-)quadratic approximations for the velocity. Thus, effective local problem error estimators for (bi-)quadratic elements need to be established first, so that this error estimation strategy can then be applied when dealing with inf-sup stable mixed approximations. This will be discussed in detail in Chapter 3.

2.1.1 The diffusion problem

The Poisson equation modeling diffusion in two dimensions is,

$$-\nabla^2 u = f \quad \text{in} \quad \Omega, \tag{2.1}$$

$$u = g \quad \text{on} \quad \partial\Omega, \tag{2.2}$$

where the unknown function u typically denotes a temperature and f is a heat source.

The standard weak formulation of (2.1)–(2.2) is: find $u \in H^1_E(\Omega)$, such that

$$\int_\Omega \nabla u \cdot \nabla v = \int_\Omega f v \quad \forall v \in H^1_0(\Omega), \tag{2.3}$$

where the spaces $H^1_E(\Omega)$ and $H^1_0(\Omega)$ are

$$H^1_E(\Omega) := \left\{ u \in H^1(\Omega) \middle| \quad u = g \quad \text{on} \quad \partial\Omega \right\}, \tag{2.4}$$

$$H^1_0(\Omega) := \left\{ u \in H^1(\Omega) \middle| \quad u = 0 \quad \text{on} \quad \partial\Omega \right\}. \tag{2.5}$$

The standard Galerkin finite element method is: find $u_h \in X^h_E \subset H^1_E(\Omega)$, such that

$$\int_\Omega \nabla u_h \cdot \nabla v_h = \int_\Omega f v_h \quad \forall v_h \in X^h_0 \subset H^1_0(\Omega),$$

where X^h_E and X^h_0 are finite dimensional spaces.

This chapter focusses on a posteriori error estimation for the lowest order conforming finite element approximations; which are the linear element $\boldsymbol{P}_1$, the bilinear element $\boldsymbol{Q}_1$, the quadratic element $\boldsymbol{P}_2$ and the biquadratic element $\boldsymbol{Q}_2$. Fig. 2.1 shows the degrees of freedom of these elements.

2.1.2 Error estimation based on solving local problems

Subtracting $\int_\Omega \nabla u_h \cdot \nabla v$ from both sides of (2.3), the error ($e = u - u_h$) then satisfies the following error equation,

$$\int_\Omega \nabla e \cdot \nabla v = \int_\Omega f v - \int_\Omega \nabla u_h \cdot \nabla v \quad \forall v \in H^1_0(\Omega). \tag{2.6}$$

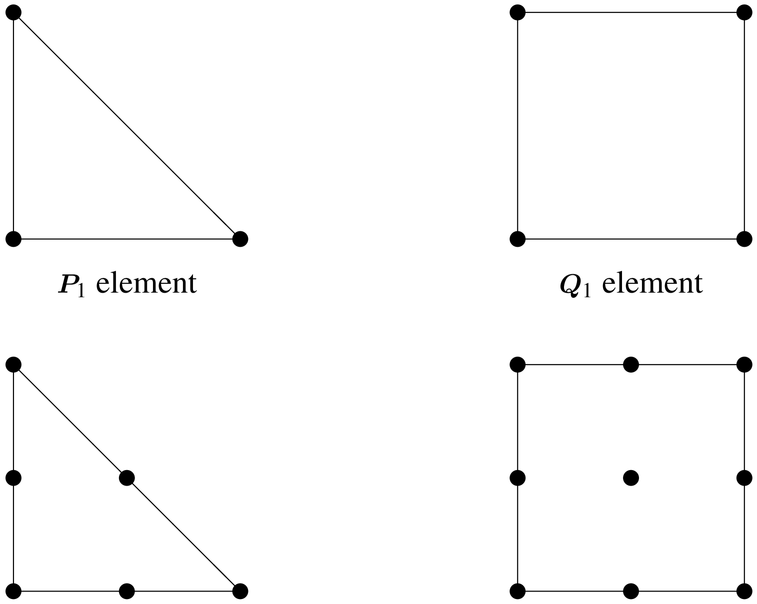

P_1 element Q_1 element

P_2 element Q_2 element

Figure 2.1: (Bi)-linear and (bi-)quadratic elements.

Integrating by parts for the second term on the right hand side of (2.6) and breaking the integrals into element contributions, the error then satisfies

$$\sum_{T\in T_h}(\nabla e,\nabla v)_T=\sum_{T\in T_h}\left[(f+\nabla^2 u_h,v)_T-\frac{1}{2}\sum_{E\in\mathcal{E}(T)}\left\langle\left\llbracket\frac{\partial u_h}{\partial n}\right\rrbracket,v\right\rangle_E\right],\tag{2.7}$$

where $\left\llbracket\frac{\partial u_h}{\partial n}\right\rrbracket$ is the flux jump which is defined in [21, p.49]—that is for an edge E shared by elements T and S,

$$\left\llbracket\frac{\partial u_h}{\partial n}\right\rrbracket:=(\nabla u_h|_T-\nabla u_h|_S)\cdot\vec{n}_{E,T}=(\nabla u_h|_S-\nabla u_h|_T)\cdot\vec{n}_{E,S}\,.\tag{2.8}$$

If the edge E is on the boundary, the flux jump is set to zero.

Next, the error equation (2.7) can be localized as

$$(\nabla e_T,\nabla v)_T=(R_T,v)_T-\sum_{E\in\mathcal{E}(T)}\langle R_E,v\rangle_E\,,\tag{2.9}$$

where

$$R_T=f+\nabla^2 u_h,\quad R_E=\frac{1}{2}\left\llbracket\frac{\partial u_h}{\partial n}\right\rrbracket.\tag{2.10}$$

Note that e_T in (2.9) is stronger than e in (2.7), since e_T automatically satisfies (2.7) while e does not need to satisfy (2.9) on each element. Thus, the error e can be approximated by solving the localized error equation (2.9) using proper finite element schemes. This methodology for estimating errors was introduced in [6].

The formal definition of the local problem error estimation strategy is: choose a suitable finite element space $\mathbb{Q}_T$ which is also called the *correction space* or the *error element*, and then find $e_h \in \mathbb{Q}_T$, such that

$$(\nabla e_h, \nabla v_h)_T = (R_T, v_h)_T - \sum_{E \in \mathcal{E}(T)} \langle R_E, v_h \rangle_E \qquad \forall v_h \in \mathbb{Q}_T. \tag{2.11}$$

The correction space $\mathbb{Q}_T$ should satisfy two requirements:

- $\mathbb{Q}_T$ must be "larger" than the original approximation space X_0^h;
- $\mathbb{Q}_T$ should make the problem (2.11) uniquely solvable—that is appropriate boundary conditions must be built into its definition.

Remark 2.1.1 The reason for these two requirements needs to be clarified. First, if $\mathbb{Q}_T$ is a subspace[1] of X_0^h, then the right hand side of (2.11) may be zero. As a result, the estimated error $||\nabla e_h||_{0,T}$ can be zero, even though the exact error may be large. Next, since the problem (2.11) is a diffusion problem with a pure Neumann boundary condition, its solution is only unique up to a constant. Thus, a Dirichlet boundary condition is needed to guarantee the uniqueness of the solution of (2.11). How to apply a proper Dirichlet boundary condition is a key issue of this chapter.

At this point, some notation is required,

$$\eta_{\bullet,T} = ||\nabla e_h||_{0,T} \quad \text{and} \quad \eta_\bullet = ||\nabla e_h||_{0,\Omega}, \tag{2.12}$$

where $\bullet$ stands for different choices of $\mathbb{Q}_T$. For instance, if the $\boldsymbol{P}_2$ approximation is used to compute the error (i.e. $\mathbb{Q}_T = \boldsymbol{P}_2$ in (2.11)), the corresponding element contribution and the global estimation of the error are denoted by

$$\eta_{P_2,T} = ||\nabla e_h||_{0,T} \quad \text{and} \quad \eta_{P_2} = ||\nabla e_h||_{0,\Omega}. \tag{2.13}$$

---

[1] More precisely, this means $\mathbb{Q} \subset X_0^h|_T := \{v' \mid v' = v|_T, \ \forall v \in X_0^h\}$.

To be efficient and reliable, an error estimator needs to satisfy the following two inequalities,

$$||\nabla e||_0 \leq C\eta_\bullet, \tag{2.14}$$

$$\eta_{\bullet,T} \leq c||\nabla e||_{0,\omega_T}, \tag{2.15}$$

where C and c are two generic constants independent of the exact solution and meshes, and the local patch ω_T is defined in Section 1.4.1.

Definition 2.1.2 (Effectivity). *The effectivity of an error estimator is the ratio* $\frac{\eta_\bullet}{||\nabla e||_0}$.

An error estimator is said to be effective in the subsequent sections, if its effectivity is close to one. In addition, the element contribution $\eta_{\bullet,T}$ of an effective error estimator is expected to be similar to $||\nabla e||_{0,T}$.

Remark 2.1.3 From a mathematical point of view, if the generic constants C and c in (2.14)–(2.15) can be accurately evaluated, a tight bound on the effectivity can be estimated. However, this is quite tricky—a lot of equivalences between different norms are necessarily required in standard analysis techniques (they will be discussed in Section 2.2), which leads to a number of unknown constants. Thus, the effectivity of error estimators may only be able to be examined numerically.

2.1.3 Test problem 1

In order to test the effectivity of error estimators, a simple example with the following exact solution

$$u = -(x^4 + y^4), \tag{2.16}$$

will be tested in subsequent sections. The domain for test problem 1 is the square $(-1, 1)^2$. In Fig. 2.2, the initial and refined rectangular and triangular meshes are shown. In this chapter, only uniform refinement is considered, where each element is equally subdivided into four.

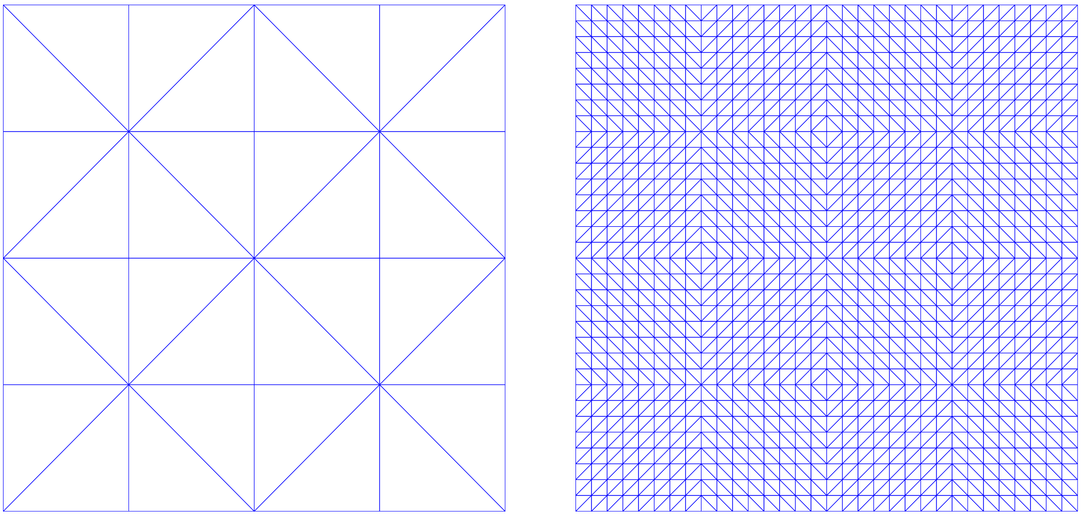

(a) The initial triangular mesh (b) Triangular mesh, refinement level three

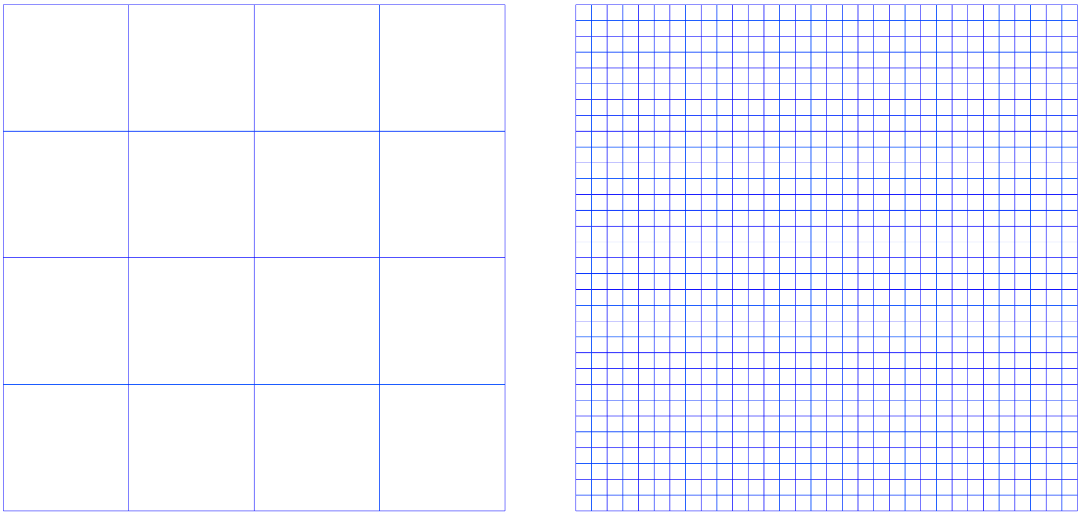

(c) The initial rectangular mesh (d) Rectangular mesh, refinement level three

Figure 2.2: Meshes for test problem 1.

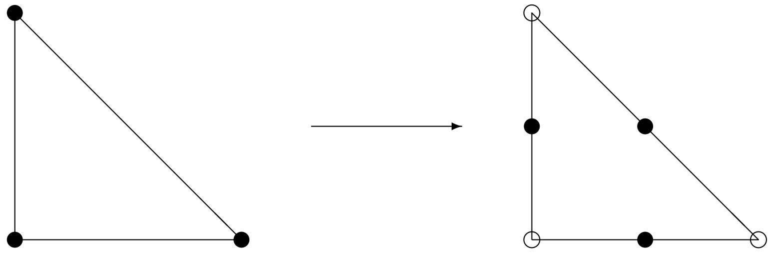

$\boldsymbol{P}_1$ element $\boldsymbol{P}_2$ error element

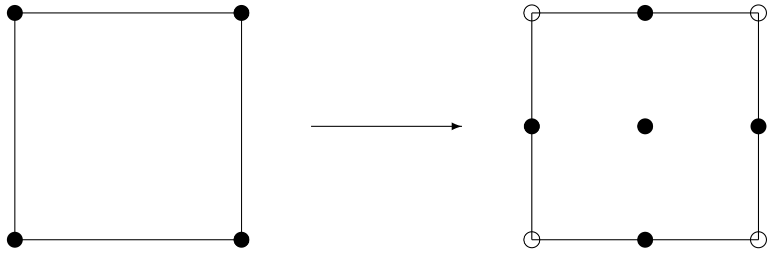

$\boldsymbol{Q}_1$ element $\boldsymbol{Q}_2$ error element

Figure 2.3: Error elements for the $\boldsymbol{P}_1$ and $\boldsymbol{Q}_1$ approximations (the empty circles imply these basis functions are removed).

2.2 Error Estimators for (Bi-)linear Elements

As discussed in [21, pp.48–56], for the linear element $\boldsymbol{P}_1$ and the bilinear element $\boldsymbol{Q}_1$, the corresponding correction spaces are the quadratic element $\boldsymbol{P}_2$ and the biquadratic element $\boldsymbol{Q}_2$ with the vertex nodes removed (the error estimators associated with them are called the $\boldsymbol{P}_2$ and $\boldsymbol{Q}_2$ estimators[2]). Fig. 2.3 shows these error elements, in which the removed nodes imply that zero boundary values are applied at these points.

The motivation for applying these Dirichlet boundary conditions for the error elements needs to be discussed. Roughly speaking, a linear finite element approximation implies that the numerical solution u_h is a linear interpolant of the exact solution u. Consequently, the error $e = u - u_h$ is usually smaller on element vertices than the error at other points in the element [3].

---

[2] The $\boldsymbol{Q}_2$ estimator is implemented in IFISS [20]. In IFISS, there is some modification for the $\boldsymbol{Q}_2$ correction space on the boundary elements (which contain some edges in $\partial\Omega$). However, for simplicity, the domain boundary effect is not considered for other error estimators in this chapter, since it is quite small.

[3] This argument can only be verified by numerical experiments, since there is no theory in recent literature to support it. Although there are many publications discussing a stronger argument—natural pointwise superconvergence (see [34], [35] and [33]), Lin [33, pp.70–80] states that there is no superconvergence point for the $\boldsymbol{P}_1$ approximation, whilst it is unclear if there is any superconvergence point for the $\boldsymbol{Q}_1$ approximation.

Table 2.1: Errors for the P_1 approximation, test problem 1.

Refinement level	$\|\|\nabla e\|\|_0$	$\frac{\eta_{P_2}}{\|\|\nabla e\|\|_0}$	$\frac{\eta_R}{\|\|\nabla e\|\|_0}$
2	1.3528×10^{-1}	1.1412×10^{0}	3.1927×10^{0}
3	6.8211×10^{-2}	1.0764×10^{0}	3.1769×10^{0}
4	3.4195×10^{-2}	1.0400×10^{0}	3.1740×10^{0}
Convergence Order	$O(h)$		

Table 2.2: Errors for the Q_1 approximation, test problem 1.

Refinement level	$\|\|\nabla e\|\|_0$	$\frac{\eta_{Q_2}}{\|\|\nabla e\|\|_0}$	$\frac{\eta_R}{\|\|\nabla e\|\|_0}$
1	5.3823×10^{-1}	1.0032×10^{0}	4.7380×10^{0}
2	2.7267×10^{-1}	1.0002×10^{0}	4.8157×10^{0}
3	1.3678×10^{-1}	0.9996×10^{0}	4.8818×10^{0}
Convergence Order	$O(h)$		

However, the standard analysis methodology introduced in [47] to establish (2.14)–(2.15) for local problem estimators does not capture this idea. In these analysis techniques, the first step is to establish the upper bound (2.14) and the local lower bound (2.15) for the residual estimator which is defined as

$$\eta_{R,T} = \sqrt{\frac{h_T^2}{p^2}||R_T||_T^2 + \sum_{E\in\partial T} \frac{h_E}{p}\,||R_E||_E^2}, \tag{2.17}$$

$$\eta_R = \sqrt{\sum_{T\in T_h} \eta_{R,T}^2}, \tag{2.18}$$

where p is the order of the approximation polynomial (i.e. $p = 1$ for the P_1 and Q_1 approximations and $p = 2$ for the P_2 and Q_2 approximations). After that, a second step is to show the equivalence between the residual estimator and the local problem estimator.

Table 2.1 and 2.2 show the exact error and the effectivity of the P_2 and Q_2 estimators. It can be seen that the exact error reduces by a factor of two, which is expected for (bi-)linear finite element approximations. The effectivity of the P_2 and Q_2 estimators is close to one, whereas the residual estimator is much less effective.

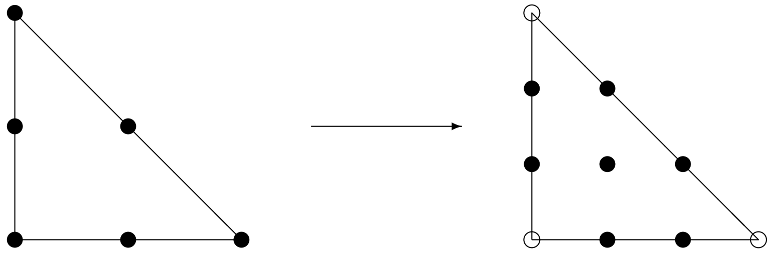

P_2 element P_3 error element

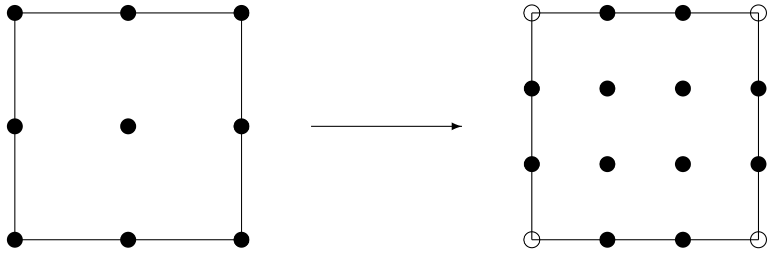

Q_2 element Q_3 error element

Figure 2.4: Error elements for the P_2 and Q_2 approximations, part **1**.

2.3 Error Estimators for (Bi-)quadratic Elements

2.3.1 P_3 and Q_3 estimation strategy

The P_3 and Q_3 error estimators are direct modifications of the lowest order case. Fig. 2.4 shows the P_3 and Q_3 error elements, which are the P_3 and Q_3 elements with the vertex nodes removed. Using the standard analysis techniques in [46], these estimators can be shown to satisfy (2.14)–(2.15). So, the P_3 and Q_3 estimators are mathematically efficient and reliable.

Next, test problem 1 is used to test the performance of the P_3 and Q_3 estimators. From Table 2.3, it can be seen that the effectivity of the P_3 estimator is about 2.7 rather than 1, while the residual estimator for this situation is even worse—its effectivity is more than 5. Table 2.4 shows the effectivity of the Q_3 estimator, which is about 2. In summary, these estimators are not as effective as their lowest order counterparts.

For the mesh shown in Fig. 2.2(b), the element contributions of the exact error, the P_3 estimator and the residual estimator for test problem 1 are provided in Fig. 2.5. It can be seen that since the solution in Fig. 2.5(a) changes rapidly towards the corner $(1, 1)$, the exact

Table 2.3: Errors for the P_2 approximation, test problem 1, part **1**.

Refinement level	$\|\|\nabla e\|\|_0$	$\frac{\eta_{P_3}}{\|\|\nabla e\|\|_0}$	$\frac{\eta_R}{\|\|\nabla e\|\|_0}$
2	2.7942×10^{-3}	2.5790×10^{0}	5.4970×10^{0}
3	7.0576×10^{-4}	2.7128×10^{0}	5.4878×10^{0}
4	1.7736×10^{-4}	2.7792×10^{0}	5.4826×10^{0}
Convergence Order	$O(h^2)$		

Table 2.4: Errors for the Q_2 approximation, test problem 1, part **1**.

Refinement level	$\|\|\nabla e\|\|_0$	$\frac{\eta_{Q_3}}{\|\|\nabla e\|\|_0}$	$\frac{\eta_R}{\|\|\nabla e\|\|_0}$
1	1.1391×10^{-2}	1.9617×10^{0}	3.8793×10^{0}
2	2.8514×10^{-3}	1.9521×10^{0}	3.8747×10^{0}
3	7.1310×10^{-4}	1.9493×10^{0}	3.8734×10^{0}
Convergence Order	$O(h^2)$		

error is maximized near this corner, which is expected for any finite element approximation. The residual estimator in Fig. 2.5(c) has the same shape as the exact error, but the scale is much larger. Fig. 2.5(d) shows that the P_3 estimator provides wrong information about the error. In addition, looking at the mesh in Fig. 2.2(b) again, it can be seen that the P_3 estimator is quite mesh dependent—if the triangles have an edge parallel to $y = x$ (along which the exact solution changes rapidly), the error is small, but otherwise it is large.

From the discussion above, the P_3 estimator provides quite inaccurate estimation for the errors, whereas the Q_3 estimator is not effective enough either. This motivates the next section which is to find effective estimators for the P_2 and Q_2 approximations.

2.3.2 P_4 and Q_4 estimation strategy

We hypothesize that the P_3 and Q_3 estimators are not effective, because their Dirichlet boundary conditions may be inappropriate. For linear interpolation, the most accurate points should be the vertices. However, for quadratic interpolation, the midpoints are also quite accurate. In detail, from Lin [33, pp.70–80], the P_2 and Q_2 nodes are typically the

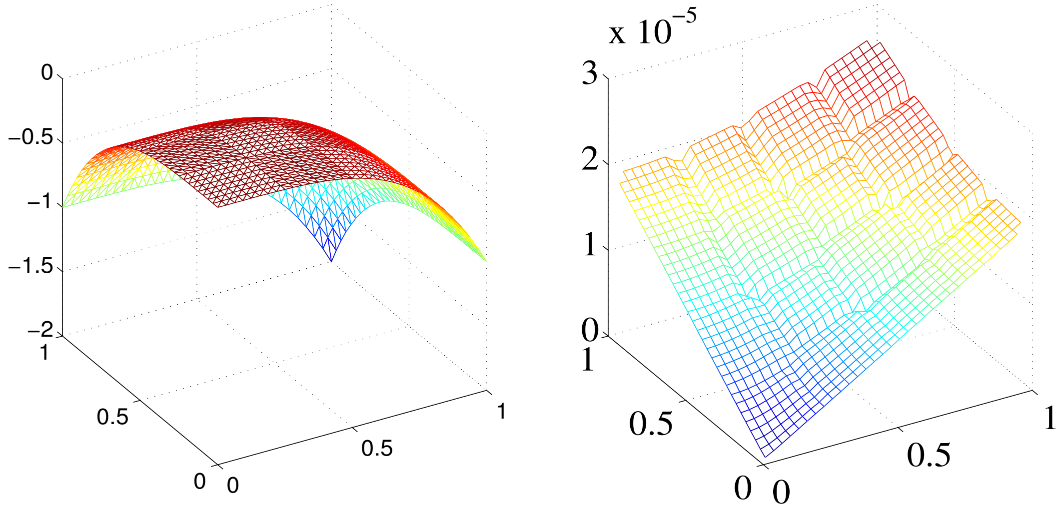

(a) The P_2 solution (b) Exact error $\|\nabla e\|_{0,T}$

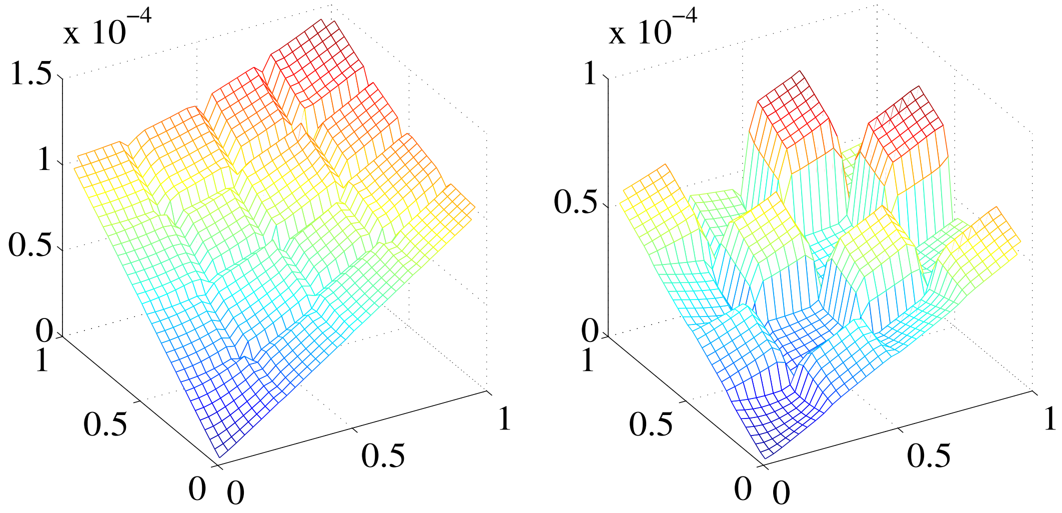

(c) Residual Estimator $\eta_{R,T}$ (d) P_3 estimator $\eta_{P_3,T}$

Figure 2.5: Error estimators for P_2 approximation, test problem 1, part **1**.

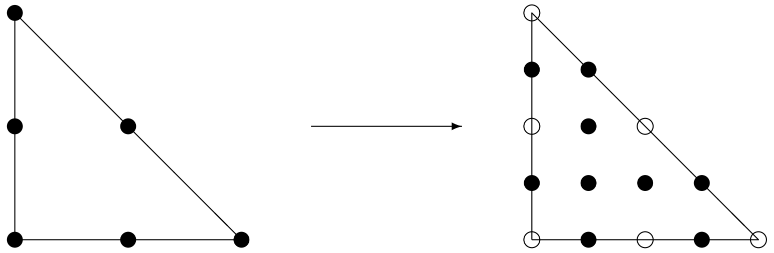

P_2 element P_4 error element

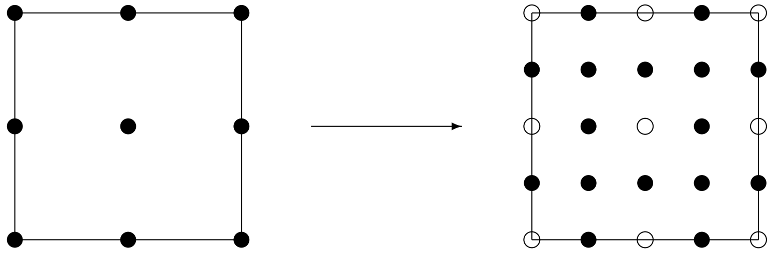

Q_2 element Q_4 error element

Figure 2.6: Error elements for the P_2 and Q_2 approximations, part **2**.

natural superconvergence points for the P_2 and Q_2 approximations. This motivates the P_4 and Q_4 estimators that we developed and are shown in Fig. 2.6.

For test problem 1, the element contribution of the P_4 estimator is shown in Fig. 2.7(d) for the mesh refinement level three. From this figure, it can be seen that the P_4 estimator provides quite an accurate approximation of the exact error.

Tables 2.5 and 2.6 show the effectivity of the P_4 and Q_4 estimators, while the results of the other estimators are also provided for comparison. From Table 2.5, the effectivity of the P_4 estimator is in the interval $(1.25, 1.27)$, which is still close to 1. However, from Table 2.6, the effectivity of the Q_4 estimator is slightly larger, which is around 1.5. So, further modification is needed for the Q_4 estimator, which will be discussed in the next section.

2.3.3 A refined Q_4 estimation strategy

In order to find an effective estimator for the Q_2 approximation, three levels of reduction of the Q_4 element are tested, which are shown in Fig. 2.8. For the biquadratic approximation, the most accurate points might be the midpoints—this motivates the reduction level a, in

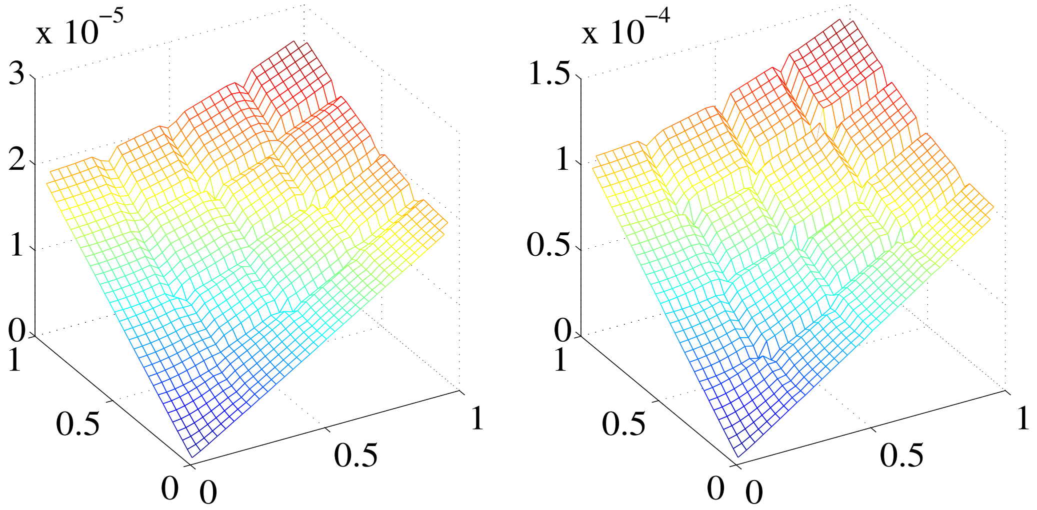

(a) Exact error $||\nabla e||_{0,T}$ (b) Residual Estimator $\eta_{R,T}$

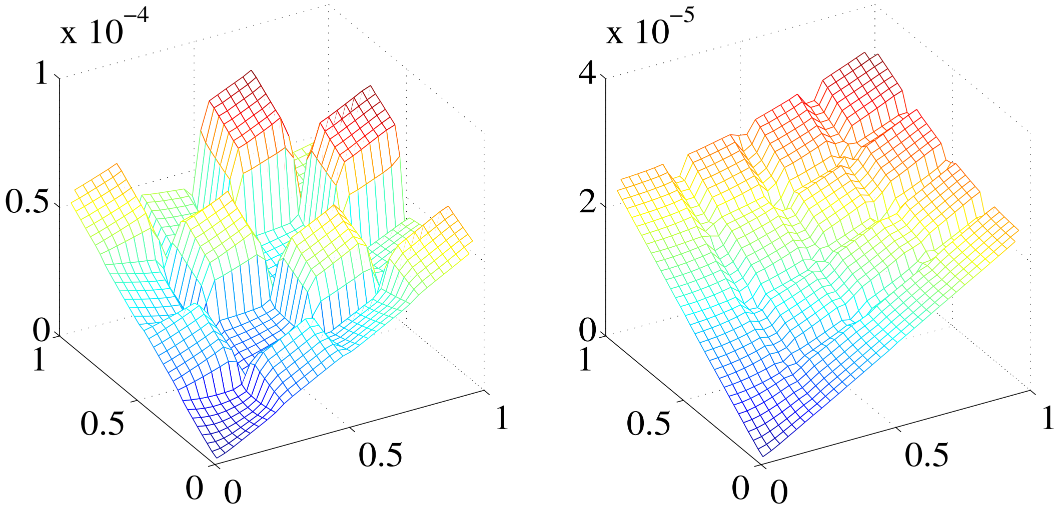

(c) P_3 estimator $\eta_{P_3,T}$ (d) P_4 estimator $\eta_{P_4,T}$

Figure 2.7: Error estimators for $\boldsymbol{P}_2$ approximation, test problem 1, part **2**.

Table 2.5: Errors for the $\boldsymbol{P}_2$ approximation, test problem 1, part **2**.

Refinement level	$\|\|\nabla e\|\|_0$	$\frac{\eta_{P_4}}{\|\|\nabla e\|\|_0}$	$\frac{\eta_{P_3}}{\|\|\nabla e\|\|_0}$	$\frac{\eta_R}{\|\|\nabla e\|\|_0}$
2	2.7942×10^{-3}	1.2538×10^{0}	2.5790×10^{0}	5.4970×10^{0}
3	7.0576×10^{-4}	1.2625×10^{0}	2.7128×10^{0}	5.4878×10^{0}
4	1.7736×10^{-4}	1.2667×10^{0}	2.7128×10^{0}	5.4878×10^{0}
Convergence Order	$O(h^2)$			

Table 2.6: Errors for the Q_2 approximation, test problem 1, part **2**.

Refinement level	$\|\|\nabla e\|\|_0$	$\frac{\eta_{Q_4}}{\|\|\nabla e\|\|_0}$	$\frac{\eta_{Q_3}}{\|\|\nabla e\|\|_0}$	$\frac{\eta_R}{\|\|\nabla e\|\|_0}$
1	1.1391×10^{-2}	1.4518×10^0	1.9617×10^0	3.8793×10^0
2	2.8514×10^{-3}	1.4510×10^0	1.9521×10^0	3.8747×10^0
3	7.1310×10^{-4}	1.4508×10^0	1.9493×10^0	3.8734×10^0
Convergence Order	$O(h^2)$			

Table 2.7: Errors for the Q_2 approximation, test problem 1, part **3**.

Refinement level	$\frac{\eta^a_{Q_4}}{\|\|\nabla e\|\|_0}$	$\frac{\eta^b_{Q_4}}{\|\|\nabla e\|\|_0}$	$\frac{\eta^c_{Q_4}}{\|\|\nabla e\|\|_0}$
1	1.7148×10^0	1.4518×10^0	1.0504×10^0
2	1.7140×10^0	1.4510×10^0	1.0492×10^0
3	1.7137×10^0	1.4508×10^0	1.0488×10^0

which the values of the error on the midpoints are set to zero. Level b is the Q_4 element with all the Q_2 nodes removed, which has been tested in Section 2.3.2. Since the biquadratic approximation is a tensor product of the one dimensional quadratic approximation, Level c removes all the vertices and all the nodes on the horizontal and vertical midlines where at least one component of the tensor product is a midpoint node.

Note that, some removed nodes in Level c are not superconvergence points. This is because our criterion for removing nodes is the pointwise error rather than the natural pointwise superconvergence which is a much stronger criterion. From numerical experiments, the error at the removed non-Q_2 nodes in Level c is still relatively small compared with the error at other points, even though the error at these removed non-Q_2 nodes is not reduced by a larger factor.

The effectivities of these Q_4 estimators are shown in Table 2.7, where $\eta^a_{Q_4}$, $\eta^b_{Q_4}$ and $\eta^c_{Q_4}$ denote the global estimated error for the reduction level a, b and c respectively. From Table 2.7, Level c is very effective—its effectivity is quite close to one. In addition, Level c is relatively cheap, since it has only 12 degrees of freedom per element.

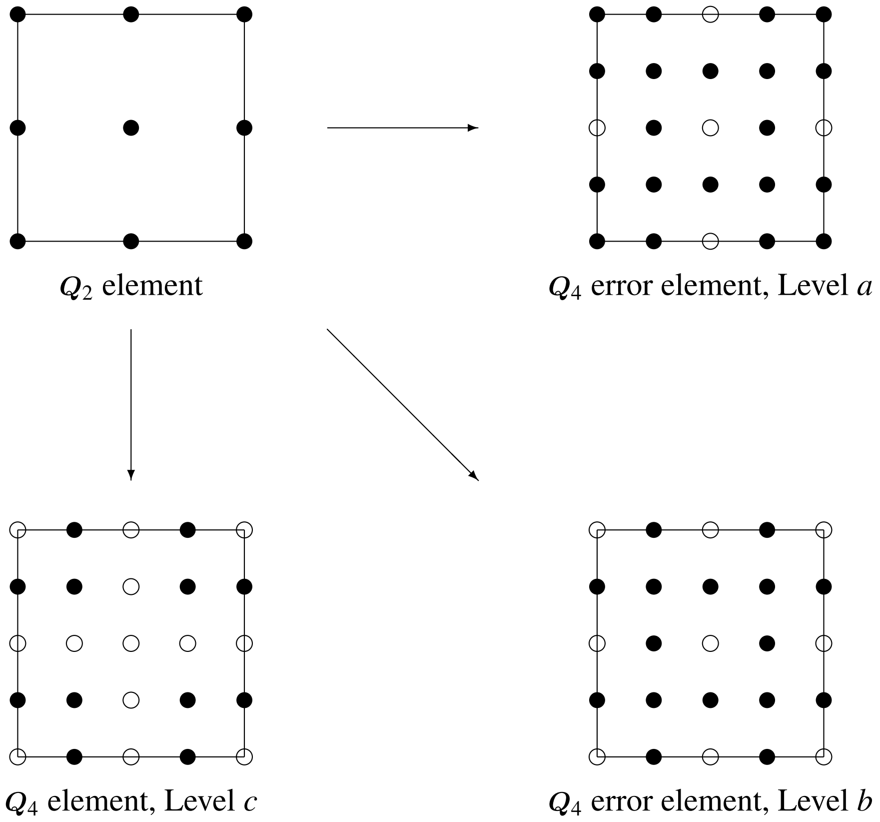

Figure 2.8: Error elements for the Q_2 approximation, part **3**.

2.4 More Challenging Test Problems for (Bi-)quadratic Elements

From the discussion of Section 2.3, it can be concluded that the P_4 estimator and the Q_4 estimator with reduction level c are effective for the P_2 and Q_2 approximations respectively. However, this conclusion is based on test problem 1, which is very smooth—just a fourth order polynomial. So, in order to guarantee the effectivity of these two error estimators, more test problems are necessarily needed. In this section, two additional numerical examples are tested. The first one has a complicated smooth solution and the second one has a singular solution.

2.4.1 Test problem 2: a smooth solution

The solution of test problem 2 is:

$$u = \sin(\pi x)\sin(\pi y)\exp(x). \tag{2.19}$$

The domain and the initial meshes for this test problem are the same as test problem 1. Table 2.8 shows the exact errors and estimated errors for the triangular P_2 approximation. The effectivity of the P_4 estimator is in the interval (1.23, 1.25) which is broadly consistent with test problem 1. Table 2.9 shows the errors for the rectangular Q_2 approximation, and it can be seen that the Q_4 estimator with reduction level c is still very effective.

Some aspects of the quadrature used need to be clarified at this point. For test problem 1, the exact solution and the source function f are polynomials with order at most four. So, a Gaussian quadrature rule with a small number of Gauss points is enough to accurately compute the integrals arising with computing the exact error and the estimated errors. However, for test problems 2 and 3, the exact solutions are more complicated. For the triangular case, a high degree Gaussian quadrature rule with 73 Gauss points provided by Dunavant [19] is used. For the rectangular case, the tensor product of the one dimensional ten-point Gauss rule [4] is used.

---

[4] We also tried the MATLAB function **dblquad**. It does not provide any significantly different result.

Table 2.8: Errors for the $\boldsymbol{P}_2$ approximation, test problem 2.

Refinement level	$\|\|\nabla e\|\|_0$	$\frac{\eta_{P_4}}{\|\|\nabla e\|\|_0}$	$\frac{\eta_R}{\|\|\nabla e\|\|_0}$
2	1.5929×10^{-2}	1.2313×10^{0}	4.2048×10^{0}
3	4.0142×10^{-3}	1.2405×10^{0}	4.1213×10^{0}
4	1.0072×10^{-3}	1.2441×10^{0}	4.0792×10^{0}
Convergence Order	$O(h^2)$		

Table 2.9: Errors for the $\boldsymbol{Q}_2$ approximation, test problem 2.

Refinement level	$\|\|\nabla e\|\|_0$	$\frac{\eta^c_{Q_4}}{\|\|\nabla e\|\|_0}$	$\frac{\eta_R}{\|\|\nabla e\|\|_0}$
1	2.1805×10^{-2}	1.0459×10^{0}	3.9094×10^{0}
2	5.4653×10^{-3}	1.0479×10^{0}	3.8826×10^{0}
3	1.3672×10^{-3}	1.0485×10^{0}	3.8755×10^{0}
Convergence Order	$O(h^2)$		

2.4.2 Test problem 3: a singular solution

Test problem 3 is the example 1.1.4 in [21, p.12], which is also included in IFISS [20]. The solution of this test problem is:

$$u = r^{2/3} \sin((2\theta + \pi)/3), \tag{2.20}$$

where $r = \sqrt{x^2 + y^2}$, and θ is the angle with the $x-$axis. The domain of test problem 3 is the $L-$shape domain which is $(-1, 1) \times (-1, 1) \setminus (-1, 0] \times (-1, 0]$. The initial triangular and rectangular meshes are shown in Fig. 2.9.

Tables 2.10 and 2.11 provide the effectivity of the $\boldsymbol{P}_4$ estimator and the $\boldsymbol{Q}_4$ estimator with reduction level c, which show that their effectivity is still close to one. So, these two estimators are still effective for this singular problem. In addition, from both tables, the exact errors of the $\boldsymbol{P}_2$ and $\boldsymbol{Q}_2$ approximations reduce by a factor of approximately $2^{2/3}$ as the mesh is refined, which is consistent with the results in [21, p.47].

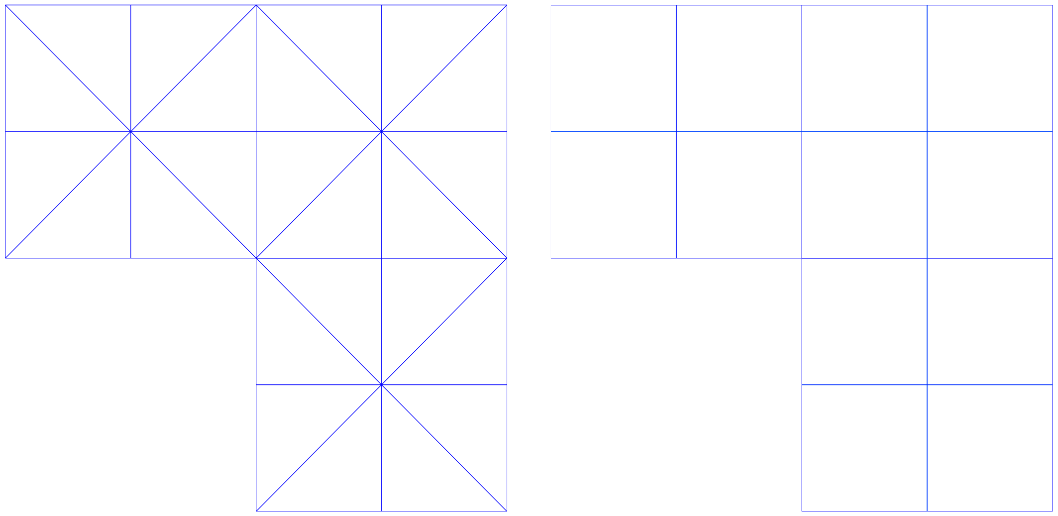

The initial triangular mesh The initial rectangular mesh

Figure 2.9: Initial meshes for test problem 3.

Table 2.10: Errors for the $\boldsymbol{P}_2$ approximation, test problem 3.

Refinement level	$\lVert\nabla e\rVert_0$	$\frac{\eta_{P_4}}{\lVert\nabla e\rVert_0}$	$\frac{\eta_R}{\lVert\nabla e\rVert_0}$
2	5.2758×10^{-2}	8.9145×10^{-1}	2.8267×10^{0}
3	3.3228×10^{-2}	8.9130×10^{-1}	2.8261×10^{0}
4	2.0930×10^{-2}	8.9122×10^{-1}	2.8258×10^{0}
Convergence Order	$O(h^{2/3})$		

Table 2.11: Errors for the $\boldsymbol{Q}_2$ approximation, test problem 3.

Refinement level	$\lVert\nabla e\rVert_0$	$\frac{\eta^c_{Q_4}}{\lVert\nabla e\rVert_0}$	$\frac{\eta_R}{\lVert\nabla e\rVert_0}$
1	6.1493×10^{-2}	8.9795×10^{-1}	3.0061×10^{0}
2	3.8728×10^{-2}	8.9767×10^{-1}	3.0052×10^{0}
3	2.4394×10^{-2}	8.9756×10^{-1}	3.0049×10^{0}
4	1.5366×10^{-2}	8.9751×10^{-1}	3.0047×10^{0}
Convergence Order	$O(h^{2/3})$		

2.5 Summary and Conclusion

In this chapter, the strategy of local problem error estimation for the diffusion problem is reviewed. Results from test problem 1 show that the $\boldsymbol{P}_2$ and $\boldsymbol{Q}_2$ estimators are effective for the linear and bilinear approximations. After that, the $\boldsymbol{P}_3$ and $\boldsymbol{Q}_3$ estimators are shown to be ineffective for the quadratic and biquadratic approximations. Finally, the following estimators are effective

- the $\boldsymbol{P}_4$ estimator for the $\boldsymbol{P}_2$ approximation;
- the $\boldsymbol{Q}_4$ estimator with reduction level c for the $\boldsymbol{Q}_2$ approximation.

Note that, the upper and lower bounds (2.14)–(2.15) for the $\boldsymbol{P}_4$ and $\boldsymbol{Q}_4$ estimators can also be established using the analysis methodology introduced in [46]. However, these upper and lower bounds are necessary but not sufficient for an effective error estimator.

A more interesting problem is addressed in the next chapter—that of establishing effective a posteriori error estimators for inf-sup stable mixed approximations for incompressible flow problems.

Chapter 3

A Posteriori Error Estimation for Classical Mixed Approximation of Stokes Equations

3.1 Introduction

The mathematical analysis foundation of a posteriori error estimation for incompressible flow problems was established in Bank & Welfert [7] and Verfürth [45]. Subsequently, Ainsworth & Oden [3] introduced the methodology of "local Poisson problem" error estimation (which is adopted herein). After that, Kay and Sivester [30] show that the local Poisson problem estimator is effective and computationally cheap for the stabilized $\boldsymbol{Q}_1 - \boldsymbol{P}_0$ approximation, which will be discussed in detail in Section 4.4.

Note that the pioneering a posteriori error estimation techniques for incompressible flow are typically built on the lowest order approximations, e.g. stabilized $\boldsymbol{Q}_1 - \boldsymbol{P}_0$ approximation and stable $\boldsymbol{P}_1 - \boldsymbol{P}_1$ (linear velocity, continuous linear pressure) mixed approximation, using either bubble terms (i.e. the mini-element, see e.g. [12, p. 153]), or a macroelement definition of the pressure (see e.g. [12, p. 152]) to guarantee inf-sup stability. For this reason, the aim of this chapter is to establish simple and effective error estimation techniques for higher order stable mixed approximations: in particular $\boldsymbol{Q}_2 - \boldsymbol{P}_{-1}$ and $\boldsymbol{Q}_2 - \boldsymbol{Q}_1$.

As discussed in Chapter 2, the main issue of establishing effective local problem estimators is to find proper correction spaces. Similarly to the process in Chapter 2, we start with testing the $\boldsymbol{Q}_3$ correction space. Unlike the diffusion problem, our numerical tests show that the $\boldsymbol{Q}_3$ correction space works well for the $\boldsymbol{Q}_2 - \boldsymbol{P}_{-1}$ and $\boldsymbol{Q}_2 - \boldsymbol{Q}_1$ approximations for the Stokes problem (see Section 3.4). So, there is no need to use the higher order $\boldsymbol{Q}_4$ correction space, which is more expensive. A detailed study will be given in the following sections. Although we restrict attention to two dimensional approximation throughout this chapter, the extension of our approach to three dimensional $\boldsymbol{Q}_2$–$\boldsymbol{P}_{-1}$ or $\boldsymbol{P}_{2*}$–$\boldsymbol{P}_{-1}$ approximation (superquadratic velocity, discontinuous linear pressure, see [21, p. 248]) using bricks or tetrahedra is completely straightforward.

This chapter is based on Liao and Silvester [32] and an outline is as follows. In the next section we review the notion of mixed approximation of the Stokes equations. We present a theoretical analysis of three a posteriori error estimation strategies for $\boldsymbol{Q}_2$–$\boldsymbol{P}_{-1}$ mixed approximation in Section 3.3. Specifically, three alternative error estimators are shown to be equivalent to the discretisation error. Some numerical results are presented in Section 3.4. Here the efficiency and reliability of the Poisson problem estimator is compared with the popular Z–Z error indicator originally introduced by Zienkiewicz & Zhu [48]. Some conclusions are given in Section 3.5.

3.2 Mathematical Setting

In this chapter, we consider the simplest possible model of viscous incompressible flow in $\mathbb{R}^2$:

$$-\nabla^2\vec{u} + \nabla p = \vec{0} \quad \text{in} \quad \Omega, \tag{3.1}$$

$$\nabla \cdot \vec{u} = 0 \quad \text{in} \quad \Omega, \tag{3.2}$$

$$\vec{u} = \vec{g} \quad \text{on} \quad \partial\Omega_D, \tag{3.3}$$

$$\frac{\partial \vec{u}}{\partial n} - \vec{n}p = \vec{0} \quad \text{on} \quad \partial\Omega_N. \tag{3.4}$$

Note that the right hand side of (3.1) is set to zero which is different from (1.1) in Chapter 1. For convenience, in the next section, the boundary data $\vec{g}$ will be assumed to be a polynomial with order at most two—this will ensure that there is no error incurred in approximating the boundary condition on $\partial\Omega_D$.

As discussed in Chapter 1, the weak formulation of (3.1)–(3.4) is: find $\vec{u} \in \boldsymbol{H}^1_E$ and $p \in \boldsymbol{P}$ such that

$$\int_\Omega \nabla\vec{u} : \nabla\vec{v} - \int_\Omega p\nabla\cdot\vec{v} = 0 \quad \forall\vec{v} \in \boldsymbol{H}^1_{E_0}, \tag{3.5}$$

$$\int_\Omega q\nabla\cdot\vec{u} = 0 \qquad \forall q \in \boldsymbol{P}. \tag{3.6}$$

A sufficient condition for the existence and uniqueness of a solution satisfying (3.5)–(3.6) is the continuous inf-sup condition (see Definition 1.20). An immediate consequence of the stability bound (1.20) is the "$\mathfrak{B}$-stability bound" given below. For a proof see [21, Lemma 5.2].

Proposition 3.2.1 *$\mathfrak{B}$-stability: working with the "big" bilinear form $\mathfrak{B} : (\boldsymbol{H}^1, \boldsymbol{P}) \times (\boldsymbol{H}^1, \boldsymbol{P}) \to \mathbb{R}$ so that*

$$\mathfrak{B}((\vec{u}, p); (\vec{v}, q)) = (\nabla\vec{u}, \nabla\vec{v}) - (p, \nabla\cdot\vec{v}) - (q, \nabla\cdot\vec{u}), \tag{3.7}$$

for all $(\vec{w}, s) \in \boldsymbol{H}^1_{E_0} \times \boldsymbol{P}$, we have that

$$\sup_{(\vec{v},q)\in\boldsymbol{H}^1_{E_0}\times\boldsymbol{P}} \frac{\mathfrak{B}((\vec{w}, s); (\vec{v}, q))}{|\vec{v}|_1 + \|q\|_0} \geq \gamma_D(|\vec{w}|_1 + \|s\|_0), \tag{3.8}$$

where γ_D depends only on the shape of the domain Ω.

The mixed finite element approximation of (3.5)–(3.6) is: find $\vec{u}_h \in X^h_E$ and $p_h \in M^h$ such that,

$$\int_\Omega \nabla\vec{u}_h : \nabla\vec{v}_h - \int_\Omega p_h\nabla\cdot\vec{v}_h = 0 \quad \forall\vec{v}_h \in X^h_0, \tag{3.9}$$

$$\int_\Omega q_h\nabla\cdot\vec{u}_h = 0 \quad \forall q_h \in M^h, \tag{3.10}$$

where the finite dimensional spaces X^h_E, X^h_0 and M^h are introduced in Section 1.5.

We let $(\vec{u}, p)$ denote the solution of (3.5)–(3.6) and let $(\vec{u}_h, p_h)$ denote the solution of (3.9)–(3.10) with $\boldsymbol{Q}_2$–$\boldsymbol{P}_{-1}$ approximation on a rectangular subdivision T_h, which is assumed to be regular and isotropic in this chapter. Our aim is to estimate the velocity and the pressure errors

$$\vec{e} = \vec{u} - \vec{u}_h, \qquad \epsilon = p - p_h, \tag{3.11}$$

by post-processing the computed solution $(\vec{u}_h, p_h)$. Following established convention, C and c denote generic constants which are independent of the mesh size, the domain Ω, and the solution $(\vec{u}, p)$ throughout this chapter. Such constants could depend on the element aspect ratio ρ_T.

If an error estimator η is to be useful then an important factor is the requirement that it should be cheap to compute—as a rule of thumb, the computational work should scale linearly as the number of elements is increased. As discussed in Chapter 2, an error estimator is efficient and reliable, if it gives the following upper and lower bounds,

$$
\begin{aligned}
|\vec{e}|_1 + \|\epsilon\|_0 &\leq C_\Omega \eta, & (3.12)\\
\eta_T &\leq C_\Omega \left(\sum_{T' \in \omega_T} \left\{ |\vec{e}|^2_{1,T'} + \|\epsilon\|^2_{0,T'} \right\} \right)^{1/2}, & (3.13)
\end{aligned}
$$

where $\eta = \sqrt{\sum_{T \in T_h} \eta_T^2}$, and the generic constant C_Ω is independent of the mesh size and the exact solution but may depend on the domain and the element aspect ratio. The upper bound (3.12) is to guarantee the accuracy of mixed approximations, whereas the local lower bound (3.13) is used to drive a reliable adaptive refinement process. In addition, an estimator is said to be effective if $\eta/(|\vec{e}|_1 + \|\epsilon\|_0)$ is close to one.

In the next sections we will introduce three alternative estimators and show that each satisfies the requirements (3.12) and (3.13).

3.3 Analysis of Estimators

We begin this section by summarising some standard results that will prove to be useful. First, so-called bubble functions on the reference element $\tilde{T} = (0,1) \times (0,1)$ are defined as follows:

$$
\begin{aligned}
b_{\tilde{T}} &= 2^4 x(1-x)y(1-y),\\
b_{\tilde{E}_1,\tilde{T}} &= 2^2 x(1-x)(1-y),\\
b_{\tilde{E}_2,\tilde{T}} &= 2^2 y(1-y)x,\\
b_{\tilde{E}_3,\tilde{T}} &= 2^2 x(1-x)y,\\
b_{\tilde{E}_4,\tilde{T}} &= 2^2 y(1-y)(1-x).
\end{aligned}
$$

Here $b_{\tilde{T}}$ is the reference *element* bubble function, and $b_{\tilde{E}_i,\tilde{T}}$, $i = 1 : 4$ are reference *edge* bubble functions. For any $T \in T_h$, the *element* bubble function is $b_T = b_{\tilde{T}} \circ F_T$ and the element *edge* bubble function is $b_{E_i,T} = b_{\tilde{E}_i,\tilde{T}} \circ F_T$, where F_T is the affine map from $\tilde{T}$ to T. For an interior edge $E \in \boldsymbol{\mathcal{E}}_{h,\Omega}$ and $E = \overline{T_1} \cap \overline{T_2}$, b_E is defined as follows,

$$b_E = \begin{cases} b_{E,T_1} & \text{in } \overline{T_1}, \\ b_{E,T_2} & \text{in } \overline{T_2}, \\ 0 & \text{in } \Omega \setminus (\overline{T_1} \cup \overline{T_2}). \end{cases}$$

For a boundary edge $E \in \boldsymbol{\mathcal{E}}_{h,D} \cup \boldsymbol{\mathcal{E}}_{h,N}$, $b_E = b_{E,T}$, where T is the rectangle such that $E \in \boldsymbol{\mathcal{E}}(T)$. With these bubble functions, Creusé et al. [17, Lemma 4.1] established the following lemma.

Lemma 3.3.1 *Inverse inequalities: let T be an arbitrary rectangle in T_h and $E \in \boldsymbol{\mathcal{E}}(T)$. For any $\vec{v}_T \in \boldsymbol{P}_{k_0}(T)$ and $\vec{v}_E \in \boldsymbol{P}_{k_1}(E)$, the following inequalities hold,*

$$c_k \|\vec{v}_T\|_{0,T} \le \|\vec{v}_T b_T^{1/2}\|_{0,T} \le C_k \|\vec{v}_T\|_{0,T}, \tag{3.14}$$

$$|\vec{v}_T b_T|_{1,T} \le C_k h_T^{-1} \|\vec{v}_T\|_{0,T}, \tag{3.15}$$

$$c_k \|\vec{v}_E\|_{0,E} \le \|\vec{v}_E b_E^{1/2}\|_{0,E} \le C_k \|\vec{v}_E\|_{0,E}, \tag{3.16}$$

$$\|\vec{v}_E b_E\|_{0,T} \le C_k h_E^{1/2} \|\vec{v}_E\|_{0,E}, \tag{3.17}$$

$$|\vec{v}_E b_E|_{1,T} \le C_k h_E^{-1/2} \|\vec{v}_E\|_{0,E}, \tag{3.18}$$

where, c_k and C_k are two constants which only depend on the element aspect ratio and the polynomial degrees k_0 and k_1.

Here, k_0 and k_1 are fixed and c_k and C_k can be associated with generic constants c and C. In addition, $\vec{v}_E$ which is only defined on the edge E also denotes its natural extension to the element T.

Second, we recall some quasi-interpolation estimates in the following lemma.

Lemma 3.3.2 *Clément interpolation estimate: Given $\vec{v} \in \boldsymbol{H}^1$, let $\vec{v}_h \in X^h \subset \boldsymbol{H}^1$ be the quasi-interpolant of $\vec{v}$ defined by averaging as in [16]. For any $T \in T_h$,*

$$\|\vec{v} - \vec{v}_h\|_{0,T} \le C h_T |\vec{v}|_{1,\tilde{\omega}_T}, \tag{3.19}$$

and for all $E \in \mathcal{E}(T)$

$$\|\vec{v} - \vec{v}_h\|_{0,E} \leq C h_E^{1/2} |\vec{v}|_{1,\tilde{\omega}_E}. \tag{3.20}$$

We are now ready to introduce our three alternative error estimators.

3.3.1 A residual error estimator

The material in this section is well known and can be found in several places, e.g. in Creusé et al. [17], or [21, section 5.4.2]. The element contribution $\eta_{R,T}$ of the residual error estimator η_R is given by

$$\eta_{R,T}^2 := h_T^2 \, \|\vec{R}_T\|_{0,T}^2 + \|R_T\|_{0,T}^2 + \sum_{E \in \mathcal{E}(T)} h_E \, \|\vec{R}_E\|_{0,E}^2, \tag{3.21}$$

and the components in (3.21) are given by

$$\begin{aligned} \vec{R}_T &:= \{\nabla^2 \vec{u}_h - \nabla p_h\}|_T, & (3.22)\\ R_T &:= \{\nabla \cdot \vec{u}_h\}|_T, & (3.23)\\ \vec{R}_E &:= \begin{cases} \frac{1}{2}[\![\nabla \vec{u}_h - p_h \mathbf{I}]\!]_E & E \in \mathcal{E}_{h,\Omega} \\ \frac{\partial \vec{u}_h}{\partial \vec{n}_{E,T}} - p_h \vec{n}_{E,T} & E \in \mathcal{E}_{h,N} \\ 0 & E \in \mathcal{E}_{h,D} \end{cases}, & (3.24) \end{aligned}$$

with the key contribution coming from the *stress jump* associated with an edge E adjoining elements T and S:

$$[\![\nabla \vec{u}_h - p_h \vec{\mathbf{I}}]\!] := ((\nabla \vec{u}_h - p_h \vec{\mathbf{I}})|_T - (\nabla \vec{u}_h - p_h \vec{\mathbf{I}})|_S) \vec{n}_{E,T}.$$

The *global* residual error estimator is given by $\eta_R := \sqrt{\sum_{T \in T_h} \eta_{R,T}^2}$.

Theorem 3.3.3 *For any mixed finite element approximation (not necessarily inf-sup stable) defined on rectangular grids T_h, the residual estimator η_R satisfies:*

$$\begin{aligned} |\vec{e}|_1 + \|\epsilon\|_0 &\leq C_\Omega \, \eta_R, \\ \eta_{R,T} &\leq C \left(\sum_{T' \in \omega_T} \left\{ |\vec{e}|_{1,T'}^2 + \|\epsilon\|_{0,T'}^2 \right\} \right)^{1/2}. \end{aligned}$$

Note that the constant C in the local lower bound is independent of the domain.

Proof. We include this for completeness. To establish the upper bound we let $[\vec{v}, q] \in \boldsymbol{H}^1_{E_0} \times \boldsymbol{P}$ and $\vec{v}_h \in X^h_0$ be the Clément interpolant of $\vec{v}$, then

$$\begin{aligned}
\mathfrak{B}([\vec{e}, \epsilon]; [\vec{v}, q]) &= \mathfrak{B}([\vec{e}, \epsilon]; [\vec{v} - \vec{v}_h, q]) \\
&= -(\nabla \vec{u}_h, \nabla(\vec{v} - \vec{v}_h)) + (p_h, \nabla \cdot (\vec{v} - \vec{v}_h)) + (q, \nabla \cdot \vec{u}_h) \\
&= \sum_{T \in T_h} \left\{ (\nabla^2 \vec{u}_h - \nabla p_h, \vec{v} - \vec{v}_h)_T - \sum_{E \in \mathcal{E}(T)} \left\langle \vec{R}_E, \vec{v} - \vec{v}_h \right\rangle_E + (q, \nabla \cdot \vec{u}_h)_T \right\},
\end{aligned}$$

where, $\left\langle \vec{R}_E, \vec{v} - \vec{v}_h \right\rangle_E = \int_E \vec{R}_E \cdot (\vec{v} - \vec{v}_h)$. Thus,

$$\begin{aligned}
|\mathfrak{B}([\vec{e}, \epsilon]; [\vec{v}, q])| &\leq \sum_{T \in T_h} \left\{ ||\nabla^2 \vec{u}_h - \nabla p_h||_{0,T} ||\vec{v} - \vec{v}_h||_{0,T} + \sum_{E \in \mathcal{E}(T)} ||\vec{R}_E||_{0,E} ||\vec{v} - \vec{v}_h||_{0,E} \right. \\
&\qquad \left. + ||q||_{0,T} ||\nabla \cdot \vec{u}_h||_{0,T} \right\} \\
&\leq C \left\{ \left(\sum_{T \in T_h} h_T^2 ||\nabla^2 \vec{u}_h - \nabla p_h||^2_{0,T} \right)^{1/2} \left(\sum_{T \in T_h} \frac{1}{h_T^2} ||\vec{v} - \vec{v}_h||^2_{0,T} \right)^{1/2} \right. \\
&\qquad + \left(\sum_{T \in T_h} \sum_{E \in \mathcal{E}(T)} h_E ||\vec{R}_E||^2_{0,T} \right)^{1/2} \left(\sum_{T \in T_h} \sum_{E \in \mathcal{E}(T)} \frac{1}{h_E} ||\vec{v} - \vec{v}_h||^2_{0,E} \right)^{1/2} \\
&\qquad \left. + \left(\sum_{T \in T_h} ||q||^2_{0,T} \right)^{1/2} \left(\sum_{T \in T_h} ||\nabla \cdot \vec{u}_h||^2_{0,T} \right)^{1/2} \right\}.
\end{aligned}$$

Using Lemma 3.3.2 then gives

$$\begin{aligned}
|\mathfrak{B}([\vec{e}, \epsilon]; [\vec{v}, q])| &\leq C \left(\sum_{T \in T_h} \left\{ |\vec{v}|^2_{1,T} + ||q||_{0,T} \right\} \right)^{1/2} \\
&\qquad \times \left(\sum_{T \in T_h} \left\{ h_T^2 ||\vec{R}_T||_{0,T} + \sum_{E \in \mathcal{E}(T)} h_E ||\vec{R}_E||^2_{0,E} + ||R_T||^2_{0,T} \right\} \right)^{1/2}.
\end{aligned}$$

Finally, noting that $\vec{e} = \vec{u} - \vec{u}_h \in \boldsymbol{H}^1_{E_0}$ and using (3.8) gives

$$|\vec{e}|_{1,\Omega} + ||\epsilon||_{0,\Omega} \leq C_\Omega \left(\sum_{T \in T_h} \left\{ h_T^2 ||\vec{R}_T||_{0,T} + \sum_{E \in \mathcal{E}(T)} h_E ||\vec{R}_E||^2_{0,E} + ||R_T||^2_{0,T} \right\} \right)^{1/2}$$

This establishes the upper bound.

Turn to the local lower bound. First, for the element interior residual part, we set $\vec{w}_T := \vec{R}_T b_T$. Since $\vec{w}_T = 0$ on ∂T, it can be extended to the whole of Ω by setting $\vec{w}_T = 0$ in $\Omega \setminus T$ to give an extended function that is in $\boldsymbol{H}^1_{E_0}$. Then,

$$(\nabla \vec{u} - p\mathrm{I}, \nabla \vec{w}_T)_T = (\nabla \vec{u} - p\mathrm{I}, \nabla \vec{w}_T)_\Omega = 0. \tag{3.25}$$

With (3.25),

$$
\begin{aligned}
(\vec{R}_T, \vec{w}_T)_T &= (\nabla^2 \vec{u}_h - \nabla p_h, \vec{w}_T)_T \\
&= -(\nabla \vec{u}_h - p_h \mathrm{I}, \nabla \vec{w}_T)_T + \langle (\nabla \vec{u}_h - p_h \mathrm{I}) \cdot \vec{n}, \vec{w}_T \rangle_{\partial T} \qquad (3.26) \\
&= -(\nabla \vec{u}_h - p_h \mathrm{I}, \nabla \vec{w}_T)_T \\
&= -(\nabla \vec{u}_h - p_h \mathrm{I}, \nabla \vec{w}_T)_T + (\nabla \vec{u} - p\mathrm{I}, \nabla \vec{w}_T)_T \\
&= (\nabla \vec{e} - \epsilon \mathrm{I}, \nabla \vec{w}_T)_T \\
&\leq (|\vec{e}|_{1,T} + ||\epsilon||_{0,T}) |\vec{w}_T|_{1,T} \\
&\leq (|\vec{e}|_{1,T}^2 + ||\epsilon||_{0,T}^2)^{1/2} h_T^{-1} ||\vec{R}_T||_{0,T},
\end{aligned}
$$

where in (3.26), $\langle (\nabla \vec{u}_h - p_h \mathrm{I}) \vec{n}, \vec{w}_E \rangle_{\partial T} = \int_{\partial T} (\nabla \vec{u}_h - p_h \mathrm{I}) \vec{n} \cdot \vec{w}_E$. In addition, from the inverse inequality (3.14), $(\vec{R}_T, \vec{w}_T)_T = ||\vec{R}_T b_T^{1/2}||_{0,T}^2 \geq c ||\vec{R}_T||_{0,T}^2$, thus

$$
h_T^2 ||\vec{R}_T||_{0,T}^2 \leq C \left(|\vec{e}|_{1,T}^2 + ||\epsilon||_{0,T}^2 \right). \tag{3.27}
$$

Next comes the divergence part,

$$
||R_T||_{0,T} = ||\nabla \cdot \vec{u}_h||_{0,T} = ||\nabla \cdot (\vec{u} - \vec{u}_h)||_{0,T} \leq \sqrt{2}\, |\vec{u} - \vec{u}_h|_{1,T} = \sqrt{2}\, |\vec{e}|_{1,T}. \tag{3.28}
$$

Finally, we need to estimate the jump term. For an interior edge $E = \overline{T_1} \cap \overline{T_2}$, we set $\vec{w}_E = \vec{R}_E b_E$ so that

$$
\begin{aligned}
2 \left\langle \vec{R}_E, \vec{w}_E \right\rangle_E &= \sum_{i=1:2} \langle (\nabla \vec{u}_h - p_h \mathrm{I}) \vec{n}, \vec{w}_E \rangle_{\partial T_i} \\
&= (\nabla \vec{u}_h - p_h \mathrm{I}, \nabla \vec{w}_E)_{\omega_E} + \sum_{i=1:2} (\nabla^2 \vec{u}_h - \nabla p_h, \vec{w}_E)_{T_i}.
\end{aligned}
$$

Using the same argument as for (3.25), the following equality holds,

$$
(\nabla \vec{u} - p\mathrm{I}, \nabla \vec{w}_E)_{\omega_E} = 0, \tag{3.29}
$$

and then, using inverse inequalities gives

$$
\begin{aligned}
2 \left\langle \vec{R}_E, \vec{w}_E \right\rangle_E &= -(\nabla \vec{e} - \epsilon \mathrm{I}, \nabla \vec{w}_E)_{\omega_E} + \sum_{i=1:2} (\nabla^2 \vec{u}_h - \nabla p_h, \vec{w}_E)_{T_i} \\
&\leq (|\vec{e}|_{1,\omega_E} + ||\epsilon||_{0,\omega_E}) |\vec{w}_E|_{1,\omega_E} + \sum_{i=1:2} ||\vec{R}_{T_i}||_{0,T_i} ||\vec{w}_E||_{0,\omega_E} \\
&\leq C \left((|\vec{e}|_{1,\omega_E} + ||\epsilon||_{0,\omega_E}) h_E^{-1/2} ||\vec{R}_E||_{0,E} + \sum_{i=1:2} ||\vec{R}_{T_i}||_{0,T_i} h_E^{1/2} ||\vec{R}_E||_E \right) \\
&\leq C \left(\left(|\vec{e}|_{1,\omega_E}^2 + ||\epsilon||_{0,\omega_E}^2 \right)^{1/2} h_E^{-1/2} ||\vec{R}_E||_{0,E} + \sum_{i=1:2} ||\vec{R}_{T_i}||_{0,T_i} h_E^{1/2} ||\vec{R}_E||_E \right).
\end{aligned}
$$

Using (3.27) gives

$$2\left\langle \vec{R}_E, \vec{w}_E \right\rangle_E \leq C\left(|\vec{e}|^2_{1,\omega_E} + \|\epsilon\|^2_{0,\omega_E}\right)^{1/2} h_E^{-1/2}\|\vec{R}_E\|_{0,E}. \tag{3.30}$$

Using (3.16) gives $\langle \vec{R}_E, \vec{w}_E\rangle_E = \|\vec{R}_E b_E^{1/2}\|^2_{0,E} \geq c\|\vec{R}_E\|^2_{0,E}$, and thus using (3.30) gives

$$h_E\|\vec{R}_E\|^2_{0,E} \leq C\left(|\vec{e}|^2_{1,\omega_E} + \|\epsilon\|^2_{0,\omega_E}\right). \tag{3.31}$$

We also need to show that (3.31) holds for boundary edges. First, for the Dirichlet boundary edges, the flux jump is set to be zero, thus (3.31) trivially holds. Second, for an edge $En \in \mathcal{E}(T) \cap \mathcal{E}_{h,N}$, we again set $\vec{w} = \vec{R}_{En} b_{En}$,

$$\begin{aligned}\left\langle \vec{R}_{En}, \vec{w}_{En} \right\rangle_{En} &= \langle (\nabla\vec{u}_h - p_h\mathrm{I})\vec{n}, \vec{w}_{En}\rangle_{\partial T} \\ &= (\nabla\vec{u}_h - p_h\mathrm{I}, \nabla\vec{w}_{En})_T + (\nabla^2\vec{u}_h - \nabla p_h, \vec{w}_{En})_T.\end{aligned}$$

Thus, as for (3.29), we have that

$$(\nabla\vec{u} - p\mathrm{I}, \nabla\vec{w}_{En})_T = 0.$$

Then, using the inverse inequalities and following the argument above gives

$$h_{En}\|\vec{R}_{En}\|^2_{0,En} \leq C\left(|\vec{e}|^2_{1,T} + \|\epsilon\|^2_{0,T}\right). \tag{3.32}$$

Finally, combining (3.27), (3.28), (3.31) and (3.32) establishes the local lower bound. □

Remark 3.3.4 Theorem 3.3.3 also holds for stable (and unstable) mixed approximations defined on a triangular subdivision. The proof is essentially identical to the rectangular case. Specifically, the upper bound can be established directly using the Clément interpolation for triangular meshes. In order to show the local lower bound, we just need to repeat the process for rectangular meshes using a cubic *element* bubble function defined by taking the value one at the centroid of the triangle and zero on the three edges, together with an *edge* bubble function defined by a quadratic polynomial which takes value one at the midpoint of one edge and is zero on the other two edges.

3.3.2 A local Stokes problem error estimator

Here our focus is on the Q_2–P_{-1} approximation method. Specifically, a suitable correction space $\mathbf{Q}_T$ needs to be introduced at this point. For an interior rectangle (i.e. if all four edges are in $\mathcal{E}_{h,\Omega} \cup \mathcal{E}_{h,N}$), $\mathbf{Q}_T$ is the $(Q_3(T))^2$ space excluding the basis functions associated with the four vertices, and for an element with some edges in $\mathcal{E}_{h,D}$, $\mathbf{Q}_T$ is the $(Q_3(T))^2$ space excluding the basis functions associated with the four vertices and all the other nodes on the boundary $\partial\Omega_D$. For a rectangle containing edges in $\mathcal{E}_{h,D}$, it is assumed that at most two neighboring edges are in $\mathcal{E}_{h,D}$. If the rectangle T has only one edge in $\mathcal{E}_{h,D}$, we call it an *edge* element, whereas if it has two neighboring edges in $\mathcal{E}_{h,D}$, we call it a *corner* element. Fig. 3.1 illustrates the types of correction spaces that can arise.

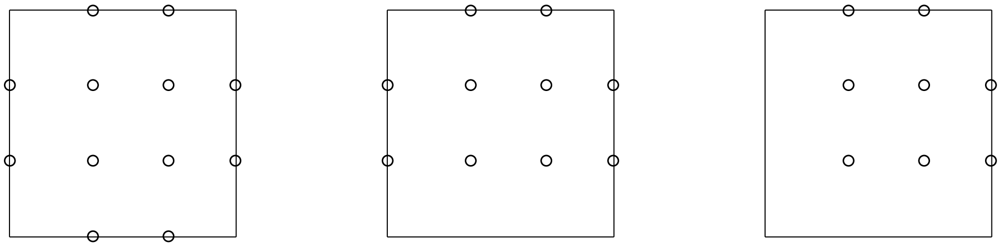

Figure 3.1: The correction space $\mathbf{Q}_T$ for an interior element (left), for an edge element (middle) and for a corner element (right).

The local Stokes problem estimator $\eta_S = \sqrt{\sum_{T \in T_h} \eta_{S,T}^2}$ is then defined as follows,

$$\eta_{S,T}^2 = |\vec{e}_{S,T}|_{1,T}^2 + \|\epsilon_{S,T}\|_{0,T}^2, \tag{3.33}$$

where $(\vec{e}_{S,T}, \epsilon_{S,T}) \in \mathbf{Q}_T \times Q_2(T)$ satisfies

$$(\nabla \vec{e}_{S,T}, \nabla \vec{v})_T - (\epsilon_{S,T}, \nabla \cdot \vec{v})_T = (\vec{R}_T, \vec{v})_T - \sum_{E \in \mathcal{E}(T)} \left\langle \vec{R}_E, \vec{v} \right\rangle_E \quad \forall \vec{v} \in \mathbf{Q}_T, \tag{3.34}$$

$$(\nabla \cdot \vec{e}_{S,T}, q) = (R_T, q)_T \quad \forall q \in Q_2(T). \tag{3.35}$$

Note that, (3.34)–(3.35) represents a Stokes problem posed on an element T with a Neumann (zero flux) boundary condition. Although the velocity solution for a Stokes problem is not uniquely defined when a zero flux condition applies everywhere on the boundary, the special choice of correction space $\mathbf{Q}_T$ guarantees that the system (3.34)–(3.35) always has a unique solution.

We want to establish that the Stokes estimator $\eta_{S,T}$ is equivalent to the residual estimator $\eta_{R,T}$. The following local inf-sup stability estimate will be crucial in achieving this goal.

Lemma 3.3.5 *Local inf-sup stability: for any rectangle $T \in T_h$, there exists a positive constant γ_L independent of h, such that*

$$\min_{0 \neq q_T \in Q_2(T)} \max_{\vec{0} \neq \vec{v}_T \in \mathbf{Q}_T} \frac{|(q_T, \nabla \cdot \vec{v}_T)|}{|\vec{v}_T|_1 \, \|q_T\|_0} \geq \gamma_L. \tag{3.36}$$

Proof. Our proof is a generalization of the approach of Verfürth [45, Lem 4.1]. First, for the reference element $\tilde{T}$, the local inf-sup stability associated with the three types of $\mathbf{Q}_T$ can be established by direct computation of the minimum eigenvalue in (1.41). Next, for an arbitrary element T, we let F_T denote the affine map from $\tilde{T}$ to T and denote the Jacobian determinant of F_T by $|J| = h_{T,x} h_{T,y}$, where $h_{T,x}$ and $h_{T,y}$ are the element sizes in x and y directions respectively. Thus, for any $q \in Q_2(T)$, we define $q_\star := |J|^{1/2} q_T \circ F_T \in Q_2(\tilde{T})$. Then, there exists a $\vec{u}_\star = (u_\star, v_\star)^T \in \mathbf{Q}_{\tilde{T}}$ with $|\vec{u}_\star|_{1,\tilde{T}} = \|q_\star\|_{0,\tilde{T}}$, such that

$$(\nabla \cdot \vec{u}_\star, q_\star)_{\tilde{T}} \geq \tilde{\gamma} \|q_\star\|^2_{0,\tilde{T}} \tag{3.37}$$

where $\tilde{\gamma}$ is the local inf-sup constant for the reference element $\tilde{T}$. If we further define

$$\vec{u}_T := \begin{pmatrix} |J|^{1/2} \frac{1}{h_{T,y}} u_\star \circ F_T^{-1} \\ |J|^{1/2} \frac{1}{h_{T,x}} v_\star \circ F_T^{-1} \end{pmatrix}, \tag{3.38}$$

then denoting $\vec{u}_T = (u_T, v_T)$ and using (s,t) to denote the local coordinates for the reference element, we get

$$\begin{aligned} |\vec{u}_T|^2_{1,T} &= \int_T \Big(\frac{\partial u_T}{\partial x}\Big)^2 + \Big(\frac{\partial v_T}{\partial y}\Big)^2 \\ &= \int_{\tilde{T}} \bigg(\Big(|J|^{1/2} \frac{1}{h_{T,y}} \frac{\partial u_\star}{\partial s} \frac{1}{h_{T,x}}\Big)^2 + \Big(|J|^{1/2} \frac{1}{h_{T,x}} \frac{\partial v_\star}{\partial t} \frac{1}{h_{T,y}}\Big)^2\bigg) |J| \\ &= |\vec{u}_\star|^2_{1,\tilde{T}} = \|q_\star\|^2_{0,\tilde{T}} = \int_{\tilde{T}} q_\star^2 = \int_T (|J|^{1/2} q_T)^2 |J|^{-1} = \|q_T\|^2_{0,T}. \end{aligned}$$

So we see that

$$|\vec{u}_T|_{1,T} = \|q_T\|_{0,T}. \tag{3.39}$$

Next,

$$
\begin{aligned}
(\nabla\cdot\vec{u}_T, q_T)_T &= \int_T \frac{\partial u_T}{\partial x} q_T + \frac{\partial v_T}{\partial y} q_T \\
&= \int_{\tilde{T}} \left(|J|^{1/2}\frac{1}{h_{T,y}}\frac{\partial u_\star}{\partial s}\frac{1}{h_{T,x}}|J|^{-1/2} q_\star + |J|^{1/2}\frac{1}{h_{T,x}}\frac{\partial v_\star}{\partial t}\frac{1}{h_{T,y}}|J|^{-1/2} q_\star \right)|J| \\
&= \int_{\tilde{T}} \left(\frac{\partial u_\star}{\partial s} q_\star + \frac{\partial v_\star}{\partial t} q_\star \right) = (\nabla\cdot\vec{u}_\star, q_\star)_{\tilde{T}} \\
&\geq \tilde{\gamma}\,\|q_\star\|^2_{0,\tilde{T}} = \tilde{\gamma}\,\|q_T\|^2_{0,T}.
\end{aligned}
\tag{3.40}
$$

This establishes the stability bound (3.36) with an inf-sup constant $\gamma_L = \tilde{\gamma}$. □

Mirroring the discussion of the stability of the continuous problem in Section 3.2 leads us to the following result.

Lemma 3.3.6 *Local $\mathfrak{B}$-stability: if the mixed approximation is locally inf-sup stable, then for all $(\vec{w}, s) \in \mathbf{Q}_T \times Q_2(T)$, we have that*

$$
\max_{(\vec{v},q)\in\mathbf{Q}_T\times Q_2(T)} \frac{\mathfrak{B}((\vec{w}, s); (\vec{v}, q))}{|\vec{v}|_{1,T} + \|q\|_{0,T}} \geq \gamma_B(|\vec{w}|_{1,T} + \|s\|_{0,T}),
\tag{3.41}
$$

where, γ_B is a positive constant that only depends on the inf-sup constant γ_L in (3.36).

Proof. See Elman et al. [21, Lemma 5.2]. □

The robustness of the Stokes error estimator is established next.

Theorem 3.3.7 *For $\boldsymbol{Q}_2$–$\boldsymbol{P}_{-1}$ approximation on a rectangle $T \in T_h$, the estimator $\eta_{S,T}$ is equivalent to the residual estimator: $c\,\eta_{S,T} \leq \eta_{R,T} \leq C\eta_{S,T}$.*

Proof. The proof is a generalization of [30, Theorem 3.5]. The details are sketched out below. First, we need to use (3.41):

$$
\begin{aligned}
\eta_{S,T} &= \sqrt{|\vec{e}_{S,T}|^2_{1,T} + \|\epsilon_{S,T}\|^2_{0,T}} \\
&\leq |\vec{e}_{S,T}|_{1,T} + \|\epsilon_{S,T}\|_{0,T} \\
&\leq \frac{1}{\gamma_B} \max_{(\vec{v},q)\in\mathbf{Q}_T\times Q_2(T)} \frac{\mathfrak{B}((\vec{e}_{S,T}, \epsilon_{S,T}); (\vec{v}, q))}{|\vec{v}|_{1,T} + \|q\|_{0,T}} \\
&= \frac{1}{\gamma_B} \max_{(\vec{v},q)\in\mathbf{Q}_T\times Q_2(T)} \frac{(\vec{R}_T, \vec{v})_T - \sum_{E\in\mathcal{E}(T)} \left\langle \vec{R}_E, \vec{v} \right\rangle_E - (q, \nabla\cdot\vec{u}_h)_T}{|\vec{v}|_{1,T} + \|q\|_{0,T}} \\
&\leq \frac{1}{\gamma_B} \max_{(\vec{v},q)\in\mathbf{Q}_T\times Q_2(T)} \frac{\|\vec{R}_T\|_{0,T}\|\vec{v}\|_{0,T} + \sum_{E\in\mathcal{E}(T)} \|\vec{R}_E\|_{0,E}\|\vec{v}\|_{0,E} + \|q\|_{0,T}\|\nabla\cdot\vec{u}_h\|_{0,T}}{|\vec{v}|_{1,T} + \|q\|_{0,T}}.
\end{aligned}
\tag{3.42}
$$

Now, since $\vec{v}$ is zero at the four vertices of T, a scaling argument and the usual trace theorem, see e.g. [21, Lemma 1.5], shows that $\vec{v}$ satisfies

$$||\vec{v}||_{0,E} \leq Ch_E^{1/2}|\vec{v}|_{1,T}, \tag{3.43}$$

$$||\vec{v}||_{0,T} \leq Ch_T|\vec{v}|_{1,T}. \tag{3.44}$$

Combining these two inequalities with (3.42) immediately gives the lower bound in the equivalence relation. For the upper bound, we first let $\vec{w}_T = \vec{R}_T b_T$ (b_T is an element interior bubble function). From (3.34),

$$\begin{aligned}
(\vec{R}_T, \vec{w}_T)_T &= (\nabla\vec{e}_{S,T}, \nabla\vec{w}_T)_T - (\epsilon_{S,T}, \nabla\cdot\vec{w}_T)_T \\
&\leq |\vec{e}_{S,T}|_{1,T}|\vec{w}_T|_{1,T} + ||\epsilon_{S,T}||_{0,T}||\nabla\cdot\vec{w}_T||_{0,T} \\
&\leq \sqrt{2}|\vec{w}_T|_{1,T}(|\vec{e}_{S,T}|_{1,T} + ||\epsilon_{S,T}||_{0,T}) \\
&\leq C\frac{1}{h_T}||\vec{R}_T||_{0,T}\left(|\vec{e}_{S,T}|_{1,T}^2 + ||\epsilon_{S,T}||_{0,T}^2\right)^{1/2}
\end{aligned} \tag{3.45}$$

In addition, from the inverse inequalities, $||\vec{R}_T||_{0,T}^2 \leq C(\vec{R}_T, \vec{w}_T)_T$, and using (3.45),

$$h_T^2||\vec{R}_T||_{0,T}^2 \leq C\left(|\vec{e}_{S,T}|_{1,T}^2 + ||\epsilon_{S,T}||_{0,T}^2\right). \tag{3.46}$$

Next, we let $\vec{w}_E = \vec{R}_E b_E$ (b_E is an edge bubble function). Then, from (3.34) and using (3.46), (3.17), together with the estimate $|\vec{w}_E|_{1,T} \leq Ch_T^{-1}||\vec{w}_E||_{0,T}$, we get

$$\begin{aligned}
\left\langle\vec{R}_E, \vec{w}_E\right\rangle_E &= -(\nabla\vec{e}_{S,T}, \nabla\vec{w}_E)_T + (\epsilon_{S,T}, \nabla\cdot\vec{w}_E)_T + (\vec{R}_T, \vec{w}_E)_T \\
&\leq |\vec{e}_{S,T}|_{1,T}|\vec{w}_E|_{1,T} + ||\epsilon_{S,T}||_{0,T}||\nabla\cdot\vec{w}_E||_{0,T} + ||\vec{R}_T||_{0,T}||\vec{w}_E||_{0,T} \\
&\leq C|\vec{w}_E|_{1,T}(|\vec{e}_{S,T}|_{1,T} + ||\epsilon_{S,T}||_{0,T}) + Ch_T^{-1}(|\vec{e}_{S,T}|_{1,T} + ||\epsilon_{S,T}||_{0,T})||\vec{w}_E||_{0,T} \\
&\leq Ch_T^{-1}||\vec{w}_E||_{0,T}(|\vec{e}_{S,T}|_{1,T} + ||\epsilon_{S,T}||_{0,T}) \\
&\leq Ch_E^{-1/2}||\vec{R}_E||_{0,E}(|\vec{e}_{S,T}|_{1,T} + ||\epsilon_{S,T}||_{0,T}).
\end{aligned} \tag{3.47}$$

Then, using $||\vec{R}_E||_{0,E}^2 \leq C\langle\vec{R}_E, \vec{w}_E\rangle_E$ and (3.47),

$$h_E||\vec{R}_E||_{0,E}^2 \leq C(|\vec{e}_{S,T}|_{1,T}^2 + ||\epsilon_{S,T}||_{0,T}^2). \tag{3.48}$$

Finally, from (3.35), since $\nabla\cdot\vec{u}_h|_T \in Q_2(T)$ we have that

$$(\nabla\cdot\vec{e}_{S,T}, \nabla\cdot\vec{u}_h)_T = (\nabla\cdot\vec{u}_h, \nabla\cdot\vec{u}_h)_T,$$

$$||R_T||_{0,T} = ||\nabla\cdot\vec{u}_h||_{0,T} \leq ||\nabla\cdot\vec{e}_{S,T}||_{0,T} \leq \sqrt{2}|\vec{e}_{S,T}|_{1,T}. \tag{3.49}$$

Combining (3.46), (3.48) and (3.49), establishes the the upper bound in the equivalence relation. □

Remark 3.3.8 The fact that $\nabla \cdot \vec{u}_h|_T \in Q_2(T)$ is crucial for the last step above. If we wanted to extend this error estimation approach to other mixed approximations then we would simply need to ensure that the pressure correction space is big enough to contain the divergence of the original velocity space. The only difficulty with this is that we also have to ensure that the velocity correction space is big enough to ensure that the local inf-sup stability condition (3.36) is not compromised. Thus, if we wanted to develop a Stokes error estimator for the $\boldsymbol{P}_{2*}$–$\boldsymbol{P}_{-1}$ mixed approximation, then the first thing to do is to choose a pressure augmentation space that is big enough to contain the divergence of $\boldsymbol{P}_{2*}$ functions. The standard quadratic polynomial space $\boldsymbol{P}_2$ would work. We must then choose a velocity augmentation space that is big enough to ensure that the combination of augmented spaces is locally stable. This suggests using a reduced $\boldsymbol{P}_3$ space for velocities (that is, with the vertex basis functions removed).

The Stokes estimator leads to large dimensional local problems. For example, the dimension of the local Stokes problem that must be solved to estimate the error in the interior element in Fig. 3.1 is 33 × 33. Our next approach is much simpler and, as we will see in section 3.4, effective in estimating the error in practice.

3.3.3 A local Poisson problem estimator

The local Poisson problem estimator $\eta_P = \sqrt{\sum_{T \in T_h} \eta^2_{P,T}}$ can be derived from the locally stable Stokes estimator (3.34)–(3.35) as follows:

$$\eta^2_{P,T} = |\vec{e}_{P,T}|^2_{1,T} + \|\epsilon_{P,T}\|^2_{0,T}, \tag{3.50}$$

where, $(\vec{e}_{P,T}, \epsilon_{P,T}) \in \mathbf{Q}_T \times Q_2(T)$ satisfies

$$(\nabla \vec{e}_{P,T}, \nabla \vec{v})_T = (\vec{R}_T, \vec{v})_T - \sum_{E \in \mathcal{E}(T)} \langle \vec{R}_E, \vec{v} \rangle_E \quad \forall \vec{v} \in \mathbf{Q}_T, \tag{3.51}$$

$$(\epsilon_{P,T}, q) = (R_T, q)_T \quad \forall q \in Q_2(T). \tag{3.52}$$

This is much more appealing from a computational perspective. First, (3.51) decouples into a pair of local Poisson problems, each one of dimension 12 × 12 in the case of the interior element in Fig. 3.1. Second, since by construction $R_T = \nabla \cdot \vec{u}_h \in Q_2(T)$, the solution of (3.52) is immediate: $\epsilon_{P,T} = \nabla \cdot \vec{u}_h$. The theoretical justification for computing the Poisson estimator instead of the Stokes estimator is the following equivalence result.

Theorem 3.3.9 *Given that the spaces defining the Stokes estimator are locally* $\mathfrak{B}$*–stable, the estimator* $\eta_{P,T}$ *is equivalent to the Stokes estimator:* $c\,\eta_{S,T} \leq \eta_{P,T} \leq C\eta_{S,T}$.

Proof. The proof is a straightforward extension of [30, Thm 3.6]. We include it here for completeness. Combining (3.34), (3.35), (3.51), (3.52), for any $T \in T_h$ and $[\vec{v}, q] \in \mathbf{Q}_T \times Q_2(T)$ we get

$$\begin{aligned}(\nabla\vec{e}_{P,T}, \nabla\vec{v})_T - (\epsilon_{P,T}, q)_T &= (\vec{R}_T, \vec{v})_T - \sum_{E\in\mathcal{E}(T)} \left\langle \vec{R}_E, \vec{v}\right\rangle_E - (\nabla\cdot\vec{u}_h, q)_T \\ &= (\nabla\vec{e}_{S,T}, \nabla\vec{v})_T - (\epsilon_{S,T}, \nabla\cdot\vec{v})_T - (\nabla\cdot\vec{e}_{S,T}, q)_T \\ &= \mathfrak{B}((\vec{e}_{S,T}, \epsilon_{S,T}); (\vec{v}, q)). \qquad (3.53)\end{aligned}$$

Then, using the local $\mathfrak{B}$-stability (3.41) gives

$$\begin{aligned}|\vec{e}_{S,T}|_{1,T} + \|\epsilon_{S,T}\|_{0,T} &\leq \frac{1}{\gamma_B} \max_{(\vec{v},q)\in\mathbf{Q}_T\times Q_2(T)} \frac{\mathfrak{B}((\vec{e}_{S,T}, \epsilon_{S,T}); (\vec{v}, q))}{|\vec{v}|_{1,T} + \|q\|_{0,T}} \\ &= \frac{1}{\gamma_B} \max_{(\vec{v},q)\in\mathbf{Q}_T\times Q_2(T)} \frac{(\nabla\vec{e}_{P,T}, \nabla\vec{v})_T - (\epsilon_{P,T}, q)_T}{|\vec{v}|_{1,T} + \|q\|_{0,T}} \\ &\leq \frac{1}{\gamma_B} \max_{(\vec{v},q)\in\mathbf{Q}_T\times Q_2(T)} \frac{|\vec{e}_{P,T}|_{1,T}|\vec{v}|_{1,T} + \|\epsilon_{P,T}\|_{0,T}\|q\|_{0,T}}{|\vec{v}|_{1,T} + \|q\|_{0,T}} \\ &\leq \frac{1}{\gamma_B}(|\vec{e}_{P,T}|_{1,T} + \|\epsilon_{P,T}\|_{0,T}). \qquad (3.54)\end{aligned}$$

This establishes the lower bound in the equivalence relation. In order to show the upper bound, we take $\vec{v} \in \mathbf{Q}_T$, and then using (3.34) and (3.51) we get

$$\begin{aligned}(\nabla\vec{e}_{P,T}, \nabla\vec{v})_T &= (\vec{R}_T, \vec{v})_T - \sum_{E\in\mathcal{E}(T)} \left\langle \vec{R}_E, \vec{v}\right\rangle_E \\ &= (\nabla\vec{e}_{S,T}, \nabla\vec{v})_T - (\epsilon_{S,T}, \nabla\cdot\vec{v})_T. \qquad (3.55)\end{aligned}$$

Using (3.35) and (3.52) means that, for any $q \in Q_2(T)$,

$$(\epsilon_{P,T}, q)_T = (R_T, q)_T = (\nabla\cdot\vec{e}_{S,T}, q). \qquad (3.56)$$

Using (3.55) gives

$$\begin{aligned}
|\vec{e}_{P,T}|_{1,T} &= \max_{\vec{v}\in\mathbf{Q}_T} \frac{(\nabla\vec{e}_{P,T},\nabla\vec{v})_T}{|\vec{v}|_{1,T}} \\
&= \max_{\vec{v}\in\mathbf{Q}_T} \frac{(\nabla\vec{e}_{S,T},\nabla\vec{v})_T - (\epsilon_{S,T},\nabla\cdot\vec{v})_T}{|\vec{v}|_{1,T}} \\
&\leq \max_{\vec{v}\in\mathbf{Q}_T} \frac{|\vec{e}_{S,T}|_{1,T}|\vec{v}|_{1,T} + ||\epsilon_{S,T}||_{0,T}||\nabla\cdot\vec{v}||_{0,T}}{|\vec{v}|_{1,T}} \\
&\leq |\vec{e}_{S,T}|_{1,T} + \sqrt{2}||\epsilon_{S,T}||_{0,T}, \qquad (3.57)
\end{aligned}$$

and, using (3.56),

$$\begin{aligned}
||\epsilon_{P,T}||_{0,T} &= \max_{q\in Q_2(T)} \frac{(\epsilon_{P,T},q)_T}{||q||_{0,T}} \\
&= \max_{q\in Q_2(T)} \frac{(\nabla\cdot\vec{e}_{S,T},q)_T}{||q||_{0,T}} \\
&\leq \max_{q\in Q_2(T)} \frac{||\nabla\cdot\vec{e}_{S,T}||_{0,T}||q||_{0,T}}{||q||_{0,T}} \\
&= ||\nabla\cdot\vec{e}_{S,T}|| \leq \sqrt{2}\,|\vec{e}_{S,T}|_{1,T}. \qquad (3.58)
\end{aligned}$$

Finally, combining (3.57) with (3.58) gives the required upper bound. □

Remark 3.3.10 If we wanted to extend this error estimation approach to other mixed approximations then we simply need to ensure that the pressure correction space is big enough to contain the divergence of the original velocity space. The upshot of this is that the Poisson estimator is independent of the pressure approximation—we would also solve (3.51)–(3.52) if we wanted to estimate the error in a solution computed with Q_2–Q_1 or Q_2–P_0 approximation!

3.4 Computational Experiments

In this section two test problems are solved in order to compare the effectivity of three error estimation strategies: a modified residual estimator $\tilde{\eta}_R$, and the Poisson estimator η_P as implemented in the IFISS Matlab toolbox [43]; and a local recovery Z–Z estimator η_Z[1]

---

[1] The Z–Z estimator is introduced in [48]. In brief, we first post-process the velocity solution $\vec{u}_h$ to obtain a more accurate approximation $\vec{u}_h^\star$ in the sense that $\nabla\vec{u}_h^\star$ is more accurate than $\nabla\vec{u}_h$. Then, $\eta_{Z,T} := ||\nabla(\vec{u}_h^\star - \vec{u}_h)||_{0,T}$ and $\eta_Z := \sqrt{\sum_{T\in T_h}\eta_{Z,T}^2}$.

as implemented in the Oomph–lib package [26]. The modified residual error estimator was introduced by Houston et al. [27], and is defined as follows:

$$\tilde{\eta}_{R,T}^2 := \left(\frac{h_T}{2}\right)^2 ||\vec{R}_T||_{0,T}^2 + ||R_T||_{0,T}^2 + \sum_{E\in\mathcal{E}(T)} \frac{h_E}{2} ||\vec{R}_E||_{0,E}^2, \tag{3.59}$$

and $\tilde{\eta}_R := \sqrt{\sum_{T\in T_h} \tilde{\eta}_{R,T}^2}$. We focus on this modified residual estimator $\tilde{\eta}_R$ because our computational experience shows that $\tilde{\eta}_R$ is much more accurate than the standard residual estimator η_R. The Z–Z estimator is a popular error estimation strategy: it is also considered by practitioners to be one of the best in terms of its simplicity and reliability, especially when used as a refinement indicator in a self-adaptive refinement setting.

3.4.1 Test problem 1: a smooth solution

Our first test problem is hard-wired into the IFISS package [20, problem S4], and the velocity solution is a quartic polynomial:

$$\vec{u} = \begin{pmatrix} 20xy^3 \\ 5x^4 - 5y^4 \end{pmatrix}, \quad p = 60x^2y - 20y^3. \tag{3.60}$$

We solve the problem as an enclosed flow (that is $\partial\Omega_N = \emptyset$) with the boundary data $\vec{g}$ given by interpolating the exact flow solution at the nodes. We could account for the resulting "variational crime" by using the methodology introduced by Ainsworth & Kelly [2], but have not done so in the results reported below.[2] The flow problem is solved on a square domain $(-1, 1) \times (-1, 1)$ using a nested sequence of uniformly refined square grids. The coarsest grid is 8×8 and is associated with a mesh parameter of $h = 1/4$. To interpret the results that are presented some notation will be needed:

$$e = \sqrt{|\vec{u} - \vec{u}_h|_1^2 + ||p - p_h||_0^2}, \tag{3.61}$$

$$e_T = \sqrt{|\vec{u} - \vec{u}_h|_{1,T}^2 + ||p - p_h||_{0,T}^2}, \tag{3.62}$$

while e_{ω_T} is defined analogously to e_T. Looking first at Table 3.1, we see that the global error e is decreasing like $O(h^2)$ as expected. It is also evident that the Poisson problem

---

[2] This means that the error estimation is inaccurate for elements next to the boundary. These effects are evident in the estimated error plots in Fig. 3.2.

estimator η_P provides the most accurate estimate of the global error: $\frac{e}{\eta_P}$ is close to one, whereas $\tilde{\eta}_R$ is about twice the exact error and η_Z is about three times smaller than the exact error. Turning to Fig. 3.2 we see that all three error estimators seem to be able to correctly indicate the structure of the error, although the vertical scale may not be very accurate. As might be anticipated from the results in Table 3.1, the only estimator that is quantitatively close to the exact error is $\eta_{P,T}$.

Table 3.1: Comparison of error estimator effectivity.

h	e	$\frac{e}{\tilde{\eta}_R}$	$\frac{e}{\eta_P}$	$\frac{e}{\eta_Z}$
$\frac{1}{4}$	1.0278e+00	5.1508e-01	1.0909e+00	3.7098e+00
$\frac{1}{8}$	2.5569e-01	4.9210e-01	1.0189e+00	3.2837e+00
$\frac{1}{16}$	6.3825e-02	4.8148e-01	9.8762e-01	3.0741e+00
$\frac{1}{32}$	1.5950e-02	4.7638e-01	9.7317e-01	2.9737e+00

Table 3.2: Comparison of effectivity indices.

h	e	$\max_{T\in T_h}\frac{e_T}{e_{\omega_T}}$	$\max_{T\in T_h}\frac{\tilde{\eta}_{R,T}}{e_{\omega_T}}$	$\max_{T\in T_h}\frac{\eta_{P,T}}{e_{\omega_T}}$	$\max_{T\in T_h}\frac{\eta_{Z,T}}{e_{\omega_T}}$
$\frac{1}{4}$	1.0278e+00	6.3048e-01	1.1261e+00	5.2173e-01	1.9083e-01
$\frac{1}{8}$	2.5569e-01	6.0283e-01	1.1401e+00	5.2674e-01	2.2408e-01
$\frac{1}{16}$	6.3825e-02	5.8974e-01	1.1327e+00	5.2173e-01	2.3030e-01
$\frac{1}{32}$	1.5950e-02	5.8346e-01	1.1261e+00	5.1777e-01	2.3134e-01

It is instructive to look at the local error estimates in more detail. In general, if an error estimator is to be efficient then the constant on the right hand side of (3.13) should be bounded. An estimate of this constant (e.g. $\max_{T\in T_h}\frac{\tilde{\eta}_{R,T}}{e_{\omega_T}}$ for $\tilde{\eta}_R$) is provided in Table 3.2, where we also estimate this constant for the exact error ($\max_{T\in T_h}\frac{e_T}{e_{\omega_T}}$) and refer to it as the "exact value". From the table, although $\max_{T\in T_h}\frac{\tilde{\eta}_{R,T}}{e_{\omega_T}}$, $\max_{T\in T_h}\frac{\eta_{P,T}}{e_{\omega_T}}$ and $\max_{T\in T_h}\frac{\eta_{Z,T}}{e_{\omega_T}}$ all appear to be bounded, only $\max_{T\in T_h}\frac{\eta_{P,T}}{e_{\omega_T}}$ is close to the "exact value".

Ideally, the local effectivity indices (i.e. $\frac{\tilde{\eta}_{R,T}}{e_{\omega_T}}$ for $\tilde{\eta}_R$) will be bounded above and below across the whole domain, so that elements with large errors can be singled out for local

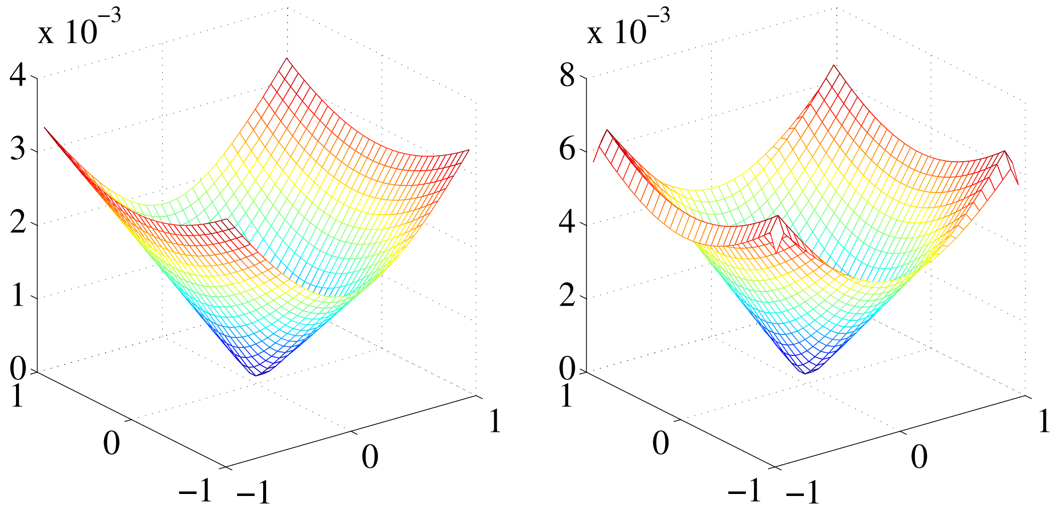

(a) Exact error: e_T (b) Estimator: $\tilde{\eta}_{R,T}$

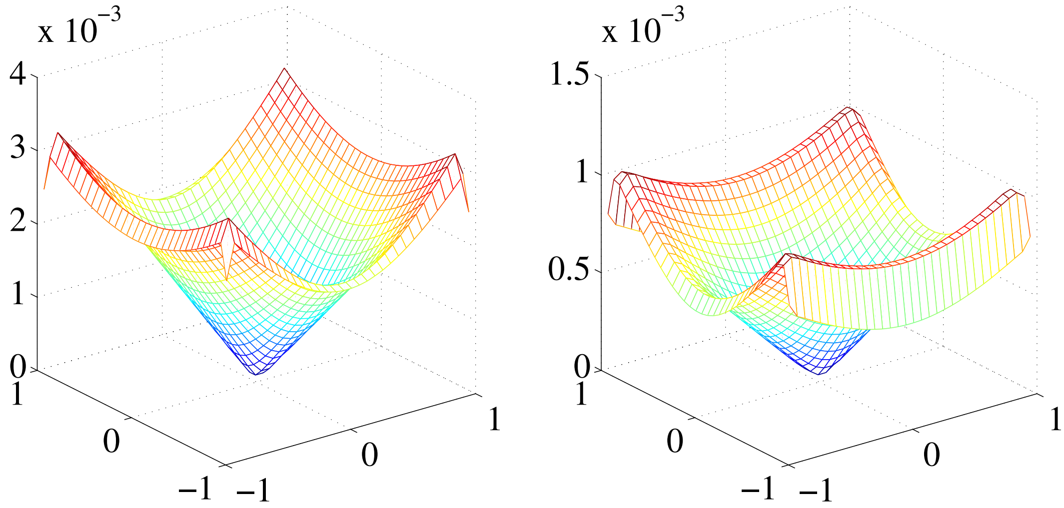

(c) Estimator: $\eta_{P,T}$ (d) Estimator: $\eta_{Z,T}$

Figure 3.2: The exact error and estimated errors for test problem 1 with $h = \frac{1}{16}$.

mesh refinement. This is assessed in Fig. 3.3. Looking at the distribution of these indices it is clear that $\eta_{P,T}$ and $\tilde{\eta}_{R,T}$ are closely aligned with the exact error but the Z–Z estimator is not. In particular the Z–Z estimator has relatively large local effectivity indices in the "wrong place", which could lead to the labelling of elements with small error for adaptive refinement.

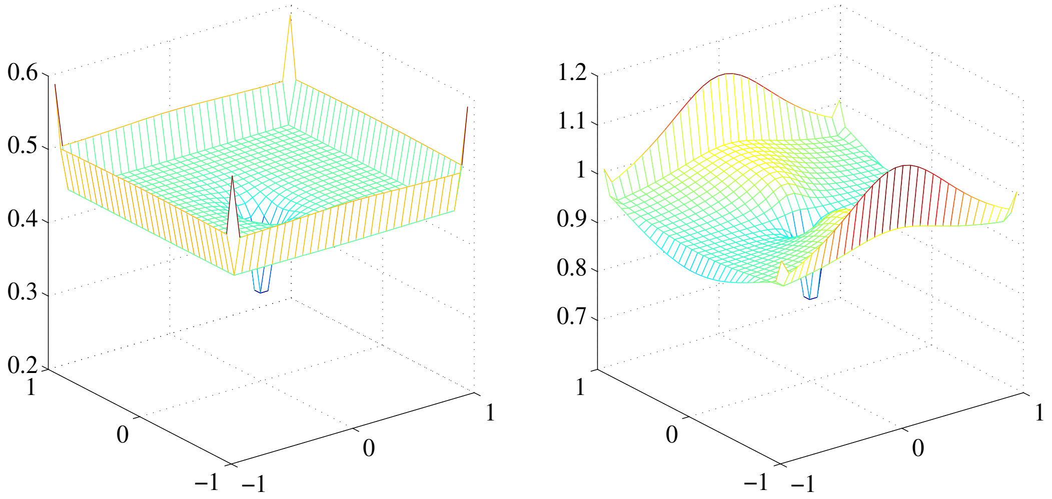

(a) Exact effectivity: $\frac{e_T}{e_{\omega_T}}$ (b) Estimator effectivity: $\frac{\tilde{\eta}_{R,T}}{e_{\omega_T}}$

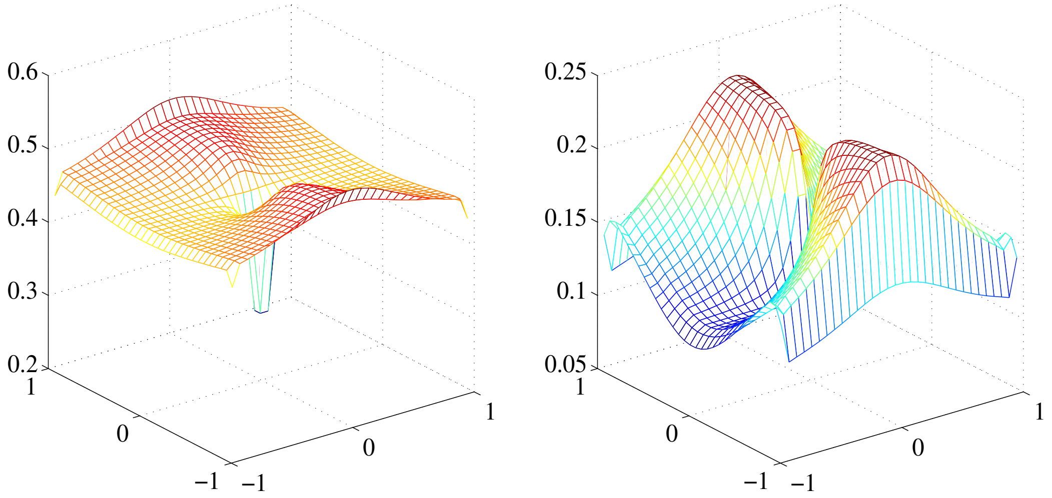

(c) Estimator effectivity: $\frac{\eta_{P,T}}{e_{\omega_T}}$ (d) Estimator effectivity: $\frac{\eta_{Z,T}}{e_{\omega_T}}$

Figure 3.3: The local effectivities of the exact error and the error estimators for test problem 1 with $h = \frac{1}{16}$.

3.4.2 Test problem 2: channel flow over a backward step

The second example is also hard-wired into the IFISS package [20, problem S2]. The flow domain is $(-1, 5) \times (-1, 1) \setminus (-1, 0] \times (-1, 0]$. A zero velocity condition applied at the top and bottom of the channel and fully-developed parabolic velocity profile is specified at the inflow boundary ($x = -1$). A natural boundary condition applies at the ouflow($x = 5$). Unlike the first problem, which has a perfectly smooth solution, this problem has a singularity at the re-entrant corner. We solve it using $\boldsymbol{Q}_2 - \boldsymbol{P}_{-1}$ approximation with a uniform square

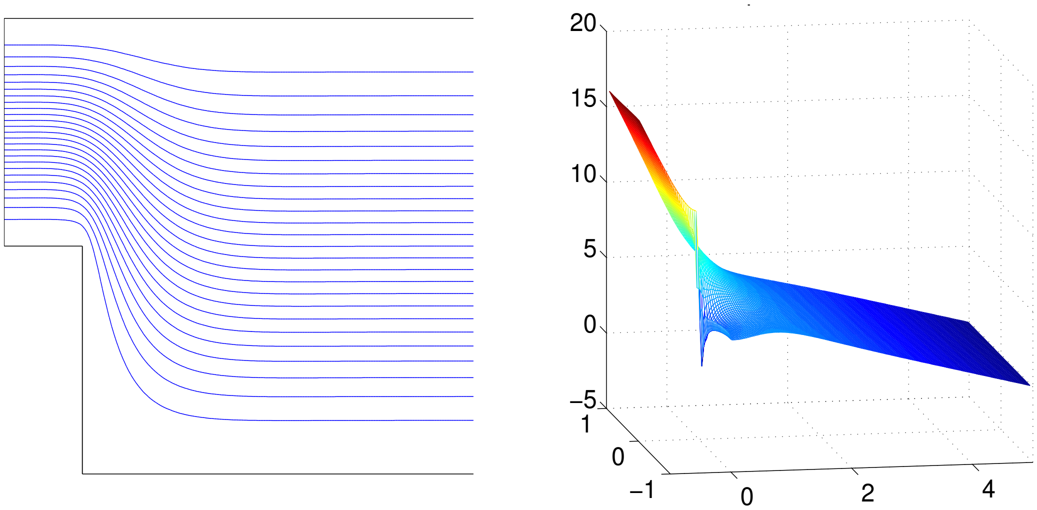

(a) Streamlines (equally spaced)

(b) Pressure distribution

Figure 3.4: The $Q_2 - P_{-1}$ solution of test problem 2 with $h = \frac{1}{16}$.

mesh (with $h = \frac{1}{16}$). The computed solution is shown in Fig. 3.4 and the profiles of the estimated error using our three estimators are shown in Fig. 3.5. All three have essentially the same structure—the estimated errors are dominated by the results in the elements close to the singularity. Their magnitudes are different however: the residual estimator is the largest, the Z–Z estimator is the smallest, and the local Poisson estimator is in the middle. This is consistent with the results obtained from the first test problem.

3.5 Conclusion

In this chapter, the following three error estimators for the $Q_2 - P_{-1}$ approximation are shown to be equivalent to the true discretisation error,

- the residual estimator η_R;
- the local Stokes problem estimator η_S;
- the local Poisson problem estimator η_P.

In these three estimators, the Poisson estimator η_P is the cheapest, and from numerical experiments, it is the most effective. Our numerical results also make it clear that a global upper bound and a local lower bound on the estimated error does not automatically lead to

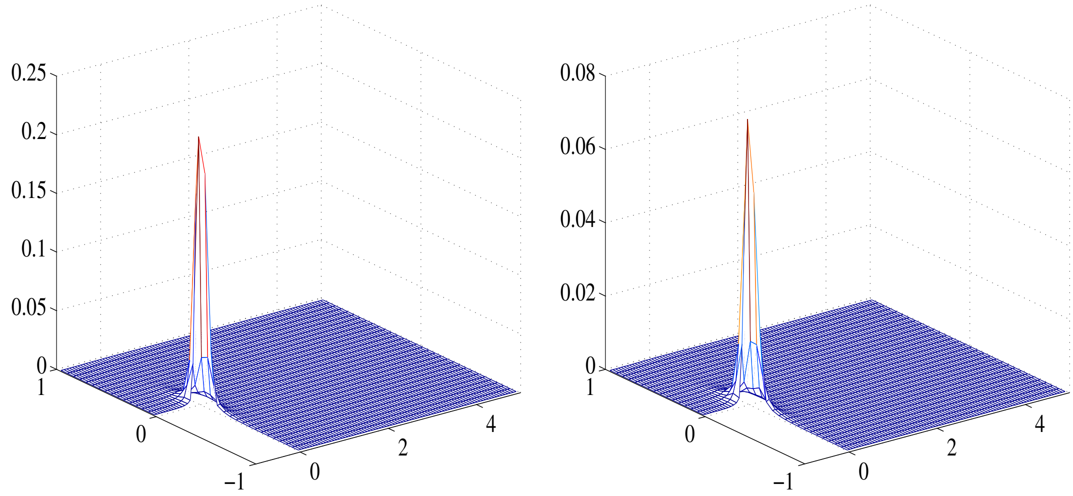

a) Estimator: $\tilde{\eta}_{R,T}$ (b) Estimator: $\eta_{P,T}$

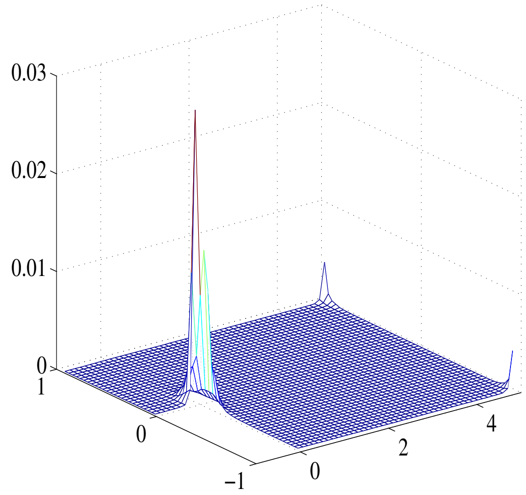

c) Estimator: $\eta_{Z,T}$

Figure 3.5: Estimated distribution of errors for test problem 2 with $h = \frac{1}{16}$.

an effective error estimator in an adaptive refinement setting. Although there is a theoretical guarantee that elements with large errors will be flagged by such an estimator, there is no guarantee that elements that are flagged as having a small discretization error actually have a small error in reality.

Chapter 4

Error Estimation for Mixed Approximations Associated with Anisotropic Meshes

For simplicity, this chapter only considers the Stokes problem (1.1)–(1.3) with a Dirichlet boundary condition ($\partial\Omega = \partial\Omega_D$). In Section 4.1, some further notation about domain partitionings will be introduced. This notation is necessarily needed in discussing error estimation for anisotropic meshes. Recent analysis results concerning inf-sup stable methods associated with anisotropic meshes will be reviewed in Section 4.2. Two numerical examples will be tested to verify these theories—the discrete inf-sup constant of inf-sup stable methods can degenerate as meshes become highly stretched. These numerical results then motivate us to use a stabilized $\boldsymbol{Q}_1 - \boldsymbol{P}_0$ method which will be introduced in Section 4.3. In this section, a robust a priori error bound for stabilized $\boldsymbol{Q}_1 - \boldsymbol{P}_0$ approximation associated with anisotropic meshes will be established. Finally, in Section 4.4, a posteriori error estimation for anisotropic meshes is briefly discussed. A new anisotropic local Poisson problem error estimator for stabilized $\boldsymbol{Q}_1 - \boldsymbol{P}_0$ approximation will be presented at the end of this section.

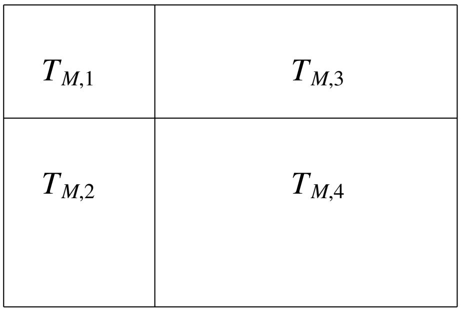

Figure 4.1: A 2 × 2 macroelement M.

4.1 Macroelement Nomenclature

A 2 × 2 macroelement is the union of four neighboring elements sharing a common vertex. Fig. 4.1 shows a macroelement M which consists of $T_{M,i}$, $i = 1 : 4$ ($\overline{M} = \cup_{i=1:4}\overline{T}_{M,i}$, $M = \overline{M} \setminus \partial\overline{M}$). For a rectangular partitioning T_h, T_M denotes its associated 2 × 2 macroelement partitioning. An example of a rectangular partitioning of a square domain with its associated macroelement partitioning is shown in Fig. 4.2. Note that throughout this chapter, we assume that any T_h has a unique 2 × 2 macroelement partitioning T_M associated with it. The framework of this chapter can be extended to more general meshes, e.g. the meshes based on 3 × 3 or 3 × 2 macroelements. For simplicity, a "macroelement" in the subsequent sections just means a 2 × 2 macroelement.

For a macroelement partitioning T_M, the following connectivity condition is assumed.

Definition 4.1.1 (Macroelement connectivity). *Let M_1 and M_2 be any two macroelements in T_M, and then $\overline{M}_1 \cap \overline{M}_2$ can only be an empty set, a single vertex, or two connected edges in $\mathcal{E}_h$.*

Another concept in this chapter is the element patch which is defined as follows.

Definition 4.1.2 (Element patch). *For a rectangular partitioning T_h, the closure of an element patch P is*

$$\overline{P} = \cup_{i\in\mathbb{N}_P}\overline{T}_i, \quad T_i \in T_h \text{ and } \cup_{\mathbb{N}_P}\overline{T}_i \text{ is connected and rectangular}, \tag{4.1}$$

where $\mathbb{N}_P$ is a subset of $\{1, 2, 3, ..., N\}$ (N is the number of elements in T_h). Then the element

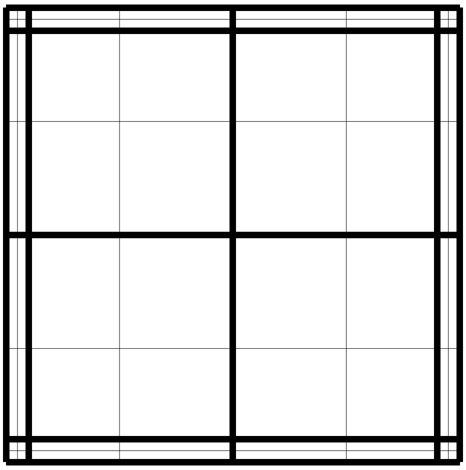

Figure 4.2: An example of an anisotropic rectangular partitioning T_h with its associated macroelement partitioning T_M shown by bold lines.

patch P is

$$P = \overline{P} \setminus \partial\overline{P}. \tag{4.2}$$

Note that a macroelement is an element patch. However, an element patch may not be a macroelement, since it has a more flexible topological structure. A patch partitioning associated with T_h denoted by T_P, is defined by insisting that any two different patches $P_1, P_2 \in T_P$ do not overlap. In other words, the mesh T_h can be considered to be refined from a patch partitioning T_P.

In stability analysis of inf-sup stable methods for anisotropic meshes[1] (see Section 4.2), patch regularity as defined below is typically required.

Definition 4.1.3 (Patch regularity). *A rectangular partitioning T_h is patch regular with respect to a patch partitioning T_P if the partitioning T_P is regular (no hanging nodes) and isotropic (its global aspect ratio is bounded by some moderate constant).*

The element patches are typically classified into three categories—the interior, edge and corner patches (P_I, P_E and P_C). These patches are defined to be the images of the reference patches ($\tilde{P}_I$, $\tilde{P}_E$ and $\tilde{P}_C$ which are partitionings of $(-1,1)^2$) by the affine map from $(-1,1)^2$ to each patch. The reference patches are defined as follows,

- $\tilde{P}_I$: an isotropic partitioning of $(-1,1)^2$;

---

[1] Note that a family of meshes is said to be isotropic if the global aspect ratios of the meshes in this family are bounded. Otherwise, the mesh family is anisotropic.

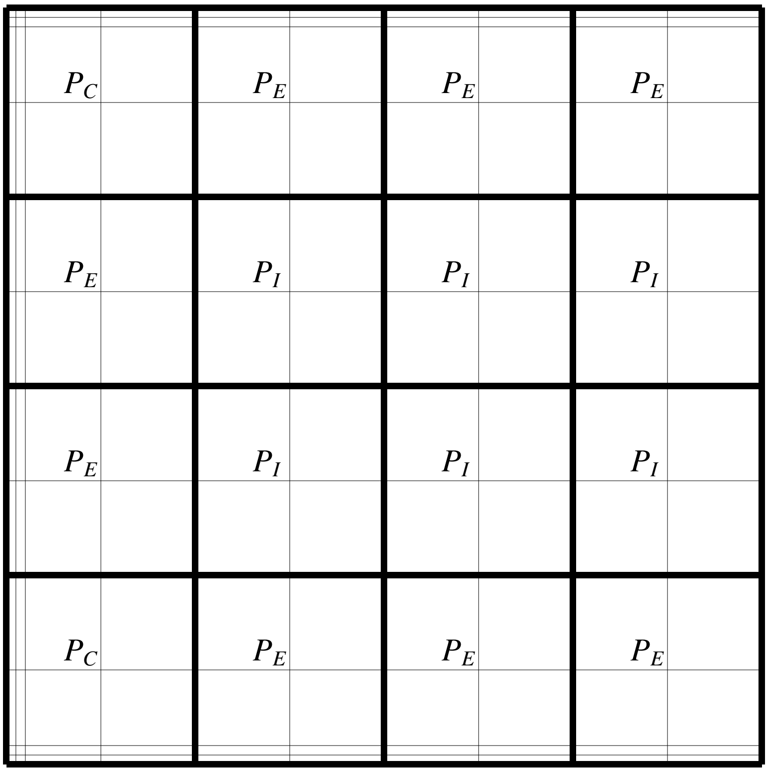

Figure 4.3: A mesh T_h and its associated patch partitioning T_P shown by bold lines (P_C denotes a corner patch, P_E denotes an edge patch and P_I denotes an interior patch).

- $\tilde{P}_E := K \times \tilde{K}$, where K is an arbitrary partitioning of $(-1, 1)$ while $\tilde{K}$ equally divides $(-1, 1)$ into two parts;
- $\tilde{P}_C := K_1 \times K_2$, where K_1 and K_2 are arbitrary partitionings of $(-1, 1)$.

Fig. 4.3 shows a mesh T_h which is patch regular with respect to T_P, and it shows patches P_I, P_E and P_C. Note that, the mesh in Fig. 4.2 is not patch regular with respect to T_M.

4.2 A Priori Error Estimates for inf-sup Stable Methods

4.2.1 Existing theories

Most of the previous literature on a priori error estimation for the Stokes problem associated with anisotropic meshes only considers inf-sup stable approximations. For this reason, we start by reviewing the existing theories for inf-sup stable methods.

As shown in (1.44), the inf-sup constant γ_h is a key component of the a priori error estimate for inf-sup stable methods. Ideally, we want γ_h to be bounded below whenever the mesh T_h becomes anisotropic. However, γ_h may be related to the aspect ratio ρ. The so-called patch technique [2] discussed in Girault and Raviart [24, pp.129–132] is typically used to analyze the stability of inf-sup stable methods on anisotropic meshes. If a family of anisotropic rectangular meshes is assumed to be patch regular with respect to some fixed patch partitioning T_P, then the constant γ_h associated with $X_0^h \times M^h$ is bounded below in this family if in addition, the mixed approximation satisfies the following two conditions:

- On each $P \in T_P$, the local inf-sup constant is bounded below. The local inf-sup constant γ_L is defined as follows

$$\min_{0 \neq q_h \in M^h(P)} \max_{\vec{0} \neq \vec{v}_h \in X_0^h(P)} \frac{|(q_h, \nabla \cdot \vec{v}_h)|}{|\vec{v}_h|_1 \, \|q_h\|_0} = \gamma_L > 0, \tag{4.3}$$

  where $X_0^h(P) = X_0^h|_P \cap H_0^1(P)^2$ and $M^h(P) = M^h|_P \cap L_0^2(P)$. Note that

$$X_0^h|_P = \left\{ \vec{v} \,\middle|\, \vec{v} = \vec{w}|_P, \, \forall \vec{w} \in X_0^h \right\}, \quad M^h|_P = \left\{ q \,\middle|\, q = q'|_P, \forall q' \in M^h \right\}. \tag{4.4}$$

- The inf-sup constant for the spaces X_0^h and $\tilde{M}_h$, where $\tilde{M}_h = \{q| \, q \in L_0^2(\Omega), q|_P \in Q_0(P), \forall P \in T_P\}$, is also bounded below.

For any mixed method, we can choose T_P to ensure that the second condition holds. So, the main issue is the first condition, which is just a local problem on each patch. Schötzau and Schwab [39] proved the local inf-sup constant of $Q_{k+1} - Q_{k-1}$ approximations is bounded below for edge patches P_E, but did not establish stability for arbitrarily anisotropic corner patches P_C. In order to avoid constructing patches P_C, we need to design anisotropic meshes properly. For instance, in some specific mesh cases, we can use the quadrilateral corner patch shown in Fig. 4.4(b) instead of the simple corner patch shown in Fig. 4.4(a). In more general situations, some methods for designing stretched meshes are suggested in [39]. However, the mesh design techniques in [39] are complicated to implement. In subsequent work, Schötzau et al [40] showed that the $Q_{k+1} - Q_{k-1}$ approximations are stable for the family of anisotropic rectangular partitionings containing P_E with hanging nodes. This leads to a more practical implementation.

---

[2] The patch technique is referred to as the macroelement technique in this book and elsewhere in the literature, e.g. [39]. However, the notation of a macroelement in the literature is referred to as the element patch in this thesis, since we used the word “macroelement” in a different way in Section 4.1.

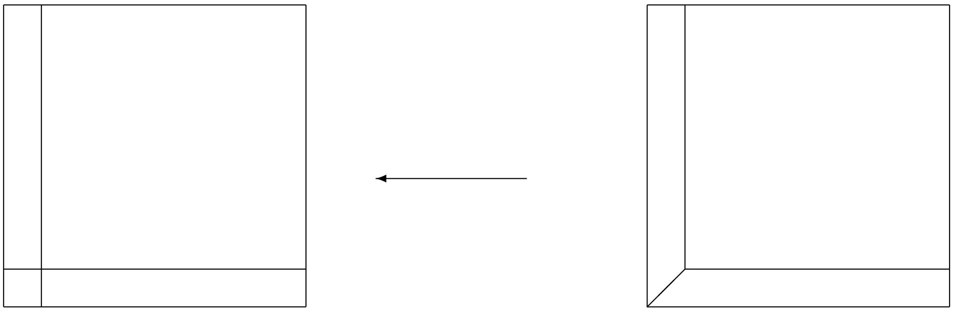

(a) A simple P_C (b) A quadrilateral corner patch

Figure 4.4: An example for avoiding P_C.

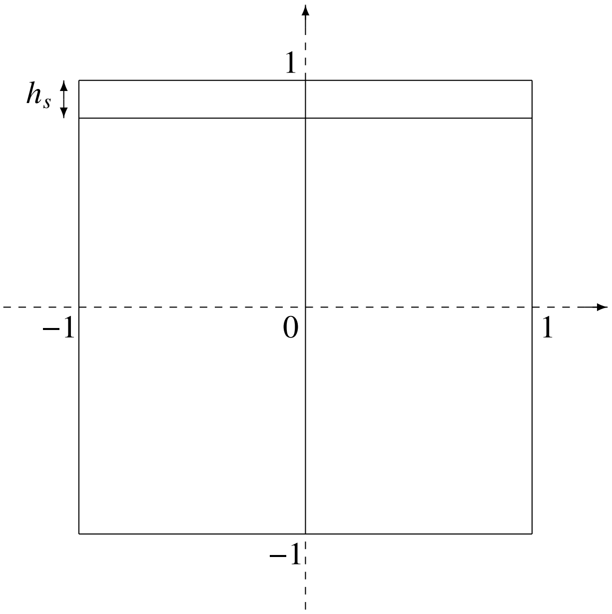

Figure 4.5: The reference edge macroelement (degenerates as $h_s \to 0$).

Nevertheless, in order to simplify mesh design techniques, corner patches play an important role, e.g. in the mesh shown in Fig. 4.3. So, it is of interest to see how the local inf-sup constant behaves for corner patches, which will be discussed in detail in the next section.

4.2.2 Some new results

For simplicity, this section considers two meshes consisting of only four elements. These are shown in Fig. 4.5 and Fig. 4.6. The mesh in Fig. 4.5 is called the reference edge macroelement, while the mesh in Fig. 4.6 is called the reference corner macroelement. As these two meshes become highly stretched ($h_s \to 0$), the eigenvalues of the generalized

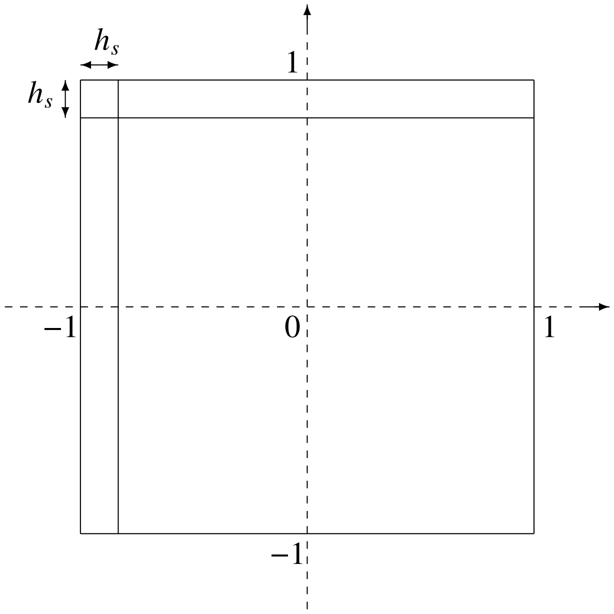

Figure 4.6: The reference corner macroelement (degenerates as $h_s \to 0$).

eigenvalue problem (1.41) associated with the $\boldsymbol{Q}_2{-}\boldsymbol{P}_0$, $\boldsymbol{Q}_2{-}\boldsymbol{P}_{-1}$, and $\boldsymbol{Q}_2{-}\boldsymbol{Q}_1$ approximations are tabulated in Tables 4.1 to 4.6. In addition, 0* in these tables implies some number which is close to the unit roundoff 10^{-15}.

Table 4.1: Eigenvalues in (1.41), $\boldsymbol{Q}_2 - \boldsymbol{P}_0$ on the reference edge macroelement.

h_s	0.1000	0.0100	0.0010	0.0001	1e-5
eigenvalues	0*	0*	0*	0*	0*
	0.4476	0.4793	0.4817	0.4819	0.4819
	0.6939	0.8123	0.8311	0.8331	0.8333
	0.7738	0.8742	0.8874	0.8887	0.8889

From Table 4.1, the inf-sup constant of the $\boldsymbol{Q}_2{-}\boldsymbol{P}_0$ approximation is obviously bounded below for the reference edge macroelement (its λ_2 is independent of h_s), which is consistent with the theoretical results in [39]. Table 4.2 shows that the inf-sup constant of the $\boldsymbol{Q}_2-\boldsymbol{P}_{-1}$ approximation goes to zero as $h_s \to 0$. Also, from Table 4.3, the inf-sup constant of the $\boldsymbol{Q}_2 - \boldsymbol{Q}_1$ approximation is bounded for the reference edge macroelement.

For the reference corner macroelement, we see that the inf-sup constants of all these methods are not bounded below (see Tables 4.4 to 4.6).

These tables also show that the other eigenvalues $\lambda_i,\ i = 3 : n_p$ are bounded below for all three approximations and both of these reference macroelements. This implies that

Table 4.2: Eigenvalues in (1.41), $\boldsymbol{Q}_2 - \boldsymbol{P}_{-1}$ on the reference edge macroelement.

h_s	0.1000	0.0100	0.0010	0.0001	1e-5
eigenvalues	0*	0*	0*	0*	0*
	0.0448	0.0008	0.0000	0.0000	0.0000
	0.2505	0.1790	0.1680	0.1668	0.1667
	0.2892	0.4142	0.4154	0.4155	0.4155
	0.3986	0.4149	0.4175	0.4177	0.4177
	0.4345	0.5071	0.5499	0.5550	0.5555
	0.6872	0.6760	0.6680	0.6668	0.6667
	0.6934	0.7685	0.7730	0.7732	0.7733
	0.8275	0.8285	0.8326	0.8333	0.8333
	0.8480	0.8333	0.8333	0.8333	0.8333
	0.8849	0.8888	0.8889	0.8889	0.8889
	0.9459	0.9931	0.9993	0.9999	1.0000

Table 4.3: Eigenvalues in (1.41), $\boldsymbol{Q}_2 - \boldsymbol{Q}_1$ on the reference edge macroelement.

h_s	0.1000	0.0100	0.0010	0.0001	1e-5
eigenvalues	0*	0*	0*	0*	0*
	0.1352	0.0536	0.0417	0.0405	0.0404
	0.1619	0.1294	0.1254	0.1250	0.1250
	0.3548	0.4145	0.4174	0.4176	0.4177
	0.3815	0.5006	0.4981	0.4978	0.4978
	0.5232	0.5185	0.5514	0.5551	0.5555
	0.5872	0.6184	0.6243	0.6249	0.6250
	0.7014	0.6748	0.6677	0.6668	0.6667
	0.9740	0.9964	0.9996	1.0000	1.0000

Table 4.4: Eigenvalues in (1.41), $\boldsymbol{Q}_2 - \boldsymbol{P}_0$ on the reference corner macroelement.

h_s	0.1000	0.0100	0.0010	0.0001	1e-5
eigenvalues	0*	0*	0*	0*	0*
	0.1343	0.0160	0.0016	0.0002	0.0000
	0.7645	0.8502	0.8600	0.8610	0.8611
	0.8099	0.8556	0.8606	0.8611	0.8611

Table 4.5: Eigenvalues in (1.41), $Q_2 - P_{-1}$ on the reference corner macroelement.

h_s	0.1000	0.0100	0.0010	0.0001	1e-5
eigenvalues	0*	0*	0*	0*	0*
	0.0575	0.0066	0.0007	0.0001	0.0000
	0.2418	0.3012	0.3146	0.3162	0.3163
	0.2678	0.3061	0.3152	0.3162	0.3163
	0.4385	0.4198	0.4170	0.4167	0.4167
	0.4455	0.4199	0.4170	0.4167	0.4167
	0.5023	0.4305	0.4182	0.4168	0.4167
	0.5031	0.4309	0.4182	0.4168	0.4167
	0.8237	0.8719	0.8775	0.8780	0.8781
	0.8828	0.8789	0.8782	0.8781	0.8781
	0.8851	0.8886	0.8889	0.8889	0.8889
	0.8869	0.8886	0.8889	0.8889	0.8889

Table 4.6: Eigenvalues in (1.41), $Q_2 - Q_1$ on the reference corner macroelement.

h_s	0.1000	0.0100	0.0010	0.0001	1e-5
eigenvalues	0*	0*	0*	0*	0*
	0.0717	0.0083	0.0008	0.0001	0.0000
	0.1723	0.1581	0.1564	0.1563	0.1563
	0.3261	0.3728	0.3847	0.3864	0.3866
	0.3267	0.3733	0.3848	0.3864	0.3866
	0.4805	0.4303	0.4185	0.4169	0.4167
	0.4824	0.4310	0.4186	0.4169	0.4167
	0.8480	0.8925	0.8975	0.8980	0.8981
	0.9144	0.8999	0.8983	0.8981	0.8981

the pressure Schur complement system $BA^{-1}B^T$ has only one degenerate eigenvalue and associated “pressure mode”.

From Definition 1.5.1, computing the inf-sup constant takes the maximum with respect to the velocity approximation space X_0^h and the minimum with respect to the pressure approximation space M^h. So, if X_0^h is enlarged or M^h is reduced properly such that the degenerate pressure mode of the Schur complement system is removed, the inf-sup constant can then be bounded. In Ainsworth and Coggins [1], some efficient methods to enhance the space X_0^h with high order polynomials are introduced. However, the degrees of the additional polynomials to enhance the space X_0^h are of order $\rho^{1/2}$ (see [1]). As a result, when the aspect ratio ρ is very large, the degrees of these additional polynomials are quite high, which may cause difficulties in practical implementation.

We would like to conclude this section by mentioning the point that, the role of the inf-sup constant in the a priori error estimate is unclear. In may cases, when the inf-sup constant decreases, the exact error does not increase. For instance, from our numerical experience, the exact errors of inf-sup stable approximations for the Stokes problem posed on the reference edge and corner macroelements do not go up, as their inf-sup constants degenerate. However, the a priori error bound (the right hand side of (1.44)) can rapidly increase due to the degeneration of the inf-sup constant, which implies that the a priori error bound is ineffective. In the next section, we will establish a robust a priori error bound for a local jump stabilized $\boldsymbol{Q}_1 - \boldsymbol{P}_0$ approximation for anisotropic meshes.

4.3 A Priori Error Estimate for a Stabilized Method

4.3.1 Motivation for using the $\boldsymbol{Q}_1 - \boldsymbol{P}_0$ approximation

For the right hand side of (1.44), using some proper interpolation for $\vec{u}$ and p, the convergence rates of inf-sup stable methods can be seen clearly. Using the $\boldsymbol{Q}_2 - \boldsymbol{Q}_1$ approximation for instance, whenever the exact solution $(\vec{u}, p)$ is in $\boldsymbol{H}_E^3 \times H^2(\Omega)$, employing the stretched Lagrange interpolation bound introduced in Apel [4, p.69], the following a priori error estimate holds,

$$||\vec{u} - \vec{u}_h||_1 + ||p - p_h||_0 \le \tilde{C} \sum_{T \in T_h} \sum_{|\alpha|=2} h_T^{\alpha} \{|D^{\alpha}\vec{u}|_{1,T} + ||D^{\alpha}p||_{0,T}\}, \tag{4.5}$$

where $\alpha = (\alpha_1, \alpha_2) \in \mathbb{N}_0^2$, $|\alpha| = \alpha_1 + \alpha_2$, $h_T^{\alpha} = h_{T,x}^{\alpha_1} h_{T,y}^{\alpha_2}$ and $D^{\alpha}(\cdot) = \frac{\partial^{\alpha_1}(\cdot)}{\partial x^{\alpha_1}} \frac{\partial^{\alpha_2}(\cdot)}{\partial y^{\alpha_2}}$.

However, the exact solutions $(\vec{u}, p)$ are not in $\boldsymbol{H}^3 \times H^2(\Omega)$ in many situations, e.g. the flow in a step domain. In these situations, higher order methods do not lead to higher accuracy. Thus, the $\boldsymbol{Q}_1 - \boldsymbol{P}_0$ approximation is more competitive.

Throughout this section, the spaces X_0^h, X_E^h and M^h represent the approximation spaces for $\boldsymbol{Q}_1 - \boldsymbol{P}_0$ approximation. The $\boldsymbol{Q}_1 - \boldsymbol{P}_0$ approximation is an inf-sup unstable method, because of the checkboard pressure mode (more information is given in [21, pp.235-237]). In order to make the problem (1.34)–(1.35) with the $\boldsymbol{Q}_1 - \boldsymbol{P}_0$ approximation uniquely solvable, stabilization is needed.

A number of stabilization methods for inf-sup unstable approximations have been developed during the last three decades. These methods can be classified into two kinds. The first one is residual based stabilization, e.g. the absolutely stabilized method introduced by Douglas and Wang [18] and the Galerkin least square methods introduced by Franca and Hughes [22]. The other one consists of pressure stabilized methods, e.g. the global pressure jump stabilized method (see Hughes and Franca [28]) and the local jump stabilized method (see Kechkar and Silvester [31]).

Since residual based stabilization typically needs to compute the momentum residual $(\vec{f} - \nabla^2\vec{u}_h + \nabla p_h)_T$, they are not appropriate for the $\boldsymbol{Q}_1 - \boldsymbol{P}_0$ approximation where $\nabla^2\vec{u}_h$ and ∇p_h are both zero. As discussed in [31], the global jump stabilized approximation is complicated to implement in parallel. So, the local jump stabilized method is adopted in this thesis.

The locally stabilized method [31] is to solve the following problem instead of (1.34)–(1.35): find $\vec{u}_h \in X_E^h$ and $p_h \in M^h$, such that

$$\int_\Omega \nabla\vec{u}_h : \nabla\vec{v}_h - \int_\Omega p_h \nabla \cdot \vec{v}_h = \int_\Omega \vec{f} \cdot \vec{v}_h \quad \forall \vec{v}_h \in X_0^h, \tag{4.6}$$

$$-\int_\Omega q_h \nabla \cdot \vec{u}_h - \frac{1}{4}\Upsilon(p_h, q_h) = 0 \quad \forall q_h \in M^h, \tag{4.7}$$

where the jump stabilization term $\Upsilon(\cdot,\cdot)$ (defined in [21, p.259]) is as follows,

$$\Upsilon_M(p_h, q_h) := \frac{|M|}{4} \sum_{E\in\Gamma_M} \frac{1}{h_E} \int_E [\![p_h]\!]_E [\![q_h]\!]_E, \tag{4.8}$$

$$\Upsilon(p_h, q_h) := \sum_{M\in T_M} \Upsilon_M(p_h, q_h), \tag{4.9}$$

where Γ_M is the set consisting of the four interior element edges in the macroelement M, T_M is a macroelement partitioning of the domain Ω, $[\![\cdot]\!]_E$ is the jump across edge E and h_E is the length of E. In addition, Υ_M defined in (4.8) is called the local jump stabilization term.

4.3.2 Theoretical analysis

For the global jump stabilized $\boldsymbol{Q}_1 - P_0$ approximation in [18], Becker [10] has established an a priori error estimate for anisotropic meshes. However, the result in [10] requires the global grading factor κ of meshes to be bounded, which may cause inconvenience for adaptive mesh refinement.

In this section, we assume the rectangular partitioning to be T_M uniform, which is defined as follows.

Definition 4.3.1 **(T_M uniformity).** *A rectangular mesh T_h is T_M uniform if T_h is associated with a unique macroelement partitioning T_M which satisfies the connectivity condition, and all the four elements included in any macroelement $M \in T_M$ have the same size.*

Note that T_M uniformity is just a local requirement, and it allows meshes to have arbitrarily large global aspect ratio and grading factor.

In order to state the main theorems, the following bilinear forms need to be introduced.

Definition 4.3.2 *The big bilinear form $\mathfrak{B}_h : (\boldsymbol{H}^1, L^2(\Omega)) \times (\boldsymbol{H}^1, L^2(\Omega)) \to \mathbb{R}$ is:*

$$\mathfrak{B}_h((\vec{u}, p); (\vec{v}, q)) = (\nabla\vec{u}, \nabla\vec{v}) - (p, \nabla\cdot\vec{v}) - (q, \nabla\cdot\vec{u}) - \tfrac{1}{4}\Upsilon(p, q), \tag{4.10}$$

and $\mathfrak{B} : (\boldsymbol{H}^1, L^2(\Omega)) \times (\boldsymbol{H}^1, L^2(\Omega)) \to \mathbb{R}$ is (also see Section 3.2):

$$\mathfrak{B}((\vec{u}, p); (\vec{v}, q)) = (\nabla\vec{u}, \nabla\vec{v}) - (p, \nabla\cdot\vec{v}) - (q, \nabla\cdot\vec{u}). \tag{4.11}$$

Obviously, the bilinear form $\mathfrak{B}$ is continuous from $(\boldsymbol{H}^1, L^2(\Omega)) \times (\boldsymbol{H}^1, L^2(\Omega)) \to \mathbb{R}$. This continuity is used in the a priori error estimates for stable methods [21, p.253]). However, it is not obvious if $\mathfrak{B}_h$ is continuous from $(\boldsymbol{H}^1, L^2(\Omega)) \times (\boldsymbol{H}^1, L^2(\Omega)) \to \mathbb{R}$, because of the jump stabilization term Υ.

Lemma 4.3.3 *Let M be a 2×2 macroelement with the four included elements having the same size. The following inequality holds,*

$$\Upsilon_M(q, q) \geq 2\|q\|_{0,M}^2 \quad \forall q \in \boldsymbol{P}_{0,M}, \tag{4.12}$$

where $\boldsymbol{P}_{0,M} := \{q, q|_T \in \boldsymbol{P}_0(T), \forall T \subset M\} \cap L_0^2(M)$, and Υ_M is the local jump stabilization term defined in (4.8).

Proof. Let

$$C^\star = \begin{pmatrix} 2 & -1 & 0 & -1 \\ -1 & 2 & -1 & 0 \\ 0 & -1 & 2 & -1 \\ -1 & 0 & -1 & 2 \end{pmatrix}. \tag{4.13}$$

Any $q \in \boldsymbol{P}_{0,M}$ can be expressed as the following vector form,

$$\vec{q} = \begin{pmatrix} q_{M,1} \\ q_{M,2} \\ q_{M,3} \\ q_{M,4} \end{pmatrix}, \tag{4.14}$$

where $q_{M,i} = q|_{M_i}$, $i = 1:4$ (M_i are the four elements included in M).

The eigenvalues and eigenvectors of $C^\star$ are

$$\{0, \mathbf{q_1}\}, \quad \{2, \mathbf{q_2}\}, \quad \{2, \mathbf{q_3}\}, \quad \{4, \mathbf{q_4}\}, \tag{4.15}$$

where

$$\mathbf{q_1} = \begin{pmatrix} 1 \\ 1 \\ 1 \\ 1 \end{pmatrix}, \mathbf{q_2} = \begin{pmatrix} 1 \\ 0 \\ -1 \\ 0 \end{pmatrix}, \mathbf{q_3} = \begin{pmatrix} 0 \\ 1 \\ 0 \\ -1 \end{pmatrix}, \mathbf{q_1} = \begin{pmatrix} -1 \\ 1 \\ -1 \\ 1 \end{pmatrix}. \tag{4.16}$$

Since $\{\mathbf{q_i}\}_{i=1}^4$ are linear independent, the vector $\vec{q}$ can be expressed uniquely as

$$\vec{q} = \alpha_1 \mathbf{q_1} + \alpha_2 \mathbf{q_2} + \alpha_3 \mathbf{q_3} + \alpha_4 \mathbf{q_4}, \quad \alpha_i \in \mathbb{R}. \tag{4.17}$$

Note that since $q \in P_{0,M}$, $\sum_{i=1:4} q_{M,i} = 0$. From (4.16), all the eigenvectors except $\mathbf{q_1}$ have zero means. Thus, the contribution of $\mathbf{q_1}$ in (4.17) is zero ($\alpha_1 = 0$).

From the definition of Υ_M and due to $\alpha_1 = 0$ in (4.17),

$$\Upsilon_M(q,q) = \vec{q}^T \frac{1}{4}|M|C^\star \vec{q} \geq \frac{1}{4}|M|\lambda_2 \vec{q}^T \vec{q}, \tag{4.18}$$

where $\lambda_2 = 2$ is the smallest nontrivial eigenvalue of the matrix $C^\star$. In addition,

$$||q||_{0,M}^2 = \sum_{i=1}^{4} q_{M,i}^2 |T_{M,i}| = \frac{1}{4}|M|\vec{q}^T \vec{q}. \tag{4.19}$$

From (4.18)–(4.19), we get

$$\Upsilon_M(q,q) \geq 2||q||_{0,M}^2 \quad \forall q \in \boldsymbol{P}_{0,M}.$$

□

Using Lemma 4.3.3, for any $q_h \in M^h$,

$$\begin{aligned} \Upsilon(q_h, q_h) &= \Upsilon(q_h - \Pi_h q_h, q_h - \Pi_h q_h) \\ &= \sum_{M \in T_M} \Upsilon_M(q_h - \Pi_h q_h, q_h - \Pi_h q_h) \\ &\geq 2||q_h - \Pi_h q_h||_0^2, \end{aligned} \tag{4.20}$$

where $\Pi_h p|_M = \frac{\int_M p}{|M|}, \forall M \in T_M$.

Following the proofs in [31], and using the connectivity condition of T_M and (4.20), the following lemma can be obtained.

Lemma 4.3.4 *For all $(\vec{v}_h, q_h) \in X_0^h \times M^h$, when the mesh T_h is T_M uniform, there exists a constant ξ which is independent of h, ρ and κ such that*

$$\sup_{(\vec{w}_h, r_h) \in X_0^h \times M^h} \frac{\mathfrak{B}_h((\vec{v}_h, q_h); (\vec{w}_h, r_h))}{||\vec{w}_h||_1 + ||r_h||_0} \geq \xi(||\vec{v}_h||_1 + ||q_h||_0). \tag{4.21}$$

Note that, (4.21) is referred to as $\mathfrak{B}_h$-stability.

With the above lemmas, Theorem 4.3.5 can then be stated. The proof needs $\mathfrak{B}_h$-stability (4.21).

Theorem 4.3.5 *Let the partitioning T_h of Ω be T_M uniform. Let $(\vec{u}_h, p_h)$ be the solution of the stabilized $\boldsymbol{Q}_1 - \boldsymbol{P}_0$ approximation (4.6)–(4.7), and $(\vec{u}, p) \in \boldsymbol{H}^2 \cap C^0(\overline{\Omega})^2 \times \boldsymbol{H}^1 \cap C^0(\overline{\Omega})$ be the solution of (1.18)–(1.19). Then, there exists a constant C_0, independent of the mesh size h and the global aspect ratio ρ and the global grading factor κ, such that,*

$$\begin{aligned} \|\vec{u} - \vec{u}_h\|_1 + \|p - p_h\|_0 \;\leq\; & C_0 \sum_{T \in T_h} \Big\{ h_{T,x} \|\vec{u}_{xx}\|_{0,T} + \max(h_{T,x}, h_{T,y}) \|\vec{u}_{xy}\|_{0,T} \\ & + h_{T,y} \|\vec{u}_{yy}\|_{0,T} + h_{T,x} \|p_x\|_{0,T} + h_{T,y} \|p_y\|_{0,T} \Big\}. \end{aligned} \tag{4.22}$$

Proof. First, note that the generic constant C in this proof is independent of h, ρ and κ. Let $\vec{u}_I$ be the Lagrange interpolant of $\vec{u}$ in X_E^h agreeing with $\vec{u}$ at the vertices of rectangles in T_h, and p_I be the L^2 projection of p in M^h. From Apel [4, p.69], and Apel and Randrianarivony [5], we have

$$\|\vec{u} - \vec{u}_I\|_1 \leq C \sum_{T \in T_h} \left\{ \sum_{|\alpha|=1} h_T^\alpha |D^\alpha \vec{u}|_{1,T} \right\} \tag{4.23}$$

$$\|p - p_I\|_0 \leq C \sum_{T \in T_h} \left\{ \sum_{|\alpha|=1} h_T^\alpha \|D^\alpha p\|_{0,T} \right\}. \tag{4.24}$$

$|\alpha| = \alpha_1 + \alpha_2$, $h_T^\alpha = h_{T,x}^{\alpha_1} h_{T,y}^{\alpha_2}$ and $D^\alpha(\cdot) = \frac{\partial^{\alpha_1}(\cdot)}{\partial x^{\alpha_1}} \frac{\partial^{\alpha_2}(\cdot)}{\partial y^{\alpha_2}}$.

Then, for all $(\vec{w}_h, r_h) \in X_0^h \times M^h$,

$$\begin{aligned} \mathfrak{B}_h((\vec{u}_h - \vec{u}_I, p_h - p_I); (\vec{w}_h, r_h)) &= \mathfrak{B}_h((\vec{u}_h, p_h); (\vec{w}_h, r_h)) - \mathfrak{B}((\vec{u}_I, p_I); (\vec{w}_h, r_h)) + \frac{1}{4}\Upsilon(p_I, r_h) \\ &= \mathfrak{B}((\vec{u}, p); (\vec{w}_h, r_h)) - \mathfrak{B}((\vec{u}_I, p_I); (\vec{w}_h, r_h)) + \frac{1}{4}\Upsilon(p_I, r_h) \\ &= \mathfrak{B}((\vec{u} - \vec{u}_I, p - p_I); (\vec{w}_h, r_h)) + \frac{1}{4}\Upsilon(p_I, r_h). \end{aligned} \tag{4.25}$$

Since $\vec{u}_h - \vec{u}_I \in X_0^h$ and $p_h - p_I \in M^h$, using the $\mathfrak{B}_h$-stability (4.21),

$$\|\vec{u}_h - \vec{u}_I\|_1 + \|p_h - p_I\|_0 \leq C \sup_{(\vec{w}_h, r_h) \in X_0^h \times M^h} \frac{\mathfrak{B}_h((\vec{u}_h - \vec{u}_I, p_h - p_I); (\vec{w}_h, r_h))}{\|\vec{w}_h\|_1 + \|r_h\|_0}. \tag{4.26}$$

Substituting (4.25) into (4.26)

$$\|\vec{u}_h - \vec{u}_I\|_1 + \|p_h - p_I\|_0 \leq C \sup_{(\vec{w}_h, r_h) \in X_0^h \times M^h} \frac{\mathfrak{B}((\vec{u} - \vec{u}_I, p - p_I); (\vec{w}_h, r_h)) + \frac{1}{4}\Upsilon(p_I, r_h)}{\|\vec{w}_h\|_1 + \|r_h\|_0}.$$

Using the continuity of $\mathfrak{B}$,

$$\|\vec{u}_h - \vec{u}_I\|_1 + \|p_h - p_I\|_0 \leq C \left(\|\vec{u} - \vec{u}_I\|_1 + \|p - p_I\|_0 + \sup_{q_h \in M^h, \|q_h\|_0 = 1} \Upsilon(p_I, q_h) \right). \tag{4.27}$$

Looking at the right hand side of (4.27), the only difficulty is to estimate the stabilization term $\Upsilon(p_I, q_h)$ while the other two terms can be estimated by (4.23)–(4.24).

Since $\Upsilon(p, q_h) = 0$ when p is in $H^1(\Omega) \cap C^0(\Omega)$, we have that $\Upsilon(p_I, q_h) = \Upsilon(p_I - p, q_h)$. Then, following the method in [31], using the triangle and Schwarz inequalities,

$$\begin{aligned} \Upsilon(p_I, q_h) &= \Upsilon(p_I - p, q_h) \\ &\leq C\left(\sum_{T\in T_h}\sum_{E\in\mathcal{E}(T)}\frac{|M|}{4h_{T,E}}\int_E |p-p_I|^2\right)^{1/2}\left(\sum_{T\in T_h}\sum_{E\in\mathcal{E}(T)}\frac{|M|}{4h_{T,E}}\int_E |q_h|^2\right)^{1/2}. \end{aligned} \tag{4.28}$$

Since a macroelement is assumed to be equally divided into four elements,

$$\frac{|M|}{4h_{T,E}} = h^{\perp}_{T,E}. \tag{4.29}$$

Thus, from (4.28),

$$\Upsilon(p_I, q_h) \leq C\left(\sum_{T\in T_h}\sum_{E\in\mathcal{E}(T)} h^{\perp}_{T,E}\int_E |p-p_I|^2\right)^{1/2}\left(\sum_{T\in T_h}\sum_{E\in\mathcal{E}(T)} h^{\perp}_{T,E}\int_E |q_h|^2\right)^{1/2}. \tag{4.30}$$

Since q_h is a piecewise constant, $(\sum_{T\in T_h}\sum_{E\in\mathcal{E}(T)} h^{\perp}_{T,E}\int_E |q_h|^2)^{1/2} \leq C\|q\|_0$.

For the first term of the right hand side of (4.30),

$$h^{\perp}_{T,E}\int_E |p-p_I|^2 = h^{\perp}_{T,E}h_{T,E}\int_{\tilde{E}} |p-p_I|^2 \tag{4.31}$$

Where $\tilde{E}$ is an edge of the reference element $\tilde{T} = (0,1)^2$. Now, applying the trace theorem to the right hand side of (4.31) gives,

$$\begin{aligned} h^{\perp}_{T,E}h_{T,E}\int_{\tilde{E}} |p-p_I|^2 &\leq Ch^{\perp}_{T,E}h_{T,E}\|p-p_I\|^2_{1,\tilde{T}} \\ &\leq Ch^{\perp}_{T,E}h_{T,E}\left(\int_{\tilde{T}}(p-p_I)^2 + \int_{\tilde{T}}\left(\frac{\partial(p-p_I)}{\partial\tilde{x}}\right)^2 + \int_{\tilde{T}}\left(\frac{\partial(p-p_I)}{\partial\tilde{y}}\right)^2\right) \\ &\leq Ch^{\perp}_{T,E}h_{T,E}\left(\frac{1}{|T|}\|p-p_I\|^2_{0,T} + \frac{1}{|T|}h^2_{T,x}\|p_x\|^2_{0,T} + \frac{1}{|T|}h^2_{T,y}\|p_y\|^2_{0,T}\right) \\ &\leq C\left(\|p-p_I\|^2_{0,T} + h^2_{T,x}\|p_x\|^2_{0,T} + h^2_{T,y}\|p_y\|^2_{0,T}\right). \end{aligned}$$

Using (4.24), we can estimate the jump stabilization term as,

$$\Upsilon(p_I, q_h) \leq C\left(\sum_{T\in T_h}(h_{T,x}\|p_x\|_{0,K} + h_{T,y}\|p_y\|_{0,T})\right)\|q_h\|_0. \tag{4.32}$$

Then, combining (4.23), (4.24), (4.27) and (4.32) gives,

$$\begin{aligned} \|\vec{u}_h - \vec{u}_I\|_1 + \|p_h - p_I\|_0 \leq\ & C \sum_{T\in T_h} \Big\{ h_{T,x}\|\vec{u}_{xx}\|_{0,T} + \max(h_{T,x}, h_{T,y})\|\vec{u}_{xy}\|_{0,T} \\ & + h_{T,y}\|\vec{u}_{yy}\|_{0,T} + h_{T,x}\|p_x\|_{0,T} + h_{T,y}\|p_y\|_{0,T} \Big\}, \qquad (4.33) \end{aligned}$$

Adding $\|\vec{u} - \vec{u}_I\|_1 + \|p - p_I\|_0$ to both sides of (4.33) and using (4.23)–(4.24), we have proved Theorem 4.3.5. □

4.3.3 Numerical results

From Theorem 4.3.5, in order to reduce the errors of the stabilized $Q_1 - P_0$ approximation, rectangles on which the exact solution changes rapidly need to be refined toward a proper direction. Let T_h' be the mesh locally refined from T_h. We require that there exists a unique macroelement partitioning T_M' associated with T_h', and T_h' is T_M' uniform.

For this purpose, we suggest the three local refinement strategies shown in Figure 4.7 to refine macroelements rather than elements. If the exact solution changes rapidly in the x direction, the local refinement method 1 is recommended; if it changes rapidly in the y direction, method 2 should be used; if the solution changes rapidly in both of the x and y directions, refinement method 3 is the right choice. In addition, after these local refinements, hanging nodes may exist on the boundaries of some macroelements. Algorithm 4.1 is advocated to remove the hanging nodes.

Algorithm 4.1

```
while there is some hanging nodes in $T_h'$ do
  find the first macroelement with hanging nodes
  if the hanging nodes are on the top and bottom boundaries of the macroelement then
    refine this macroelement using the local refinement method 1
  else
    refine this macroelement using the local refinement method 2
  end if
end while
```

Two test problems with exact solutions on the square domain $\Omega = (-1, 1)^2$ are considered next. For these two test problems, we first solve them with the initial uniform mesh which equally divides the domain into 8×8 elements. Then, we locally refine the

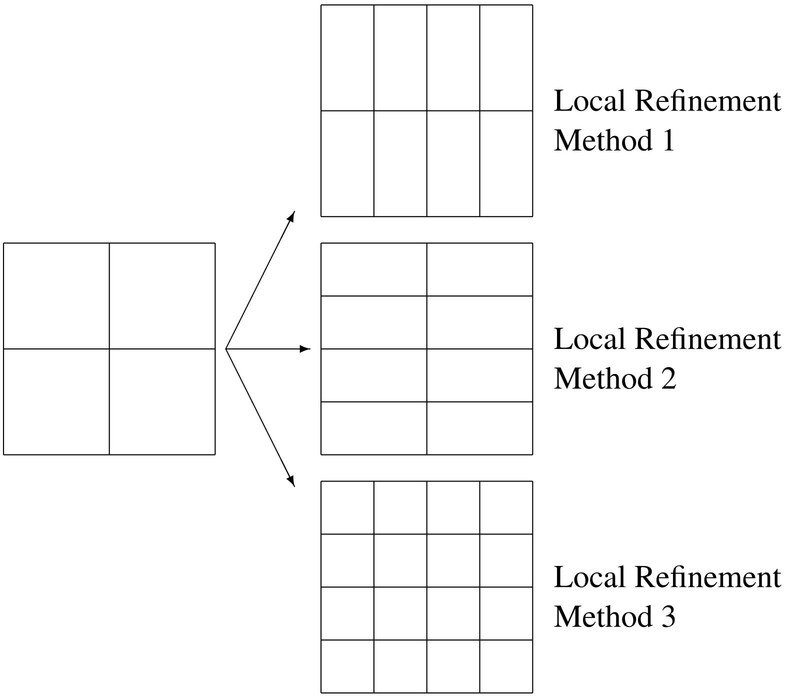

Figure 4.7: Local refinements for a macroelement.

macroelements which contain the elements whose contribution to $||\vec{u} - \vec{u}_h||_1^2 + ||p - p_h||^2$ exceeds 50% of the largest element contribution. After that, we remove all the hanging nodes using Algorithm 4.1.

For comparison, a nonconforming finite element method (the so-called rotated $\boldsymbol{Q}_1 - \boldsymbol{P}_0$ approximation) introduced by Rannacher and Turek [38] is also tested in this section. Turek [44, p.113] states that this rotated $\boldsymbol{Q}_1 - \boldsymbol{P}_0$ approximation is stable for anisotropic meshes. The velocity space of the rotated $\boldsymbol{Q}_1 - \boldsymbol{P}_0$ approximation on each rectangular element is locally defined by span$\{1, x, y, x^2 - y^2\}$ while that of the standard $\boldsymbol{Q}_1 - \boldsymbol{P}_0$ approximation is span$\{1, x, y, xy\}$. The pressure spaces of the rotated and standard $\boldsymbol{Q}_1 - \boldsymbol{P}_0$ approximations are the same—the set of piecewise constant functions. Figure 4.8 shows the degrees of freedom of the rotated and standard $\boldsymbol{Q}_1 - \boldsymbol{P}_0$ approximations.

The following notation is used in the subsequent tables. First, for the stabilized $\boldsymbol{Q}_1 - \boldsymbol{P}_0$ approximation,

$$\epsilon_u^a = ||\vec{u} - \vec{u}_h||_1, \quad \epsilon_p^a = ||p - p_h||_0, \quad \epsilon_{u+p}^a = \left[(\epsilon_u^a)^2 + \left(\epsilon_p^a\right)^2 \right]^{1/2}.$$

Figure 4.8: The left and right pictures are the degrees of freedom for the rotated and the standard $Q_1 - P_0$ approximations respectively (• is a velocity node, while ◦ is a pressure node).

Second, for the rotated $Q_1 - P_0$ approximation,

$$\epsilon_u^b = \left(\sum_{T \in T_h} \|\vec{u} - \vec{u_h}\|_{1,T}^2 \right)^{1/2}, \quad \epsilon_p^b = \|p - p_h\|_0, \quad \epsilon_{u+p}^b = \left[\left(\epsilon_u^b\right)^2 + \left(\epsilon_p^b\right)^2 \right]^{1/2}.$$

We let L denote the level of local refinement and N denote the number of elements. Note that only the errors of the stabilized $Q_1 - P_0$ approximation are used to determine the local refinement sequence. Finally, $\{T_h\}$ is the sequence of meshes locally refined from the initial uniform mesh and $\{Tn_h\}$ is the mesh sequence after a single uniform refinement of T_h (equally dividing each rectangle in $\{T_h\}$ into four).

Test problem 4.3.6 Square domain $(-1, 1)^2$, with the exact solution $\vec{u} = (u, v)$:

$$u = e^{3y} - 1, \quad v = x^2, \quad p = x + y. \tag{4.34}$$

From (4.34), the velocity solution u changes rapidly in the y direction. Thus, we use the local refinement method 2 shown in Fig. 4.7. Fig. 4.9 shows the mesh with local refinement level three associated with this problem. Table 4.7 shows the errors on each local refinement level. From Table 4.7, the total error on the local refinement level three is less than a quarter of the initial mesh and the number of elements is around twice that of the initial mesh. However, from the first row in Table 4.8, the number of elements of the global refinement is four times that of the initial mesh but the errors only reduce by a factor of two (as expected for the standard and rotated $Q_1 - P_0$ approximations). So, the local mesh refinement is efficient in this case. After several steps of local refinement, the errors could become equally distributed in the domain. Then, the global mesh refinement may be necessary for making future progress.

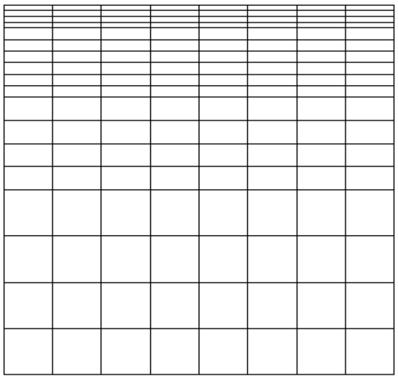

Figure 4.9: Mesh corresponding to local refinement level three for test problem 4.3.6.

Table 4.7: Errors for test problem 4.3.6 with the mesh sequence $\{T_h\}$.

L	ρ	N	ϵ_u^a	ϵ_p^a	ϵ_{u+p}^a	ϵ_u^b	ϵ_p^b	ϵ_{u+p}^b
0	1	64	7.3586	0.2483	7.3628	5.7444	1.5070	5.9388
1	2	80	4.0126	0.2361	4.0195	2.6952	1.3780	3.0270
2	4	96	2.8220	0.2347	2.8318	1.9351	0.7211	2.0651
3	8	144	1.6893	0.2203	1.7036	1.0526	0.3922	1.1233
4	8	176	1.3371	0.2185	1.3549	0.8384	0.3132	0.8949
5	16	224	1.0828	0.2046	1.1019	0.6798	0.2418	0.7215

Table 4.8: Errors for test problem 4.3.6 with the mesh sequence $\{Tn_h\}$.

L	ρ	N	ϵ_u^a	ϵ_p^a	ϵ_{u+p}^a	ϵ_u^b	ϵ_p^b	ϵ_{u+p}^b
0	1	256	3.7460	0.1207	3.7480	2.9576	0.5768	3.0133
1	2	320	2.0200	0.1148	2.0232	1.3637	0.4899	1.4491
2	4	384	1.4221	0.1141	1.4267	0.9782	0.2399	1.0072
3	8	576	0.8466	0.1071	0.8534	0.5277	0.1352	0.5447
4	8	704	0.6699	0.1062	0.6782	0.4205	0.1183	0.4368
5	16	896	0.5418	0.0995	0.5508	0.3399	0.0984	0.3538

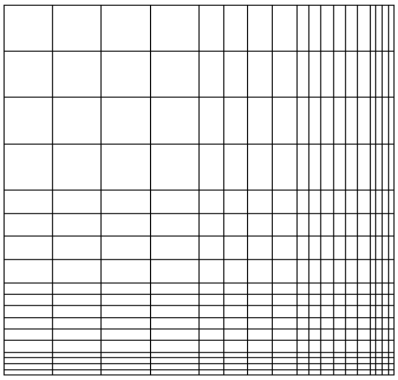

Figure 4.10: Mesh corresponding to local refinement level three for test problem 4.3.7.

Table 4.9: Errors for test problem 4.3.7 with the mesh sequence $\{T_h\}$.

L	ρ	N	ϵ_u^a	ϵ_p^a	ϵ_{u+p}^a	ϵ_u^b	ϵ_p^b	ϵ_{u+p}^b
0	1	64	87.5443	8.2768	87.9347	119.4243	4.6338	119.5142
1	2	100	46.8160	3.2450	46.9283	65.6795	3.2776	65.7612
2	4	144	32.8474	2.8202	32.9682	46.7072	4.3049	46.9052
3	8	324	19.3173	0.7809	19.3330	27.4502	2.2982	27.5463
4	16	484	16.0048	0.7708	16.0234	22.8881	2.8770	23.0683
5	32	1156	10.9346	0.6253	10.9525	15.8307	3.3058	16.1722

Test problem 4.3.7 Square domain $(-1,1)^2$, with the exact solution $\vec{u} = (u, v)$:

$$u = e^{3(x-y)}, \quad v = e^{3(x-y)}, \quad p = x^2 + y^2 - 2/3. \tag{4.35}$$

From (4.35), $\vec{u}$ is rapidly varying in the elements close to the corner $(1,-1)$ (the right bottom corner of Ω), and in these elements, $\vec{u}$ varies rapidly in both the x and the y directions. Thus, the local refinement method 3 is used to refine the macroelements containing elements with large errors. Fig. 4.10 shows the mesh of the local refinement level three. The errors for this example are shown in Table 4.9 and 4.10. From these two tables, it still can be seen that the anisotropic meshes generated from local refinement are more efficient than the uniform meshes.

From these tables, it can also be seen that the errors of the stabilized and rotated $Q_1 - P_0$ approximations are similar for both test problems.

Table 4.10: Errors for test problem 4.3.7 with the mesh sequence $\{Tn_h\}$.

L	ρ	N	ϵ_u^a	ϵ_p^a	ϵ_{u+p}^a	ϵ_u^b	ϵ_p^b	ϵ_{u+p}^b
0	1	256	43.7149	2.4200	43.7818	61.2259	1.2490	61.2386
1	2	400	23.4113	0.8854	23.4281	33.0695	1.3291	33.0962
2	4	576	16.4365	0.7864	16.4553	23.3371	1.6918	23.3984
3	8	1296	9.6621	0.2279	9.6648	13.6943	0.7923	13.7172
4	16	1936	8.0056	0.2262	8.0088	11.3683	0.9023	11.4041
5	32	4624	5.4677	0.1963	5.4712	7.7859	0.8308	7.8301

4.4 A Posteriori Error Estimation for Stabilized $Q_1 - P_0$

4.4.1 Existing theories

This section focuses on a posteriori error estimation for the stabilized $Q_1 - P_0$ approximation associated with anisotropic meshes. Since most of the recent papers on a posteriori error estimation only consider isotropic meshes, we start with a review of this literature. After that, the recent relevant papers on a posteriori error estimation for anisotropic meshes will be reviewed. Finally, an anisotropic local problem error estimator will be presented, and numerical examples will show that this estimator is reliable in practice. For simplicity, the forcing term f in (1.1) is assumed to be zero in this section.

The paper [30] by Kay and Silvester provides a residual error estimator and two local problem error estimators for the stabilized $Q_1 - P_0$ approximation (4.6)–(4.7). The residual error estimator is:

$$\eta_{R,T}^2 = \|\nabla \cdot \vec{u}_h\|_{0,T}^2 + \sum_{E \in \mathcal{E}(T)} h_{T,E} \|\vec{R}_E\|_{0,E}^2, \tag{4.36}$$

where the stress jump $\vec{R}_E$ is defined in Section 3.3.1.

The other two estimators are based on solving local Neumann problems. The first one is to solve a local Stokes problem: find $(e_{S,T}, \epsilon_{S,T}) \in \mathbf{Q}_T \times P_1(T)$, such that

$$(\nabla e_{S,T}, \nabla \vec{v})_T - (\epsilon_{S,T}, \nabla \cdot \vec{v})_T = - \sum_{E \in \mathcal{E}(T)} \langle \vec{R}_E, \vec{v} \rangle_E \quad \forall \vec{v} \in \mathbf{Q}_T, \tag{4.37}$$

$$(\nabla \cdot e_{S,T}, q)_T = (\nabla \cdot \vec{u}_h, q) \quad \forall q \in P_1(T), \tag{4.38}$$

where $\mathbf{Q}_T$ is the space $Q_2(T)^2$ with the four vertex nodes removed. Then the local Stokes problem estimator is:

$$\eta_{S,T}^2 = |e_{S,T}|_{1,T}^2 + \|\epsilon_{S,T}\|_{0,T}^2. \tag{4.39}$$

The second one is the local Poisson problem estimator:

$$\eta_{P,T}^2 = |e_{P,T}|_{1,T}^2 + \|\epsilon_{P,T}\|_{0,T}^2, \tag{4.40}$$

where $(e_{P,T}, \epsilon_{P,T}) \in \mathbf{Q}_T \times \boldsymbol{P}_1(T)$ satisfies

$$(\nabla e_{P,T}, \nabla \vec{v})_T = -\sum_{E\in\mathcal{E}(T)} \langle \vec{R}_E, \vec{v}\rangle \quad \forall \vec{v} \in \mathbf{Q}_T, \tag{4.41}$$

$$(\epsilon_{P,T}, q) = (\nabla \cdot \vec{u}_h, q)_T \quad \forall q \in \boldsymbol{P}_1(T). \tag{4.42}$$

As discussed in Chapters 2 and 3, to be efficient and reliable, an error estimator η_T needs to satisfy the following two inequalities,

$$\left(\sum_{T\in T_h} \|\vec{u} - \vec{u}_h\|_{1,T}^2\right)^{1/2} + \|p - p_h\|_0 \le C_{up} \sqrt{\sum_{T\in T_h} \eta_T^2}, \tag{4.43}$$

$$C_{low}\eta_T \le \left(\sum_{T\in\omega_T} \|\vec{u} - \vec{u}_h\|_{1,T}^2\right)^{1/2} + \|p - p_h\|_{\omega_T}, \tag{4.44}$$

where the local patch ω_T is defined in Section 1.4.1.

In [30], the upper bound (4.43) and the local lower bound (4.44) for the residual estimator $\eta_{R,T}$ are firstly established with constants C_{up} and C_{low} related to the aspect ratio ρ and the continuous inf-sup constant γ (see Definition 1.3.1). Then, the Stokes estimator $\eta_{S,T}$ and Poisson estimator $\eta_{P,T}$ are shown to be equivalent to $\eta_{R,T}$. However, from numerical examples, we see that $\eta_{S,T}$ and $\eta_{P,T}$ can estimate the exact error much more accurately than $\eta_{R,T}$. In addition, $\eta_{P,T}$ is computationally cheaper than $\eta_{S,T}$. So, $\eta_{P,T}$ is the best of the three estimators for stabilized $\boldsymbol{Q}_1 - \boldsymbol{P}_0$ approximation.

From the original paper introducing the local Neumann problem estimator by Bank and Weiser [6], the theoretical basis is on a so-called saturation assumption.

Definition 4.4.1 *Saturation assumption: let function spaces X_h, W_h and X have the relationship: $X_h \subset W_h \subset X$. The space W_h satisfies the saturation assumption with respect to X and X_h if there exists a constant* $0 \le \mu < 1$ *such that:*

$$\min_{\psi_h\in W_h} \|\nabla(v - \psi_h)\|_0 \le \mu \min_{\phi_h\in X_h} \|\nabla(v - \phi_h)\|_0 \quad \forall v \in X. \tag{4.45}$$

Note that, the larger space W_h can be constructed by introducing higher order basis functions to X_h or refining the mesh. In other words, there are two versions of the saturation assumption: one requires that the higher order method is more accurate than the lower order method, and the other requires that a given approximation method is more accurate on a finer mesh than on a coarse mesh. Both these versions of the saturation assumption are true when the exact solution is smooth enough. For example, when the exact solution is in $\boldsymbol{H}^3 \times H^2(\Omega)$, the $\boldsymbol{Q}_2 - \boldsymbol{Q}_1$ approximation is more accurate than $\boldsymbol{Q}_1 - \boldsymbol{P}_0$. Also, for the stabilized $\boldsymbol{Q}_1 - \boldsymbol{P}_0$ approximation, due to Theorem 4.3.5, a finer mesh is more accurate when the solution is in $\boldsymbol{H}^2 \times H^1(\Omega)$. However, since the exact solution is not always in $\boldsymbol{H}^2 \times H^1(\Omega)$, then the saturation assumption may fail.

From the discussion above, it can be seen that the saturation assumption is not always satisfied. Then, the error estimators based on it may not be reliable. Nochetto [36] suggests that in order to avoid the saturation assumption, the local Neumann problem estimators should be derived by proving its equivalence to the residual estimators and this is the way later works followed (e.g. [30]).

In summary, from the literature, the upper and local lower bounds of local problem error estimators can be established by either using the saturation assumption or by showing their equivalence to the underling residual estimators.

For the Stokes problem posed on stretched meshes, Randrianarivony [37] provides a hierachical based estimator which needs the saturation assumption, while Creusé et al [17] provide a residual error estimator.

The analysis in [37] is based on the saturation assumption. More precisely, the constant C_{up} in the upper bound in (4.43) is related to the saturation assumption constant μ in (4.45), and $C_{up} = O(\frac{1}{1-\mu})$. As we have discussed before, the saturation assumption constant μ might be close or equal to unity, and then the upper bound is not reliable. In addition, there is simply a global lower bound but no local lower bound in [37]. Because of this, the estimator may not be able to identify the right elements for subsequent refinement.

The residual estimator in [17] is:

$$\eta_{C,T}^2 = ||\nabla \cdot \vec{u}_h||_T^2 + \sum_{E \in \mathcal{E}(T)} \frac{h_{T,min}^2}{h_{T,E}^{\perp}} ||\vec{R}_E||_E^2. \tag{4.46}$$

From [17], the constant C_{up} for this estimator is dependent on the global grading factor κ and $C_{up} \sim (m_1(\vec{e}, T_h) + m_1(\vec{v}_p, T_h))$, where $\vec{e} = \vec{u} - \vec{u}_h$ and m_1 is the alignment measure defined as follows.

Definition 4.4.2 *Alignment measure: let $\vec{v} \in \boldsymbol{H}^1$,*

$$m_1(\vec{v}) := \frac{\sum_{T \in T_h} h_{T,min}^{-1} (h_{T,x} \| \frac{\partial \vec{v}}{\partial x} \|_{0,T} + h_{T,y} \| \frac{\partial \vec{v}}{\partial y} \|_{0,T})}{\| \frac{\partial \vec{v}}{\partial x} \|_0 + \| \frac{\partial \vec{v}}{\partial y} \|_0} \tag{4.47}$$

The function $\vec{v}_p$ above is in $\boldsymbol{H}^1$, and is designed to satisfy

$$\|e_p\|_0 \le C \frac{\int_\Omega \epsilon \nabla \cdot \vec{v}_p}{|\vec{v}_p|_1}, \tag{4.48}$$

where $\epsilon = p - p_h$ and the generic constant C only depends on the shape of the domain .

For the constant $m_1(\vec{e}, T_h)$, if the mesh is refined properly (e.g. if $\|\partial \vec{e}/\partial x\|_{0,T}$ is large, then $h_{T,x}$ should be small), $m_1(\vec{e}, T_h)$ can be bounded. However, we do not usually have the function $\vec{v}_p$. In this case, the constant $m_1(\vec{v}_p, T_h)$ can not be estimated. So, this estimator may not be able to provide a reliable upper bound for the exact error.

From the discussion above, both of these two estimators may not be mathematically efficient and reliable. This causes difficulty in establishing an efficient and reliable local problem estimator for anisotropic meshes in the sense of analysis. However, from the computational point of view, since the local Poisson problem estimator $\eta_{P,T}$ is effective for isotropic meshes, it is of interest to modify it for anisotropic meshes (see the next part of this section), even though it is an open question to analyze this situation.

4.4.2 An new anisotropic local problem error estimator

From Section 4.4.1, for isotropic meshes, the local Poisson problem estimator for the local jump stabilized $\boldsymbol{Q}_1 - \boldsymbol{P}_0$ approximation is based on solving (4.41)–(4.42). In this section, we consider anisotropic meshes. Since the contribution of (4.42) is quite small from our computational experience, the main issue is then to modify (4.41) for anisotropic meshes.

For isotropic meshes the two contributions to the left hand side of (4.41) are equally weighted. However, for anisotropic meshes, they should have different weights. For this purpose, an anisotropic local Poisson estimator is defined as follows,

$$\eta^{*2}_{P,T} = |e^*_T|^2_{1,T} + \|\epsilon^*_T\|^2_{0,T}, \tag{4.49}$$

where $e^*_T = (e^*_{T,1}, e^*_{T,2}) \in \mathbf{Q}_T$ and $\epsilon^*_T \in P_1(T)$ satisfy

$$\begin{aligned} \frac{h_{T,x}}{h_{T,y}}\left(\frac{\partial e^*_{T,1}}{\partial x}, \frac{\partial v_1}{\partial x}\right)_T &+ \frac{h_{T,y}}{h_{T,x}}\left(\frac{\partial e^*_{T,1}}{\partial y}, \frac{\partial v_1}{\partial y}\right)_T + \frac{h_{T,x}}{h_{T,y}}\left(\frac{\partial e^*_{T,2}}{\partial x}, \frac{\partial v_2}{\partial x}\right)_T + \frac{h_{T,y}}{h_{T,x}}\left(\frac{\partial e^*_{T,2}}{\partial y}, \frac{\partial v_2}{\partial y}\right)_T \\ &= \sum_{E \in \mathcal{E}(T)} \left\langle \vec{R}_E, \vec{v} \right\rangle \quad \forall \vec{v} = (v_1, v_2) \in \mathbf{Q}_T, & (4.50) \\ (\epsilon^*_T, q) &= (\nabla \cdot \vec{u}_h, q)_T \qquad \forall q \in P_1(T). & (4.51) \end{aligned}$$

The following test problem will provide an illustration.

Test problem 4.4.3 Square domain $(0,1)^2$, with the exact solution (this is a test problem in the MATLAB package IFISS [20]):

$$u = 20xy^3, \quad v = 5x^4 - 5y^4, \quad p = 60x^2y - 20y^3. \tag{4.52}$$

For this test problem, the computational domain is partitioned by a Shishkin mesh, which in this case is the tensor product of the following one-dimensional grids

$$x_i = \frac{i}{4}\tau \quad i = 0:3, \tag{4.53}$$

$$x_{i+4} = \tau + \frac{i}{4}(1-\tau) \quad i = 1:4, \tag{4.54}$$

where $\tau \geq 1$. Note that as the parameter τ increases, the global aspect ratio of the Shishkin mesh increases quite rapidly.

Table 4.11 shows the ratio between the exact and estimated errors with the following notation

$$\begin{aligned} \eta &= \sqrt{\eta_T^2}, \\ \eta^* &= \sqrt{\eta_T^{*\,2}}, \\ e_{u+p} &= \|\nabla(\vec{u} - \vec{u}_h)\|_0 + \|p - p_h\|_0. \end{aligned}$$

From Table 4.11, it can be seen that the anisotropic estimator η^* provides an efficient upper bound for the exact error, since e_{u+p}/η^* is essentially constant, independent of the aspect ratio. However, the original estimator η is dependent on ρ.

Table 4.11: Error estimators for test problem 4.4.3.

τ	ρ	$\frac{e_{u+p}}{\eta}$	$\frac{e_{u+p}}{\eta^*}$
1	9	2.4765	2.8598
2	99	1.5006	2.9384
3	999	0.5349	2.9469
4	9999	0.1172	2.9470

4.5 Conclusion

In this chapter, we first reviewed the literature on the stability of inf-sup stable methods for anisotropic meshes. Summarizing these papers and our numerical examples, the following conclusions can be made,

- $\boldsymbol{Q}_2 - \boldsymbol{P}_0$ is stable for mesh families containing edge patches but unstable for families including corner patches;
- $\boldsymbol{Q}_2 - \boldsymbol{Q}_1$ may be stable for edge patches but unstable for corner patches;
- $\boldsymbol{Q}_2 - \boldsymbol{P}_{-1}$ is unstable for edge and corner patches.

Due to the degeneration of the inf-sup constants, all the inf-sup stable methods may have large error for meshes including corner patches.

Since the inf-sup stable methods may not be accurate for corner patches, we established a robust a priori estimation in the form of Theorem 4.3.5 for the local jump stabilized $\boldsymbol{Q}_1 - \boldsymbol{P}_0$ approximation. In this theorem, there is only a local uniformity requirement for meshes: all the rectangles in a macroelement must have the same size. After that, test problems show that, using anisotropic meshes can lead to more accurate solutions and less computational cost compared to uniform meshes.

Finally, a posteriori error estimation of mixed approximations for anisotropic meshes is discussed. It is still an open question to establish a completely efficient and reliable error estimation strategy of mixed approximations for anisotropic meshes. However, from numerical experiments, our anisotropic local Poisson problem estimator can provide an efficient upper bound independently of the global mesh aspect ratio for the stabilized $\boldsymbol{Q}_1 - \boldsymbol{P}_0$ approximation.

Chapter 5

Solving Unsteady Flow Problems Using the Stabilized $Q_1 - P_0$ Approximation

5.1 Introduction

5.1.1 The Navier-Stokes equations

The Navier-Stokes equations considered in this chapter are,

$$\frac{\partial \vec{u}}{\partial t} - \nu \nabla^2 \vec{u} + \vec{u} \cdot \nabla \vec{u} + \nabla p = 0 \quad \text{in} \quad \Omega, \tag{5.1}$$

$$\nabla \cdot \vec{u} = 0 \quad \text{in} \quad \Omega, \tag{5.2}$$

$$\vec{u} = \vec{g} \quad \text{on} \quad \partial\Omega_D, \tag{5.3}$$

$$\frac{\partial \vec{u}}{\partial n} - \vec{n} p = \vec{0} \quad \text{on} \quad \partial\Omega_N, \tag{5.4}$$

$$\vec{u}(0, \vec{x}) = 0 \quad \text{in} \quad \Omega, \tag{5.5}$$

where $\nu > 0$ is the fluid viscosity parameter (ν is assumed to be small—$O(10^{-2})$, since we focus on unsteady flow problems in this chapter) and the boundary data $\vec{g}$ in (5.3) is time dependent.

Note that we consider the equations (5.1)–(5.5) to be dimensionless—ν in (5.1) is used as a dimensionless number in place of the Reynolds number: $Re = \tilde{U}\tilde{L}/\nu$. This is due to our definitions of $\tilde{U}$ and $\tilde{L}$ below. In this chapter, we focus on two test problems which are described in Section 5.2 and Section 5.3. The reference velocity scale $\tilde{U}$ is defined by the maximum inlet horizontal velocity as time $t \to \infty$ (that is $\tilde{U} = 1$ for both test problems). The length scale for test problem 1 is defined to be half the full channel height: $\tilde{L} := H/2 = 1$ (see Section 5.2), while the length scale for test problem 2 is defined to be twice the cylinder edge length: $\tilde{L} := 2B = 1$ (see Section 5.3). So, with the definitions of $\tilde{U}$ and $\tilde{L}$, $Re^{-1} = \nu$ for both test problems.

The aim of this chapter is to show how to solve (5.1)–(5.5) efficiently. For any potential numerical scheme, there are three important issues: the spatial discretization, the temporal discretization and the linearization of the quadratic term $\vec{u} \cdot \nabla\vec{u}$ in (5.1). In this chapter, the stabilized adaptive TR (Trapezoid Rule) time stepping method introduced by Kay et al. [29] is adopted for the time discretization. For the linearization, the extrapolated method discussed in [29] is used. Note that for the spatial discretization, only inf-sup stable methods are considered in [29]. Thus, it is of interest to extend the methodology in [29] to the stabilized $\boldsymbol{Q}_1 - \boldsymbol{P}_0$ method.

The motivation for using the stabilized $\boldsymbol{Q}_1 - \boldsymbol{P}_0$ method is discussed in Section 4.3. First, higher order methods do not provide more accurate solutions when the exact solution is not smooth enough (this is often the case, e.g. the problem of flow in a step domain will be introduced in the next section). Second, in Chapter 4, the a priori error bound of the stabilized approximation is established for anisotropic meshes (only for steady-state Stokes problems), but standard inf-sup stable approximations may not be so robust.

For inf-sup stable methods, on each time step, the following fully discretized problem needs to be solved: we seek $(\vec{d}^{n+1}, p_{n+1}) \in X^h_{Et} \times M^h$, where $n+1$ means the time is t_{n+1} and X^h_{Et} is a finite dimensional approximation of the velocity space with boundary data $\frac{\vec{g}^{n+1}-\vec{g}^{n}}{k_{n+1}}$ ($k_{n+1} = t_{n+1} - t_n$ is the current time step), such that

$$\begin{aligned} 2(\vec{d}^n_h, \vec{v}_h) + \nu k_{n+1}(\nabla\vec{d}^n_h, \vec{v}_h) &+ k_{n+1}(\vec{w}^{n+1}_h \cdot \nabla\vec{d}^n_h, \vec{v}_h) - (p^{n+1}_h, \nabla \cdot \vec{v}_h) \\ &= (\frac{\partial\vec{u}^n_h}{\partial t}, \vec{v}_h) - \nu(\nabla\vec{u}^n_h, \nabla\vec{v}_h) - (\vec{w}^{n+1}_h \cdot \nabla\vec{u}^n_h, \vec{v}_h), \qquad (5.6) \\ (\nabla \cdot \vec{d}^{n+1}_h, q_h) &= 0, \qquad (5.7) \end{aligned}$$

for all $(\vec{v}_h, q_h) \in X^h_0 \times M^h$, where $\vec{w}^{n+1}_h = (1 + \frac{k_{n+1}}{k_n})\vec{u}^n_h - (\frac{k_{n+1}}{k_n})\vec{u}^{n-1}_h$. The velocity at t_{n+1} can then be updated by,

$$\vec{u}^{n+1}_h = \vec{u}^n_h + k_{n+1}\vec{d}^n_h; \qquad \frac{\partial\vec{u}^{n+1}_h}{\partial t} = 2\vec{d}^n_h - \frac{\partial\vec{u}^n_h}{\partial t}. \qquad (5.8)$$

As introduced in [29], in order to start (5.6)–(5.7), a potential flow problem is solved to obtain the initial acceleration at the first time step: find $(\frac{\partial\vec{u}^0}{\partial t}, p_0) \in X_{Et}^h \times M^h$ such that,

$$\Big(\frac{\partial \vec{u}_h^0}{\partial t}, \vec{v}_h\Big) - (p_h^0, \nabla\cdot\vec{v}_h) = -\nu(\nabla\vec{u}_h^0, \nabla v_h) - (\vec{u}_h^0\cdot\nabla\vec{u}_h^0, \vec{v}_h) \quad \forall\vec{v}_h \in X_0^h, \tag{5.9}$$

$$\Big(\nabla\cdot\frac{\partial\vec{u}^0}{\partial t}, q_h\Big) = 0 \quad \forall q_h \in M^h. \tag{5.10}$$

Alternatively, for the stabilized $Q_1 - P_0$ method, on a general TR step, the following problem needs to be solved,

$$\begin{aligned}
2(\vec{d}_h^n, \vec{v}_h) + \nu k_{n+1}(\nabla\vec{d}_h^n, \vec{v}_h) &+ k_{n+1}(\vec{w}_h^{n+1}\cdot\nabla\vec{d}_h^n, \vec{v}_h) - (p_h^{n+1}, \nabla\cdot\vec{v}_h) \\
&= \Big(\frac{\partial\vec{u}_h^n}{\partial t}, \vec{v}_h\Big) - \nu(\nabla\vec{u}_h^n, \nabla\vec{v}_h) - (\vec{w}_h^{n+1}\cdot\nabla\vec{u}_h^n, \vec{v}_h), \qquad (5.11)\\
-(\nabla\cdot\vec{d}_h^{n+1}, q_h) &- \beta\Upsilon(p_h^{n+1}, q_h) = 0, \qquad (5.12)
\end{aligned}$$

for all $(\vec{v}^h, q_h) \in X_0 \times M^h$, where β is the stabilization parameter and the stabilization term $\Upsilon(p_h, q_h)$ has been introduced in Section 4.3 and [21, p.259], that is

$$\begin{aligned}
\Upsilon_M(p_h, q_h) &:= \frac{|M|}{4}\sum_{E\in\Gamma_M}\frac{1}{h_E}\int_E [\![p_h]\!]_E[\![q_h]\!]_E, \qquad (5.13)\\
\Upsilon(p_h, q_h) &:= \sum_{M\in T_M}\Upsilon_M(p_h, q_h). \qquad (5.14)
\end{aligned}$$

For the initial step, the stabilized method is to find $(\frac{\partial\vec{u}^0}{\partial t}, p_0) \in X_{Et}^h \times M^h$, such that,

$$\Big(\frac{\partial \vec{u}^0}{\partial t}, \vec{v}_h\Big) - (p_h^0, \nabla\cdot\vec{v}_h) = -\nu(\nabla\vec{u}_h^0, \nabla v_h) - (\vec{u}_h^0\cdot\nabla\vec{u}_h^0, \vec{v}_h) \quad \forall\vec{v}_h \in X_0^h, \tag{5.15}$$

$$-\Big(\nabla\cdot\frac{\partial\vec{u}^0}{\partial t}, q_h\Big) - \beta\Upsilon(p_h^0, q_h) = 0 \quad \forall q_h \in M^h. \tag{5.16}$$

Remark 5.1.1 The stabilization at the initial step in (5.16) is not mathematically necessary, since the system (5.15)–(5.16) is solvable with $\beta = 0$. However, from computational experiments, including this stabilization can make the time steps increase more quickly at earlier steps—certainly for time shorter than the initial response time that is referred to in [29].

5.1.2 Time stepping parameters

The parameters of the stabilized adaptive TR time stepping method (see [29]) used in this chapter are:

- initial time step = 10^{-9};
- time stepping tolerance = 10^{-4};
- averaging frequency parameter $n_\star = 10$.

Note that the initial time step is quite small ($k_0 = 10^{-9}$). Although our computational experience never shows any trouble for these small time steps, the stability of stabilized approximations with respect to time integration is always an important issue when the time steps are very small. A number of recent articles discuss this issue for transient Stokes problems, and they typically reach a conclusion that the time steps associated with stabilized methods can not be much smaller than the mesh size. From example, Bochev et al. [11] show that, for the backward-Euler time stepping method, residual based stabilized methods are stable only when $\Delta t > Ch^2$. Subsequently, a more detailed study by Burman and Fernández [13] proves that the pressure stabilized methods (including our local jump stabilized method) is unconditionally stable for the TR time stepping method only when the initial data is regular enough. However, the paper [13] still only focuses on the Stokes problem. So, although the initial condition (5.5) is zero and it then satisfies the requirement in [13], the stability analysis of the stabilized system (5.11)–(5.12) for very small time steps remains an open question.

5.1.3 Stabilization parameters

In order to check the performance of the spatial stabilized method (5.11)–(5.12), the following four different finite element methods are tested,

- An inf-sup stable method: the $\boldsymbol{Q}_2 - \boldsymbol{P}_{-1}$ approximation (black);
- The stabilized $\boldsymbol{Q}_1 - \boldsymbol{P}_0$ approximation with a stabilization parameter $\beta = \frac{1}{4}\nu$ (blue);
- The stabilized $\boldsymbol{Q}_1 - \boldsymbol{P}_0$ approximation with $\beta = \frac{1}{4}$ (red);
- The stabilized $\boldsymbol{Q}_1 - \boldsymbol{P}_0$ approximation with $\beta = \frac{1}{4\nu}$ (green),

where the colors in the brackets will be used to illuminate the corresponding methods in the subsequent figures. From Silvester [42], the main idea of the local jump stabilized $\boldsymbol{Q}_1 - \boldsymbol{P}_0$

method is trying to make the pressure approximation constant on each macroelement, so that the checkerboard pressure mode is controlled. The larger the parameter value β is, the closer to a constant on each macroelement the pressure approximation becomes. For this purpose, we test these three choices: small $\beta = \frac{1}{4}\nu$ (since ν is assumed to be small), medium $\beta = \frac{1}{4}$ and large $\beta = \frac{1}{4\nu}$. We want to clarify that the three stabilization parameters are dimensionless, since throughout this chapter, the problem (5.1)–(5.5) is considered to be dimensionless and $\nu = Re^{-1}$ is also dimensionless.

The main objective of this chapter is to find appropriate parameters for the transient Navier-Stokes problem solved with the adaptive TR time stepping method. Note that, the $\boldsymbol{Q}_2 - \boldsymbol{P}_{-1}$ method is referred to have the "true" solution and the stabilized solutions are compared with this reference solution.

In addition, time steps are not involved in the definition of the stabilization parameter. This is a consequence of our approach to stabilization—that is to control the checkerboard pressure mode. Thus, the time step size plays no role, which is quite different from the residual based stabilization methods (see [11]).

In the next sections, two numerical experiments are performed using the MATLAB package IFISS3.0 [43]. In these numerical tests, the viscosity parameters are both $O(10^{-2})$. Very viscous flow problems are not considered here. For very large viscosity cases, Burman et al. [14] showed that the stabilization parameter should be proportional to the local Reynolds number (that is ν^{-1} in this chapter) for stabilized equal order approximations. The same conclusion is reached for the local jump stabilized $\boldsymbol{Q}_1 - \boldsymbol{P}_0$ approximation in [21, p.329].

5.2 Test Problem 1 (Steady Flow): Flow in a Backward Step Domain with Viscosity $\nu = \frac{1}{600}$

5.2.1 Introduction and logistics

The backward step domain is shown in Fig. 5.1. In this figure, O is the origin of the

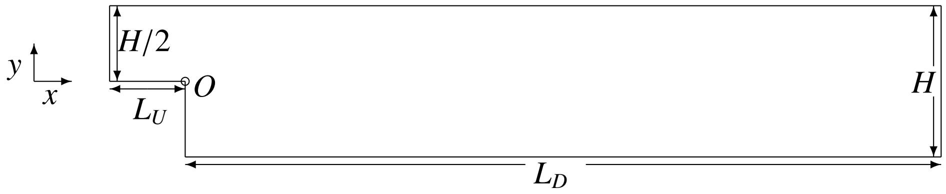

Figure 5.1: The backward step domain.

cartesian coordinate system. Throughout this section, the dimensions of the domain are,

$$H = 2; \quad L_U = 1; \quad L_D = 30.$$

The boundary condition is as follows. A time dependent velocity $\vec{u} = (u, v)$,

$$u = (1 - e^{(-10t)})4y(1 - y), \quad v = 0,$$

is applied on the inflow boundary (the left boundary), (5.4) is applied on the outflow boundary (the right boundary), and the other boundaries are non-slip non-penetration boundaries.

The initial condition is as in (5.5), which implies that the flow is initially at rest.

For the viscosity $\nu = \frac{1}{600}$[1], the flow solution of this test problem is expected to be steady. There are two pieces of evidence supporting this expectation. First, Gresho et al. [25] performed extensive numerical experiments on a closely related problem which is equivalent to our test problem except that its upstream length L_U is set to zero (or in other words, they do not have an inlet channel). Their results show that the solution reaches a steady-state. Second, the effect of the inlet channel is investigated in detail by Barton [9], which shows that for this small viscosity ($\nu = \frac{1}{600}$), the inlet channel has only a small influence on the flow field away from the corner. Thus, the solution of our test problem should have a similar behavior to the solution in [25].

However, the paper [9] also pointed out that for very viscous flow, a long inlet channel could lead to a better agreement between numerical solutions and experimental results. This motivates us to adopt the backward step domain with $L_U = 1$ rather than $L_U = 0$.

Two uniform meshes are tested in this section: one is referred to as the coarse mesh and the other as the fine mesh. For the $Q_2 - P_{-1}$ method, the coarse mesh is a uniform mesh with $h = \frac{1}{8}$ (16145 velocity degrees of freedom), while the coarse mesh for the stabilized

---

[1] This is $Re = 800$ with the normal normalization (see [25]).

$Q_1 - P_0$ method is the uniform mesh with $h = \frac{1}{16}$, since we want to keep the same velocity degrees of freedom. The fine mesh for $Q_2 - P_{-1}$ is the uniform mesh with $h = \frac{1}{16}$, while the fine mesh for $Q_1 - P_0$ is obtained by refining it once (that is, $h = \frac{1}{32}$).

The structure of this section is: first, some pictures of velocity and pressure fields computed by stabilized $Q_1 - P_0$ with $\beta = \frac{1}{4}\nu$ will be plotted. After that, the four different finite element methods will be compared by measuring the following quantities,

- velocity change per time step and global kinetic energy;
- time steps of the adaptive TR method;
- lengths of the upper and lower eddies;
- velocities and pressures at three history points $\mathbf{P}_1 = (0, 0)$, $\mathbf{P}_2 = (10, 0.75)$ and $\mathbf{P}_3 = (28, 0)$;
- vorticity.

The time interval for computing these history values is $[0, 450]$. Note that the simulations in [25] suggest that this time interval is long enough for the solution to reach a steady-state.

5.2.2 The flow field at snap-shot times

The solution fields of this test problem are shown in Fig. 5.2 to Fig. 5.5. These are computed by the stabilized $Q_1 - P_0$ approximation with $\beta = \frac{1}{4}\nu$ on the fine mesh. From Fig. 5.2(a), at an early time ($t \approx 10$), two separation eddies can be seen clearly—one is the upper eddy and other is the lower eddy. In addition, the upper eddy at this time is quite small and close to the inlet channel. As the time value increases, Fig. 5.2(b) and Fig. 5.2(c) show that the main upper eddy moves towards the outflow boundary and the main lower eddy becomes longer. Also, besides the main eddies, some small eddies appear in these last two pictures. However, as the time value t becomes very large (larger than 100), in Fig. 5.3, only the main upper and lower eddies can be seen clearly, and the other small eddies seem to have dissipated. At time $t \approx 100$, the streamlines close to the outflow boundary are not parallel to the $x-$axis. The streamlines become closer to parallel at $t \approx 200$, and they seem to reach a steady-state at $t \approx 450$.

The pressure solution is provided in Fig. 5.4 and Fig. 5.5. These pictures show that the pressure changes rapidly at the beginning and goes to a steady-state at the end of the time interval.

5.2.3 Time steps

Fig. 5.6 shows the time steps of our four approximation methods. It can be seen that, for both of the mesh levels, the time steps of the stabilized $Q_1 - P_0$ method with $\beta = \frac{1}{4}$ and $\beta = \frac{1}{4}\nu$ have a very close agreement with that of the $Q_2 - P_{-1}$ method.

However, for the coarse mesh (see Fig. 5.6(a)), the stabilized $Q_1 - P_0$ method with $\beta = \frac{1}{4\nu}$ has a quite different time step pattern—its time steps close to the end of the time interval are much larger than those of the other methods. Large time steps imply that the flow goes to a steady structure quickly. However, large time steps may also lead to less accurate solutions.

In addition, for the fine mesh (see Fig. 5.6(b)), the time steps of the stabilized method with $\beta = \frac{1}{4\nu}$ are more in line with those of the other methods. In this case, the time steps near to the steady-state are much smaller. For the other three methods, their time steps do not have any obvious difference between the two mesh levels. So, just from the information of the time steps, it might be suspected that the more proper choice of stabilization parameter is $\beta = \frac{1}{4}\nu$ or $\beta = \frac{1}{4}$ rather than $\beta = \frac{1}{4\nu}$.

5.2.4 The velocity change and kinetic energy

In many articles, the criterion for a time dependent solution becoming steady is the relative velocity change between two time steps: $\frac{\|\vec{u}_h^{n+1} - \vec{u}_h^n\|_0}{\|\vec{u}_h^{n+1}\|_0}$ (see Barrenechea and Blasco [8]). When the relative velocity change is small enough, the flow problem is then assumed to be steady. So, it is of interest to see the velocity changes for this test problem (see Fig. 5.7). For the fine mesh, all four methods finally reach a very small relative velocity change (smaller than 10^{-3}). However, for the coarse mesh, the velocity change of the stabilized method

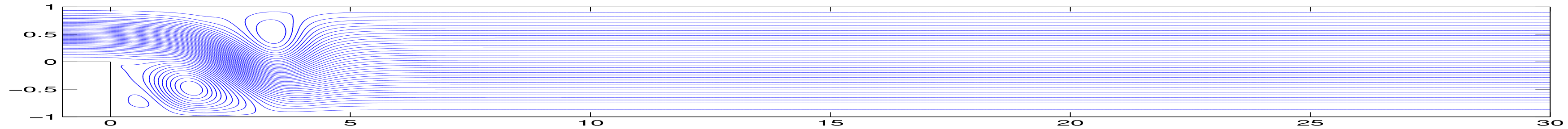

(a) Velocity streamlines at $t = 10.15$

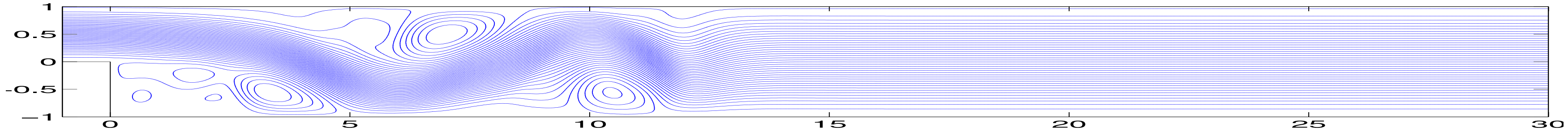

(b) Velocity streamlines at $t = 30.04$

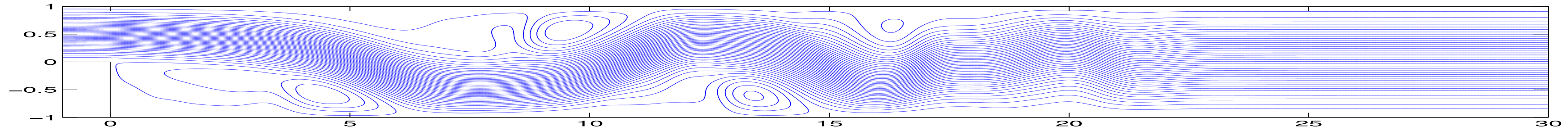

(c) Velocity streamlines at $t = 50.03$

Figure 5.2: Velocity streamlines generalized by stabilized $\boldsymbol{Q}_1 - \boldsymbol{P}_0$ with $\beta = \frac{1}{4}\nu$ (early time).

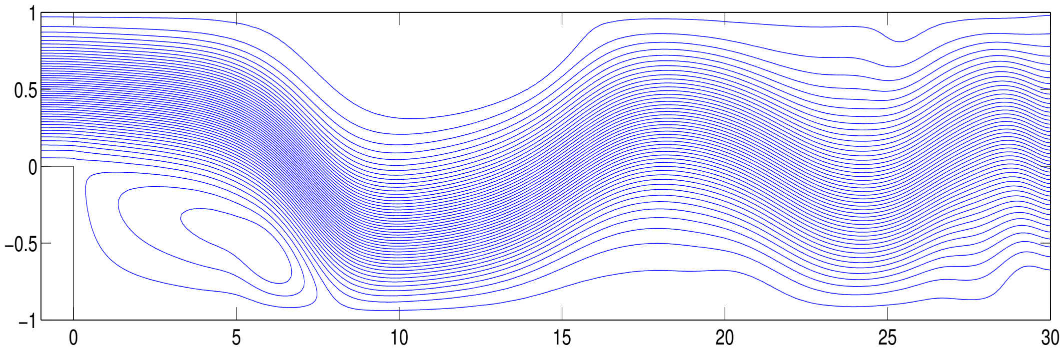

(a) Velocity streamlines at $t = 100.20$

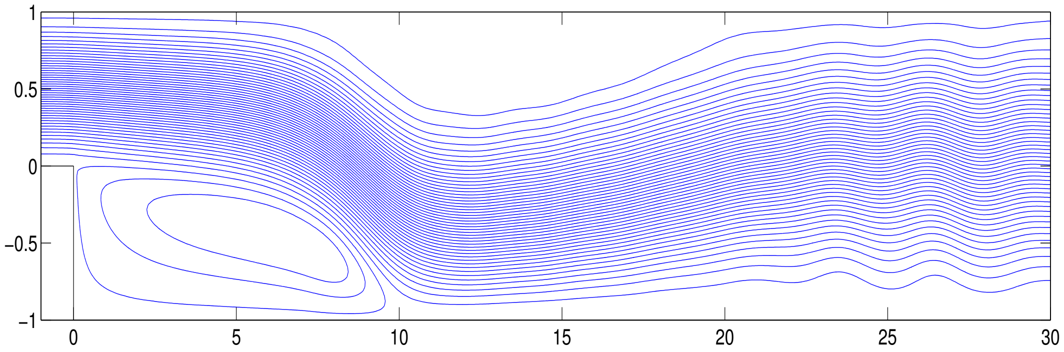

(b) Velocity streamlines at $t = 200.28$

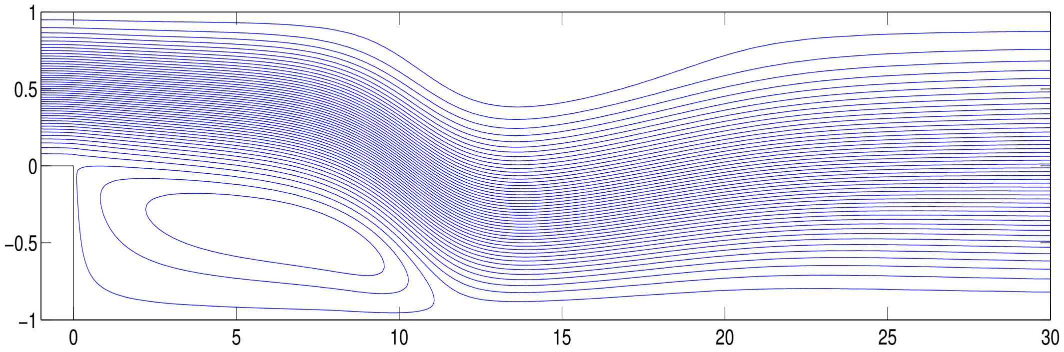

(c) Velocity streamlines at $t = 449.07$

Figure 5.3: Velocity streamlines generalized by stabilized $Q_1 - P_0$ with $\beta = \frac{1}{4}\nu$ (long time).

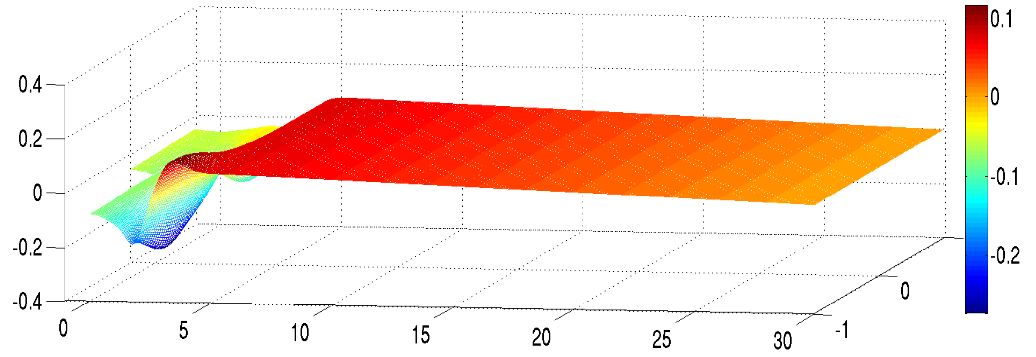

(a) Pressure at $t = 10.15$

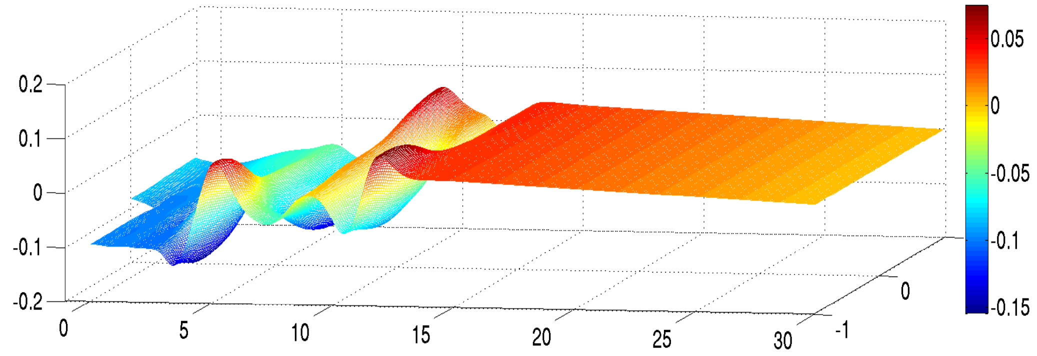

(b) Pressure at $t = 30.04$

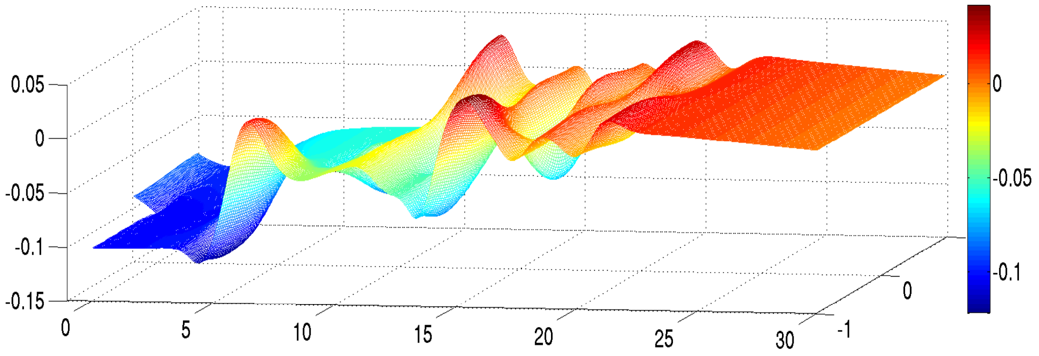

(c) Pressure at $t = 50.03$

Figure 5.4: Pressure generalized by stabilized $Q_1 - P_0$ with $\beta = \frac{1}{4}\nu$ (early time).

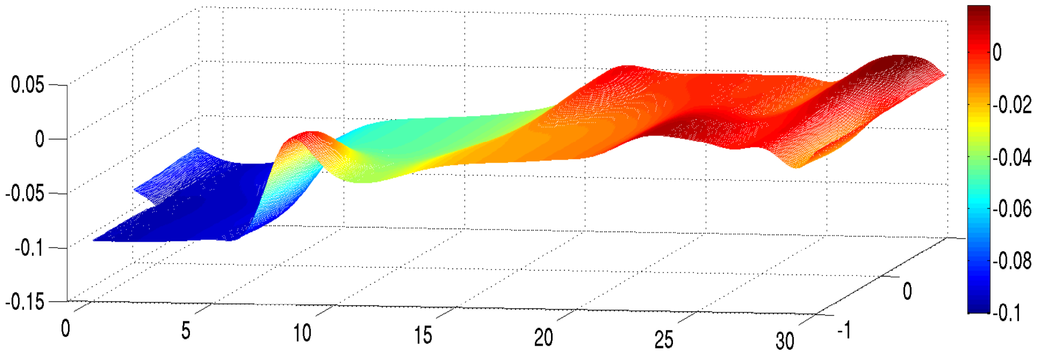

(a) Pressure at $t = 100.20$

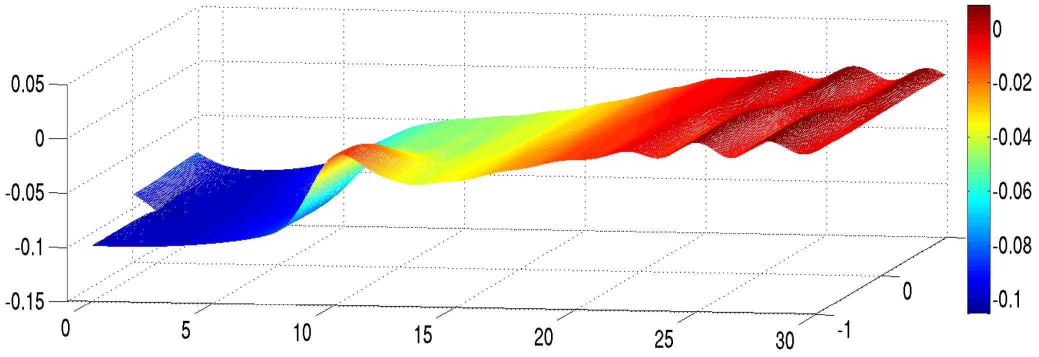

(b) Pressure at $t = 200.28$

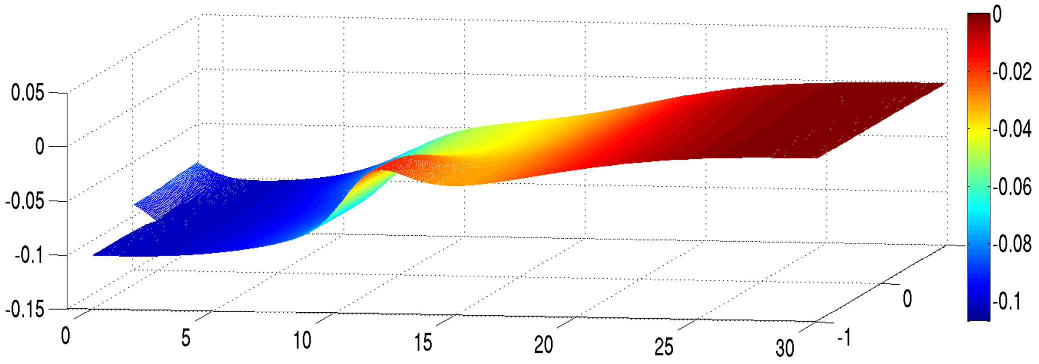

(c) Pressure at $t = 449.07$

Figure 5.5: Pressure generalized by stabilized $Q_1 - P_0$ with $\beta = \frac{1}{4}\nu$ (long time).

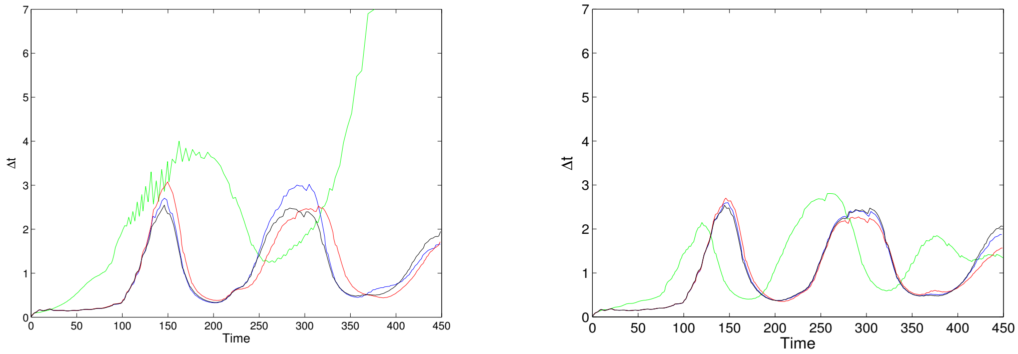

(a) time steps (coarse mesh) (b) time steps (fine mesh)

Figure 5.6: Time step evaluation: black is $Q_2 - P_{-1}$; blue is stabilized $Q_1 - P_0$ with $\beta = \frac{1}{4}\nu$; red is $Q_1 - P_0$ with $\beta = \frac{1}{4}$; green is $Q_1 - P_0$ with $\beta = \frac{1}{4\nu}$.

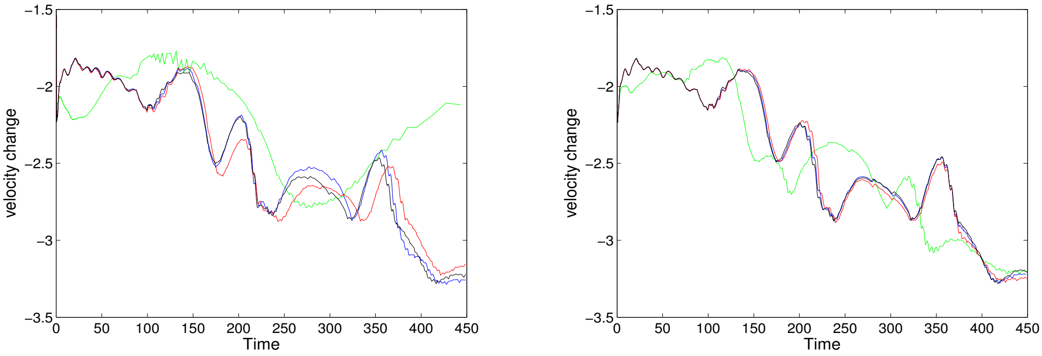

(a) $\log_{10}\frac{\|\vec{u}_h^{n+1}-\vec{u}_h^{n}\|_0}{\|\vec{u}_h^{n+1}\|_0}$ (coarse mesh) (b) $\log_{10}\frac{\|\vec{u}_h^{n+1}-\vec{u}_h^{n}\|_0}{\|\vec{u}_h^{n+1}\|_0}$ (fine mesh)

Figure 5.7: Velocity changes computed by the four methods.

with $\beta = \frac{1}{4\nu}$ goes up at the end of the time interval. Moreover, by comparing Fig. 5.6 and Fig. 5.7, the velocity changes are almost independent of the time steps—larger time steps do not lead to obviously larger velocity changes, except the green curve in Fig. 5.7(a). This reveals that the adaptive time stepping is effective.

Finally, the kinetic energy is shown in Fig. 5.8. The kinetic energies computed by all four methods seem to be quite similar. This suggests that the kinetic energy is a relatively insensitive measure of the spatial accuracy.

5.2.5 Separation eddies

From Fig. 5.3(a), we see that two major separation bubbles exist in the flow field (the lower eddy and the upper eddy). In this section, the lengths of the two eddies are evaluated.

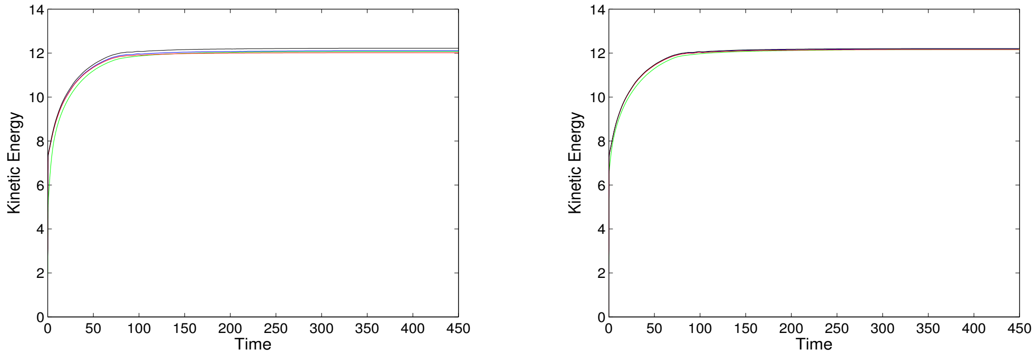

(a) $\|\vec{u}_h^n\|_0^2$ (coarse mesh) (b) $\|\vec{u}_h^n\|_0^2$ (fine mesh)

Figure 5.8: Kinetic energies computed by the four methods.

First, for each x grid value x_k (also, y_k denotes a y grid value), some notation is required,

$$u^{up}_{min,x_k} = \min_{y_k}\{u(x, y_k)|\ x = x_k, 0 < y_k < 1\}, \tag{5.17}$$

$$u^{low}_{min,x_k} = \min_{y_k}\{u(x, y_k)|\ x = x_k, -1 < y_k < 0\}, \tag{5.18}$$

and

$$x^{up}_{in} = \{x_k|\ u^{up}_{min,x_k} < 0\}, \tag{5.19}$$

$$x^{low}_{in} = \{x_k|\ u^{low}_{min,x_k} < 0\}, \tag{5.20}$$

where x^{up}_{in} and x^{low}_{in} are the x grids inside of the upper and lower eddies. For the upper eddy, the starting point is defined by the x grid value which is just smaller than $\min\{x^{up}_{in}\}$ and the reattachment point is $\max\{x^{up}_{in}\}$. The distance between these two points is referred to as the length of the upper eddy. The lower eddy is assumed to start at $x = 0$ and its length is just defined by $\max\{x^{low}_{in}\}$.

This criterion to evaluate the eddy lengths is not robust. It only works, if there is no other eddy except the main upper and lower eddies. Indeed, when the flow is not close to the steady-state and some other small eddies exist, this criterion can break down. As a result, the lengths of the eddies are only evaluated for relatively large time values ($t > 210$).

Fig. 5.9 shows lengths of the eddies computed by the four approximation methods. From these pictures, when the mesh is coarse, the stabilization parameter $\beta = \frac{1}{4\nu}$ leads to quite different eddy lengths and upper eddy starting point values from that of the other methods. As the mesh is refined, the four methods behave similarly but the results for

$\beta = \frac{1}{4}\nu$ and $\beta = \frac{1}{4}$ still have a much better agreement with the $Q_2 - P_{-1}$ method than that obtained with $\beta = \frac{1}{4\nu}$.

In addition, some reference values provided by Gartling [23] by directly solving a steady-state problem for the step domain with $L_U = 0$ are presented in Table 5.1. In this table, the results of our four methods associated with the fine mesh at $t \approx 450$ are also tabulated. We see that the eddy lengths obtained from the four methods are quite close to the reference numbers. However, our results are slightly smaller than the reference numbers. This is not so surprising, since as discussed in [9], the blunt inlet channel in [23] is known to give longer separation eddy lengths when the viscosity is small.

Table 5.1: Separation eddies with the fine mesh at $t \approx 450$.

Method	Lower length	Upper start	Upper end	Upper length
Gartling [23]	12.20	9.70	20.96	11.26
$Q_2 - P_{-1}$	11.4375	9.2812	20.4375	11.1562
$Q_1 - P_0$, with $\beta = \frac{1}{4}\nu$	11.4062	9.2500	20.4375	11.1875
$Q_1 - P_0$, with $\beta = \frac{1}{4}$	11.4062	9.1562	20.3125	11.1562
$Q_1 - P_0$, with $\beta = \frac{1}{4\nu}$	11.7500	9.2812	20.3750	11.0938

5.2.6 Velocity at history points

Since the history point $\mathbf{P}_1$ is on the non-slip boundary, the velocity at this point is zero. Fig. 5.10 and Fig. 5.11 provide the time histories for u (horizontal velocity) and v (vertical velocity) at the history points $\mathbf{P}_2$ and $\mathbf{P}_3$.

In Fig. 5.10(a), the stabilized $Q_1 - P_0$ method with $\beta = \frac{1}{4}\nu$ and $\beta = \frac{1}{4}$ matches the reference solution quite well while the stabilized method with $\beta = \frac{1}{4\nu}$ is far away from it. In detail, when the time is very early ($t < 20$), the difference between the four methods is not obvious, but when the time goes to about 25, the green curve suddenly goes down while the other three curves go up rapidly. Also, at a time value t slightly larger than 50, the blue, red and black curves achieve a minimum point which is close to -0.2 while the green one is about -0.1. Moreover, in the time interval $[250, 450]$, only the green curve obviously goes up. However, once the mesh is refined (see Fig. 5.10(b)), the green curve

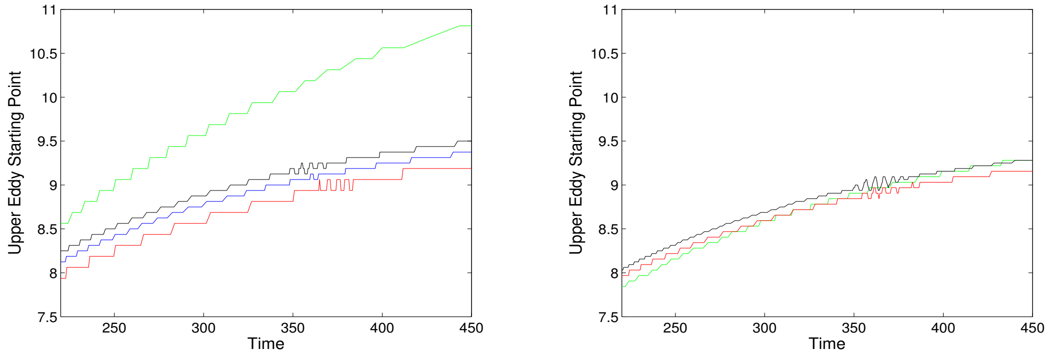

(a) Upper eddy start (coarse mesh) (b) Upper eddy start (fine mesh)

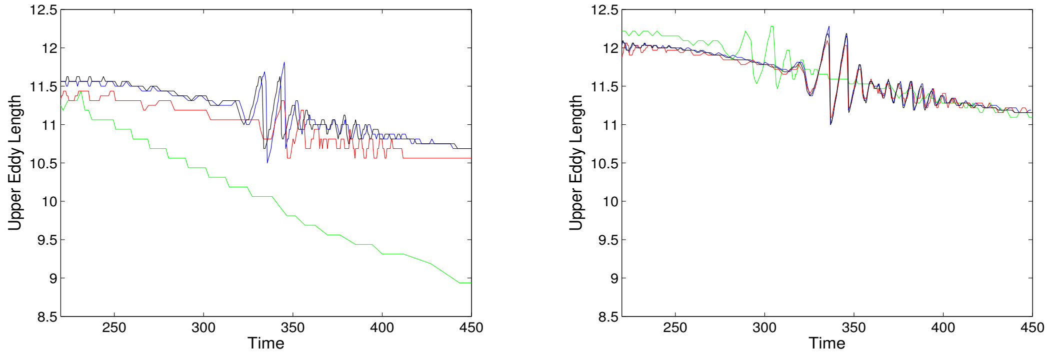

(c) Upper eddy length (coarse mesh) (d) Upper eddy length (fine mesh)

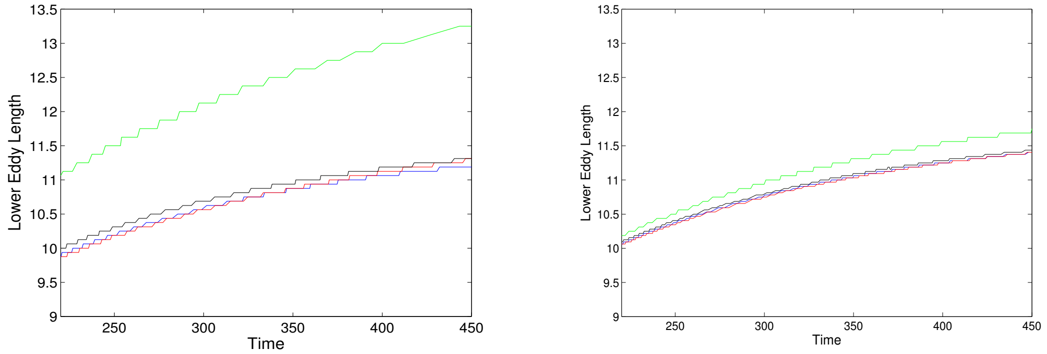

(e) Lower eddy length (coarse mesh) (f) Lower eddy length (fine mesh)

Figure 5.9: Separation bubbles: black is $Q_2 - P_{-1}$; blue is stabilized $Q_1 - P_0$ with $\beta = \frac{1}{4}\nu$; red is $Q_1 - P_0$ with $\beta = \frac{1}{4}$; green is $Q_1 - P_0$ with $\beta = \frac{1}{4\nu}$.

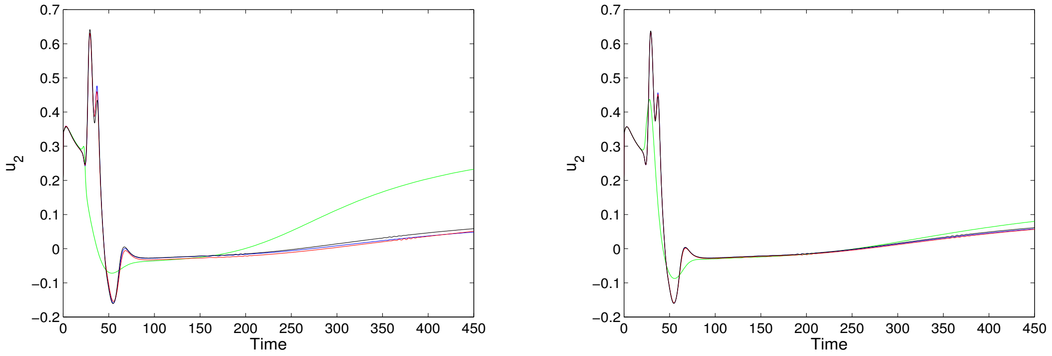

(a) u at $\mathbf{P}_2$ (coarse mesh) (b) u at $\mathbf{P}_2$ (fine mesh)

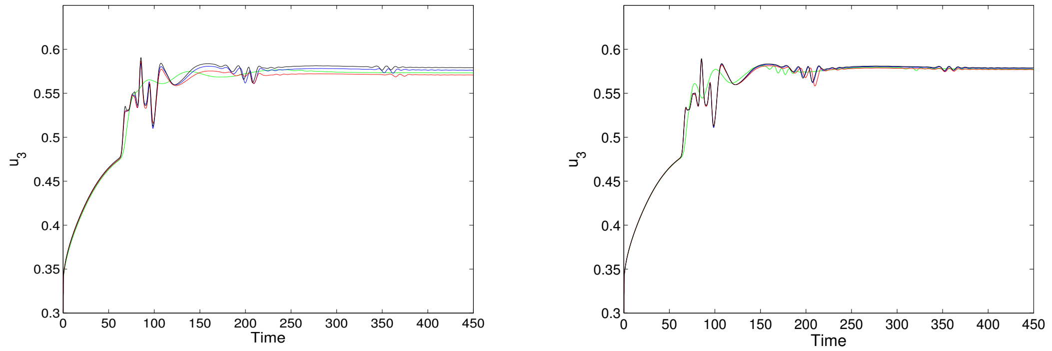

(c) u at $\mathbf{P}_3$ (coarse mesh) (d) u at $\mathbf{P}_3$ (fine mesh)

Figure 5.10: x direction velocity at history points.

is closer to the other three curves. Since $\mathbf{P}_2$ is located in the upstream portion of the upper eddy, the u velocity component should be small at the steady-state, which can be seen from Fig. 5.10(b). For $\mathbf{P}_3$, the u velocity components of the four methods are not so different. Still, it can be seen that the red and the blue curves match the black curve better.

Comparing Fig. 5.11(b) and Fig. 5.11(d), the oscillation of the v velocity component on $\mathbf{P}_3$ happens a bit later than that on $\mathbf{P}_2$. This is because the location of $\mathbf{P}_3$ is much farther from the inflow boundary than $\mathbf{P}_2$, and so the flow needs more time to reach $\mathbf{P}_3$. Since the point $\mathbf{P}_3$ is close to the outflow boundary, the v velocity there must be close to zero. This is verified in Fig. 5.11. For the choice of the stabilization parameter, $\beta = \frac{1}{4}\nu$ and $\beta = \frac{1}{4}$ again give a better agreement with the reference method than $\beta = \frac{1}{4\nu}$.

5.2.7 Pressure at history points

The pressure is a sensitive variable and it always shows the instability of mixed approximations. In other words, the main objective of stabilized methods is to make the pressure

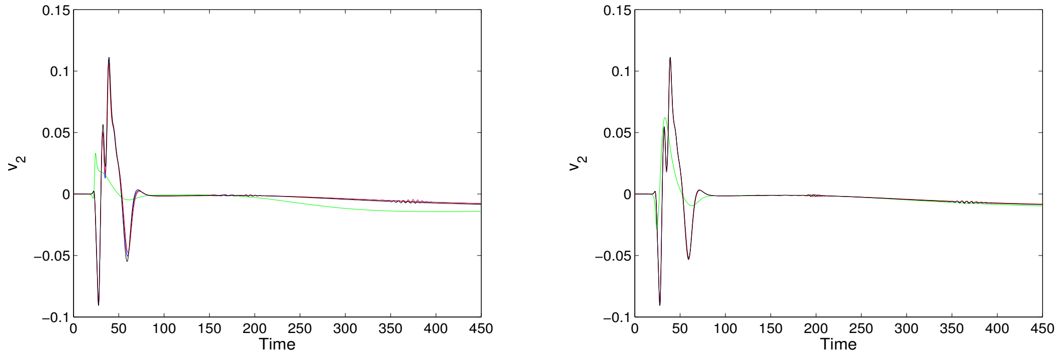

(a) v at $\mathbf{P}_2$ (coarse mesh) (b) v at $\mathbf{P}_2$ (fine mesh)

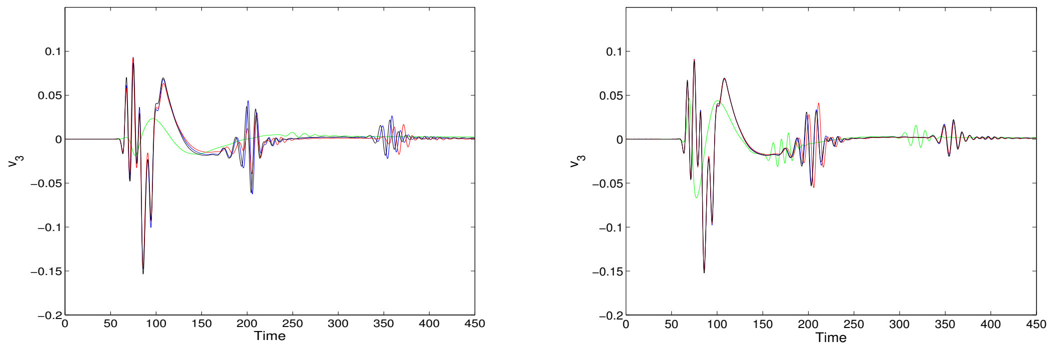

(c) v at $\mathbf{P}_3$ (coarse mesh) (d) v at $\mathbf{P}_3$ (fine mesh)

Figure 5.11: y direction velocity at history points.

approximation stable (see Section 4.3). Fig. 5.12 shows the pressure at history points. For the pressure on the step corner ($\mathbf{P}_1$) with the coarse mesh (see Fig. 5.12(a)), only the stabilized method with $\beta = \frac{1}{4}\nu$ gives a visual agreement with that of the $Q_2 - P_{-1}$ method. Once the mesh is refined (see Fig. 5.12(b)), the solution associated with $\beta = \frac{1}{4}$ also becomes quite close to the reference solution, whereas the results associated with $\beta = \frac{1}{4\nu}$ are not so close. In addition, the largest stabilization parameter forces the pressure to be too smooth. For example, in Fig. 5.12(e), at $t \approx 100$, the pressure associated with $\beta = \frac{1}{4\nu}$ is quite smooth, whereas the results computed by the other three methods show strong oscillations in time.

5.2.8 Vorticity

In fluid mechanics, the vorticity is used to measure the rotation of fluids. It is defined by the curl of the velocity, which is

$$\omega = \nabla \times \vec{u}. \tag{5.21}$$

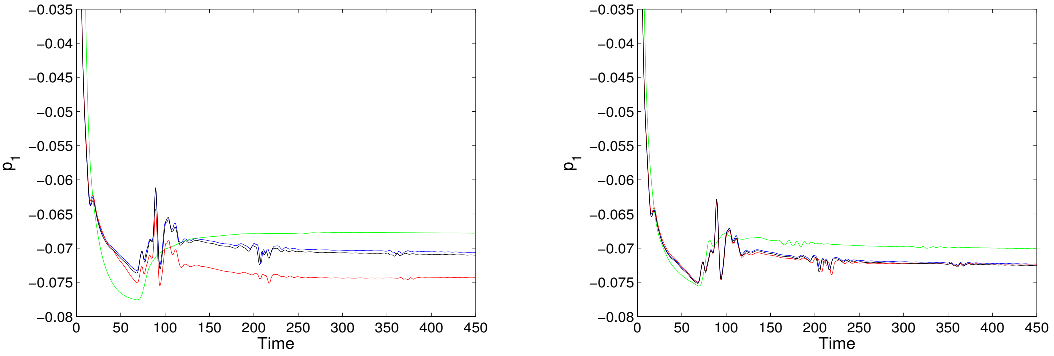

(a) Pressure at $\mathbf{P}_1$ (coarse mesh) (b) Pressure at $\mathbf{P}_1$ (fine mesh)

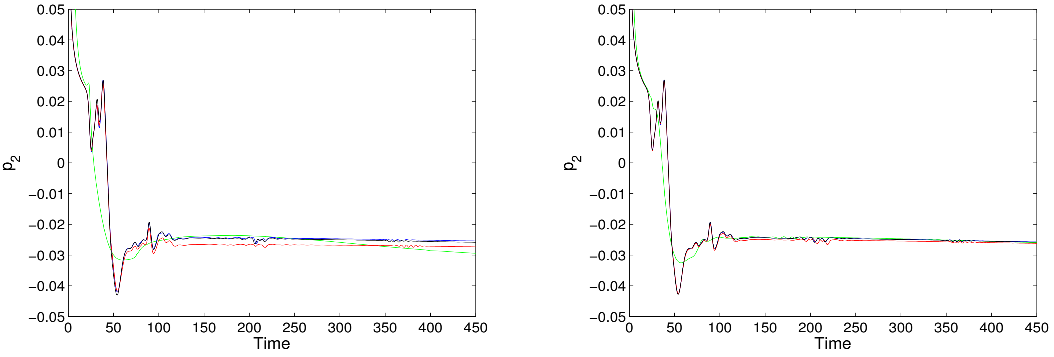

(c) Pressure at $\mathbf{P}_2$ (coarse mesh) (d) Pressure at $\mathbf{P}_2$ (fine mesh)

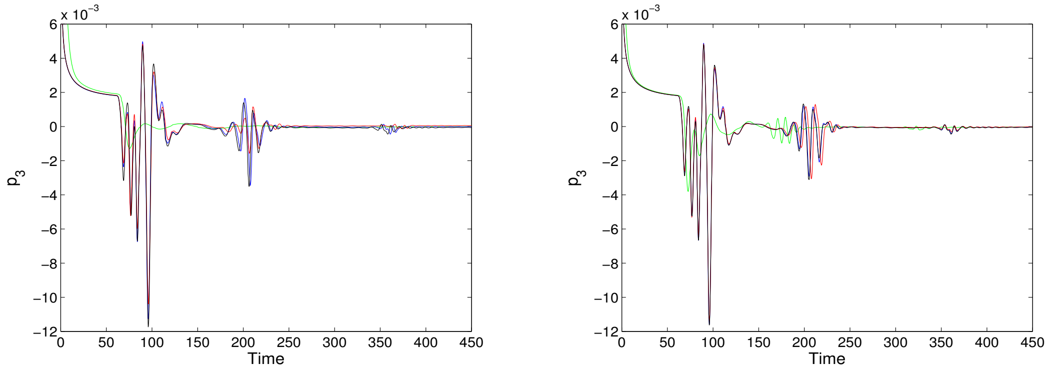

(e) Pressure at $\mathbf{P}_3$ (coarse mesh) (f) Pressure at $\mathbf{P}_3$ (fine mesh)

Figure 5.12: Pressure at history points.

In two dimensions, let $\vec{u} = (u, v)^T$ and then

$$\nabla \times \vec{u} = \frac{\partial v}{\partial x} - \frac{\partial u}{\partial y} \tag{5.22}$$

with a direction perpendicular to the two dimensional domain.

Fig. 5.13 and Fig. 5.14 show the contour lines of the vorticity computed by the stabilized $\boldsymbol{Q}_1 - \boldsymbol{P}_0$ method with $\beta = \frac{1}{4}\nu$. From Fig. 5.13(a), at $t \approx 10$, the fluid rotation around the step corner is very strong. At $t \approx 30$, it is clear that the vorticity is large in three places: the step corner, the lower eddy reattachment point and the upper eddy reattachment point. When the time becomes very large ($t \approx 450$), the vorticity contour lines seem to reach a steady-state while the main rotation of the flow is at the step corner.

In addition, the mean vorticity ω_Ω which is defined by

$$\omega_\Omega = \int_\Omega \omega, \tag{5.23}$$

is also computed. Note that, using Green's theorem,

$$\int_{\partial\Omega} \vec{u} \cdot \vec{t} = \int_\Omega \omega, \tag{5.24}$$

where $\vec{t}$ is the unit tangential direction on the boundary. Due to the boundary condition applied on this test problem, the non-trivial tangential velocity can only appear on the outflow boundary $\partial\Omega_N$. This implies that, for all $\vec{u} = (u, v)^T \in \boldsymbol{H}_E^1$,

$$\omega_\Omega = \int_{\partial\Omega_N} v. \tag{5.25}$$

From (5.25), the mean vorticity shows the outflow boundary effect. Ideally, the mean vorticity is expected to be close to zero, i.e. the outflow is close to be parallel to the x axis. In this situation, the natural condition (5.4) is valid and has the correct physical meaning—zero flow pressure on the out flow boundary. In order to achieve this goal, the downstream channel should be long enough. Gresho et al. [25] suggests that $L_D = 30$ is enough for this test problem.

The mean vorticities computed by the four approximations are shown in Fig. 5.15. From this figure, they do get close to zero (for the fine mesh, their absolute values at $t \approx 450$ are between 5×10^{-4} and 2×10^{-3}) as time goes by. In addition, it can be seen that the results of stabilized $\boldsymbol{Q}_1 - \boldsymbol{P}_0$ with $\beta = \frac{1}{4}\nu$ is the closest one to that of the $\boldsymbol{Q}_2 - \boldsymbol{P}_{-1}$ method.

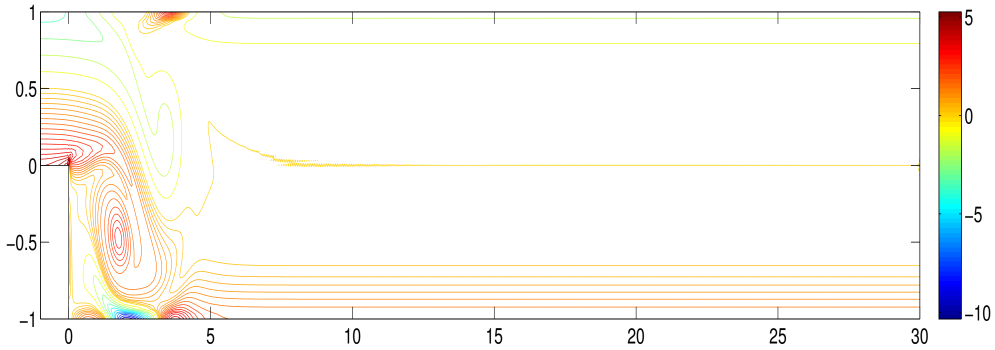

(a) Vorticity at $t = 10.15$

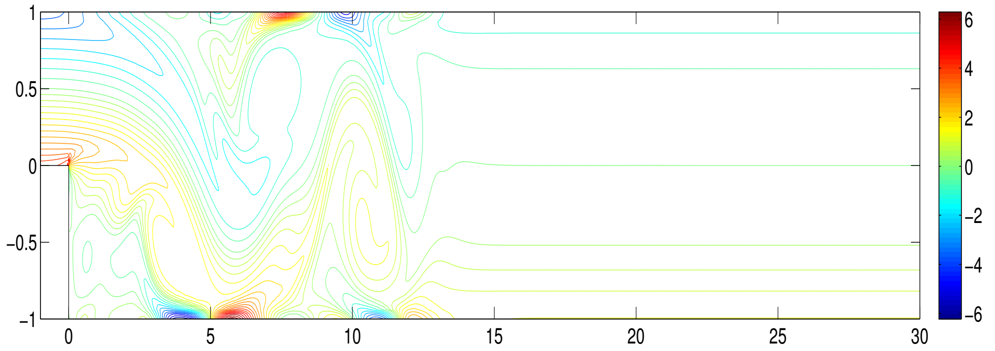

(b) Vorticity at $t = 30.04$

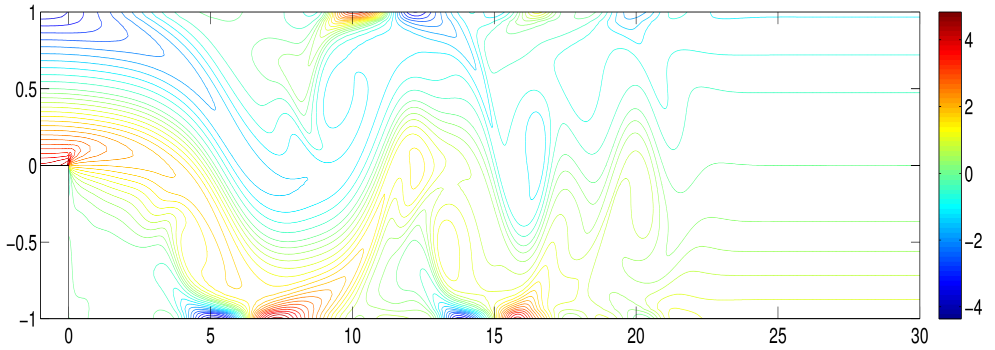

(c) Vorticity at $t = 50.03$

Figure 5.13: Vorticity generalized by stabilized $Q_1 - P_0$ with $\beta = \frac{1}{4}\nu$ (early time).

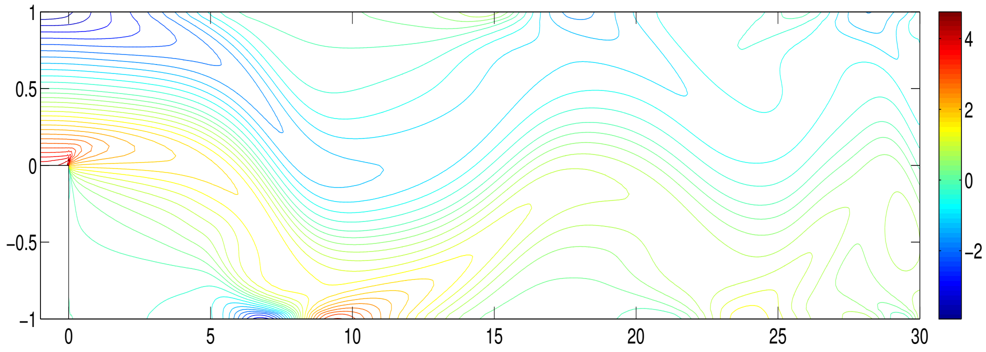

(a) Vorticity at $t = 100.20$

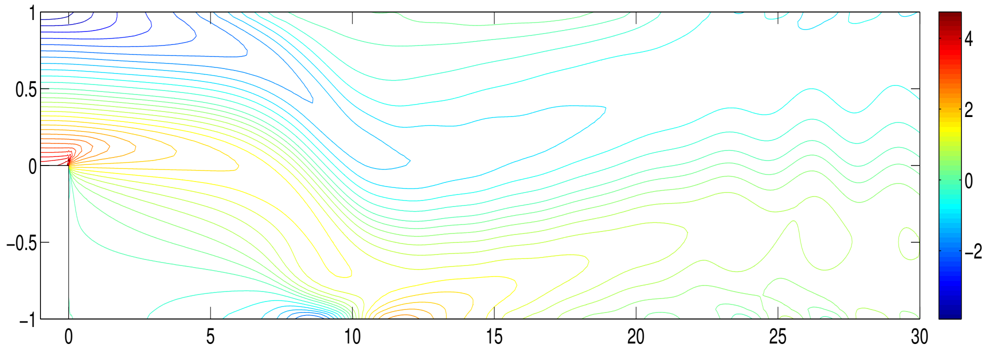

(b) Vorticity at $t = 200.28$

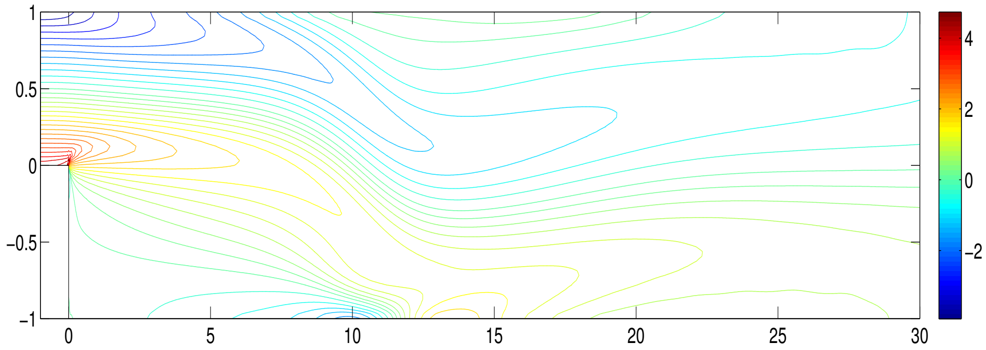

(c) Vorticity at $t = 449.07$

Figure 5.14: Vorticity generalized by stabilized $Q_1 - P_0$ with $\beta = \frac{1}{4}\nu$ (long time).

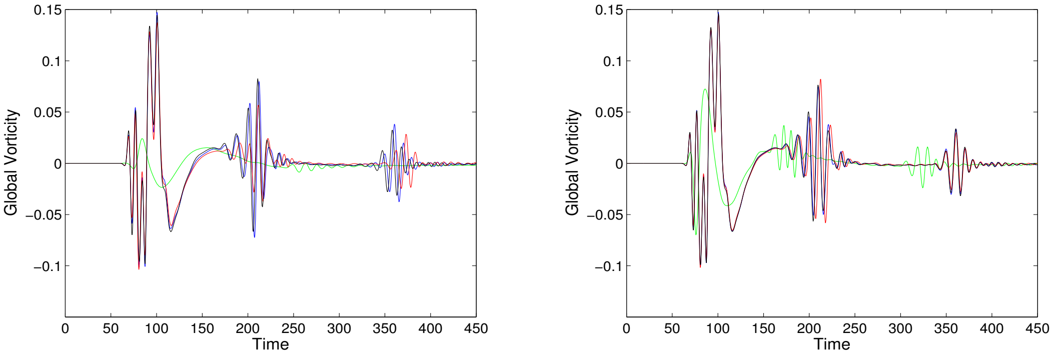

(a) ω_Ω (coarse mesh) (b) ω_Ω (fine mesh)

Figure 5.15: Mean vorticity ω_Ω.

5.3 Test Problem 2 (Periodic Flow): Flow around a Square Cylinder with $\nu = \frac{1}{300}$

The second test problem is that of flow around a square cylinder in a channel domain. This problem is shown in Fig. 5.16, where the square cylinder is located in the middle of the channel in the sense of the y direction. For the inflow (left) boundary, the following time dependent velocity $\vec{u} = (u, v)$ is applied,

$$u = (1 - e^{(-10t)})(1 + y)(1 - y), \quad v = 0,$$

a natural boundary condition is applied for the right boundary, and the other boundaries are non-slip non-permeation boundaries. The viscosity of this test problem is set to be $\frac{1}{300}$ and from Sharma and Eswaran [41], the solution of this test problem is known to be periodic for $80 < \nu < 320$.

In order to check the performance of the four finite element methods, the drag and lift coefficients are computed. The definitions of the drag coefficient C_d and the lift coefficient C_l are as follows,

$$C_d = \int_S (\nu \frac{\partial u_{t_s}}{\partial n} n_y - p n_x), \quad C_l = -\int_S (\nu \frac{\partial u_{t_s}}{\partial n} n_x + p n_y), \tag{5.26}$$

where S is the surface of the cylinder, $\vec{n} = (n_x, n_y)^T$ is the normal vector on S, $t_s = (n_y, -n_x)^T$ is the tangential vector and u_{t_s} is the tangential velocity.

Two kinds of meshes are tested for this problem. The first one is a uniform mesh—for the $Q_2 - P_{-1}$ approximation, it is the uniform mesh with $h = \frac{1}{8}$ (1008 rectangles) while for

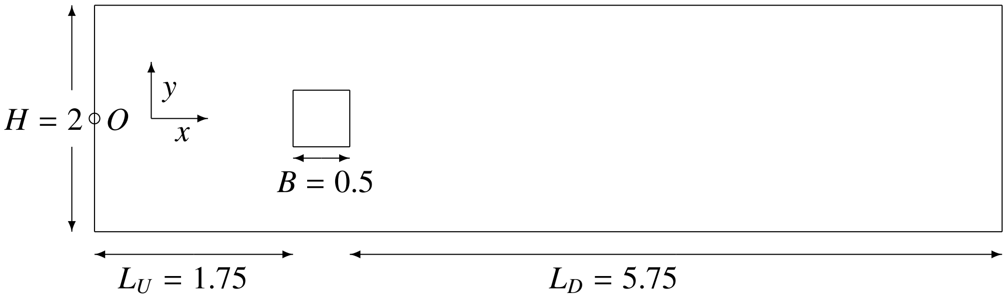

Figure 5.16: A square cylinder in a channel.

the $Q_1 - P_0$ approximation, the uniform mesh is obtained by refining the mesh for $Q_2 - P_{-1}$ once. The second one for the $Q_2 - P_{-1}$ approximation is a stretched mesh which is shown in Fig. 5.17 containing 2826 elements, while the stretched mesh for $Q_1 - P_0$ approximation is also obtained by refining it once. The stretched mesh should provide much more accurate drag and lift coefficients than the uniform mesh.

5.3.1 Numerical results

Fig. 5.18 shows the time steps of the four methods associated with both kinds of meshes. It can be seen that, the time steps of the stabilized method with $\beta = \frac{1}{4\nu}$ are much larger than the other methods. This implies, the solution associated with $\beta = \frac{1}{4\nu}$ reaches a steady-state which is not expected.

Fig. 5.19 shows the drag coefficients. For the uniform mesh, the four methods generate obviously different drag coefficients. Once the mesh is switched to the stretched mesh, $Q_2 - P_{-1}$ and stabilized $Q_1 - P_0$ with $\beta = \frac{1}{4}\nu$ provide very close values. In detail, from Fig. 5.19(d), the black curve and the blue curve have similar oscillation amplitudes and frequencies. The black one oscillates between 0.78 and 0.79, while the blue one oscillates between 0.79 and 0.80, which implies their difference is less than 3% of their magnitudes.

Fig. 5.20 shows the lift coefficients. From this figure, it is obvious that the lift coefficients of stabilized $Q_1 - P_0$ with $\beta = \frac{1}{4}\nu$ is the closest to that of the $Q_2 - P_{-1}$ method. The largest parameter $\beta = \frac{1}{4\nu}$ only provides a steady-state solution, while the lift coefficient associated with the medium parameter $\beta = \frac{1}{4}$ goes down as the time value increases, which all contradict the true solution (which should be purely periodic).

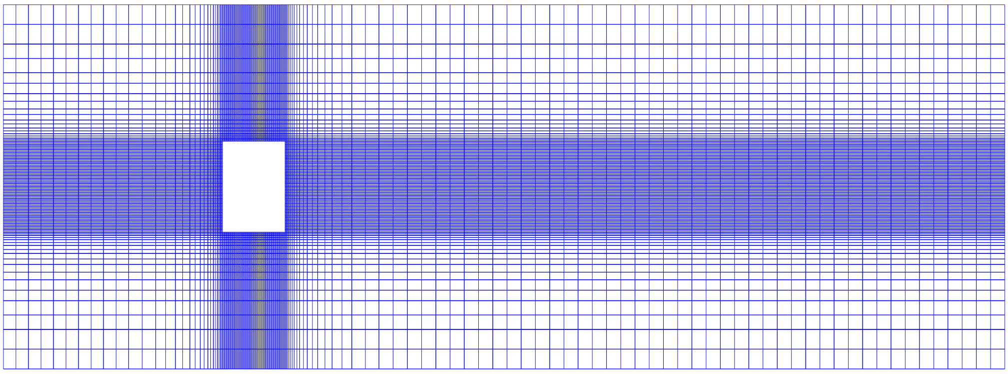

Figure 5.17: A stretched mesh with 2826 rectangles.

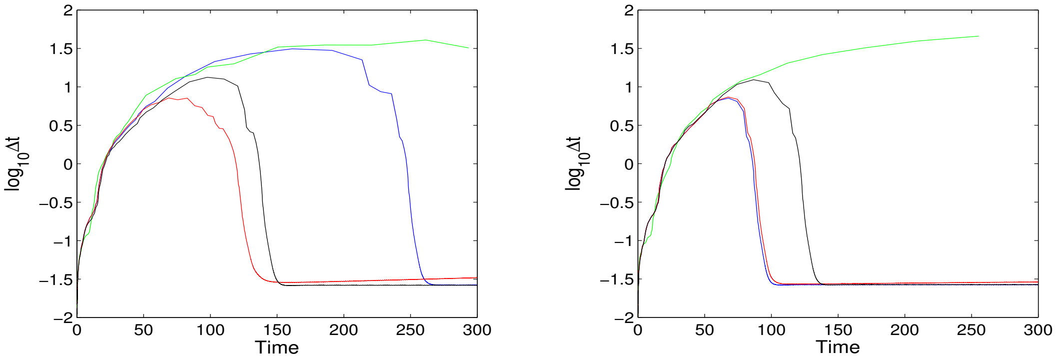

(a) Time steps (uniform mesh)

(b) Time steps (stretched mesh)

Figure 5.18: Time steps for the four finite element methods, test problem 2.

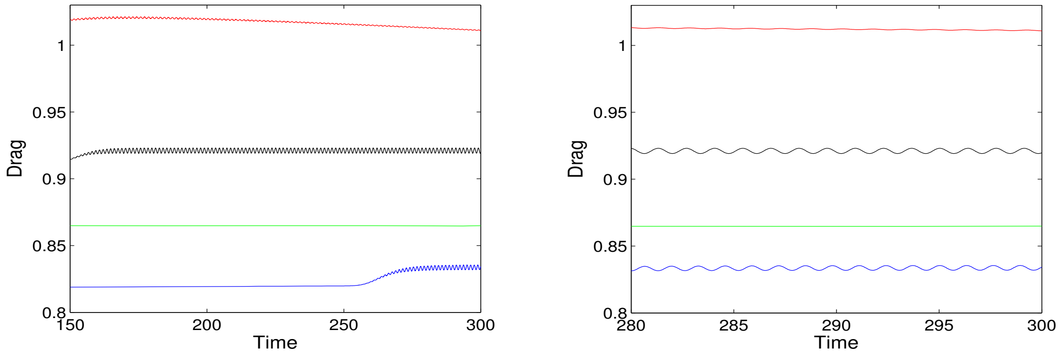

(a) Drag coefficients (uniform mesh) (b) Drag (uniform mesh), Zoom in.

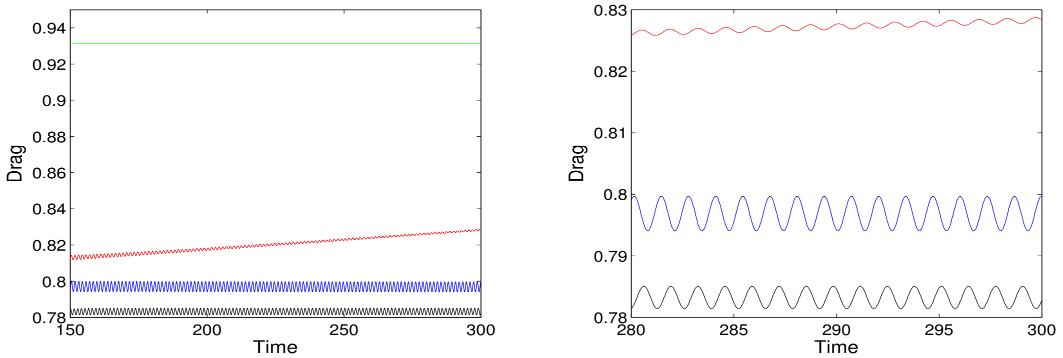

(c) Drag coefficients (stretched mesh) (d) Drag (stretched mesh), Zoom in.

Figure 5.19: Drag coefficients.

Finally, the periods of the lift and drag coefficients are computed, which are used to define the Strouhal number in fluid mechanics. In this chapter, a period is defined by the length of the time interval between two local minima of the oscillation quantities. In Tables 5.2 and 5.3, N implies the average of the last N periods up to the final time. Note that since stabilized $Q_1 - P_0$ with $\beta = \frac{1}{4\nu}$ leads to a steady-state solution, no period is given for this method. From both tables, the averages of the last 5 and 10 periods are not significantly different. Looking at Table 5.3, for the stretched mesh, the periods generated by stabilized $Q_1 - P_0$ with $\beta = \frac{1}{4}\nu$ are very close to that of $Q_2 - P_{-1}$.

5.4 Summary and Conclusions

In this chapter, the stabilized $Q_1 - P_0$ approximation is applied to the time dependent Navier-Stokes equations solved with the adaptive TR time stepping method introduced in [29]. The numerical experiments are performed on two test problems:

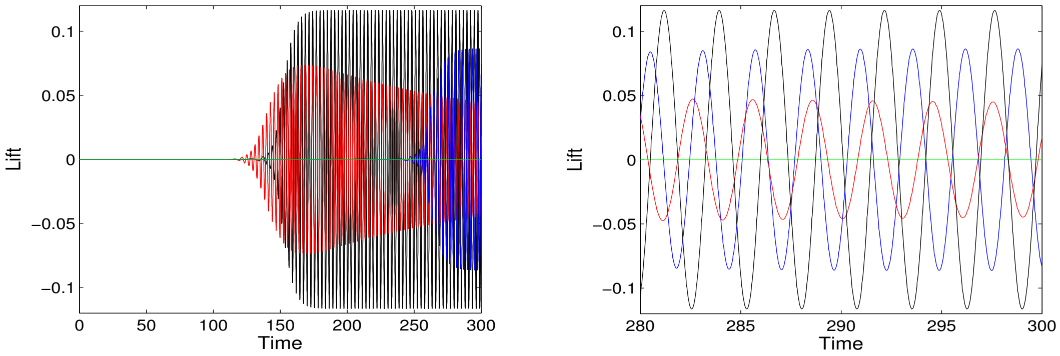

(a) Lift coefficients (uniform mesh) (b) Lift (uniform mesh), Zoom in.

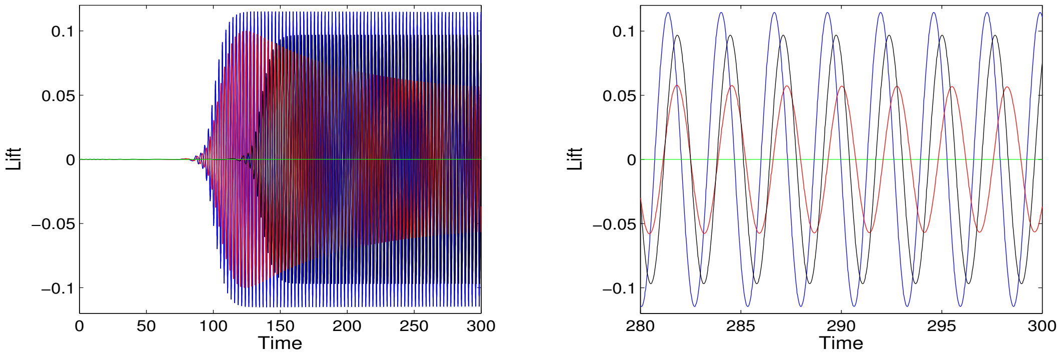

(c) Lift coefficients (stretched mesh) (d) Lift (stretched mesh), Zoom in.

Figure 5.20: Lift coefficients.

Table 5.2: Periods of the drag and lift coefficients on the uniform mesh.

Method	Drag $N = 5$	Drag $N = 10$	Lift $N = 5$	Lift $N = 10$
$\boldsymbol{Q}_2 - \boldsymbol{P}_{-1}$	1.3723	1.3710	2.7447	2.7434
$\boldsymbol{Q}_1 - \boldsymbol{P}_0$, with $\beta = \frac{1}{4}\nu$	1.3072	1.3072	2.6143	2.6099
$\boldsymbol{Q}_1 - \boldsymbol{P}_0$, with $\beta = \frac{1}{4}$	1.4938	1.4940	2.9895	2.9823
$\boldsymbol{Q}_1 - \boldsymbol{P}_0$, with $\beta = \frac{1}{4\nu}$	N/A	N/A	N/A	N/A

Table 5.3: Periods of the drag and lift coefficients on the stretched mesh.

Method	Drag $N = 5$	Drag $N = 10$	Lift $N = 5$	Lift $N = 10$
$\boldsymbol{Q}_2 - \boldsymbol{P}_{-1}$	1.3203	1.3177	2.6354	2.6354
$\boldsymbol{Q}_1 - \boldsymbol{P}_0$, with $\beta = \frac{1}{4}\nu$	1.3226	1.3226	2.6451	2.6464
$\boldsymbol{Q}_1 - \boldsymbol{P}_0$, with $\beta = \frac{1}{4}$	1.3693	1.3708	2.7421	2.7366
$\boldsymbol{Q}_1 - \boldsymbol{P}_0$, with $\beta = \frac{1}{4\nu}$	N/A	N/A	N/A	N/A

- steady flow in the step domain with viscosity $\nu = \frac{1}{600}$;
- unsteady periodic flow around a square cylinder in a channel with $\nu = \frac{1}{300}$.

In these two test problems, the flow fields generated by the stabilized $\boldsymbol{Q}_1 - \boldsymbol{P}_0$ approximation and the $\boldsymbol{Q}_2 - \boldsymbol{P}_{-1}$ approximation are compared by computing some important flow quantities, such as the separation eddy lengths, velocity and pressure history point values, and the drag and lift coefficients.

Based on these numerical experiments, when $\nu = O(10^{-2})$, the best choice of stabilization parameter for stabilized $\boldsymbol{Q}_1 - \boldsymbol{P}_0$ approximation (5.11)–(5.12) is

$$\beta = \frac{1}{4}\nu. \tag{5.27}$$

Some other numerical experience (not reported here) reveals that the unstabilized $\boldsymbol{Q}_1 - \boldsymbol{P}_0$ approximation (that is with $\beta = 0$) has a strong pressure instability when the viscosity is large, while if the viscosity becomes small, the instability decreases. This also supports our conclusion that $\beta = \frac{1}{4}\nu$ is the right choice, because it avoids over-stabilizing the pressure approximation.

Chapter 6

Open Questions

Looking to the future, we are left with some open questions that arise from the material in the thesis.

- How to find the points where the spatial discretization error is relatively small?
- How to establish the upper and lower bounds (see (2.14)–(2.15) or (3.12)–(3.13)) for local problem error estimators in a more direct way rather than showing their equivalence to residual estimators?
- How to derive reliable bounds of local problem estimators for the Stokes problem associated with anisotropic meshes?

The first question is the foundation of local problem estimators. When solving local error equations (see Chapter 2), zero values need to be set at the points where the error is relatively small. However, most papers discussing pointwise errors typically focus on the natural pointwise superconvergence, which we do not necessarily need. Although the error at superconvergence points is definitely small, the error at some other points may also be relatively small. So, it is of interest to find these non-superconvergence points with small discretization errors.

From the numerical experiments in Chapters 2 and 3, the local problem error estimators are more effective than the residual estimators. However, the standard analysis techniques do not capture this advantage—the upper and lower bounds of local problem estimators are typically established by showing their equivalence to residual error estimators. So, it would be interesting to establish the bounds in a more direct way. In addition, although using the saturation assumption (see Section 4.4.1) is one route to achieve this goal, we should try to avoid this assumption, since it does not always hold.

The numerical example in Section 4.4.2 shows that our new local problem estimator can provide a reliable upper bound for the stabilized $Q_1 - P_0$ approximation. However, with the standard analysis techniques it is hard to make progress in establishing the upper and lower bounds, since residual estimators for mixed approximations associated with anisotropic meshes have not been successfully established (see Section 4.4.1). So, the resolution of the second question is also key to solving the third question—that is to derive the bounds for local problem estimators directly.

Bibliography

[1] M. Ainsworth and P. Coggins, *The stability of mixed hp-finite element methods for Stokes flow on high aspect ratio elements*, SIAM J. Numer. Anal., 38 (2000), pp. 1721–1761.

[2] M. Ainsworth and D. Kelly, *A posteriori error estimators and adaptivity for finite element approximation of the non-nomogeneous dirichlet problem*, Advances in Computational Mathematics, 15 (2001), pp. 3–23.

[3] M. Ainsworth and J. Oden, *A posteriori error estimates for Stokes' and Oseen's equations*, SIAM J. Numer. Anal., 34 (1997), pp. 228–245.

[4] T. Apel, *Anisotropic Finite Elements: Local Estimation and Applications*, B.G.Teubner Stuttgart·Leipzig, Germany, 1999.

[5] T. Apel and H. Randrianarivony, *Stability of discretizations of the Stokes problem on anisotropic meshes*, Math. Comput. Simulation, 61 (2003), pp. 437–447.

[6] R. Bank and A. Weiser, *Some a posteriori error estimators for elliptic partial differential equations*, Math. Comp., 44 (1985), pp. 283–301.

[7] R. Bank and B. Welfert, *A posteriori error estimates for the Stokes problem*, SIAM J. Numer. Anal., 28 (1991), pp. 591–623.

[8] G. Barrenecheaa and J. Blasco, *Pressure stabilization of finite element approximations of time-dependent incompressible flow problems*, Comput. Methods Appl. Mech. Engrg., 197 (2007), p. 219231.

[9] I. Barton, *The entrance effect of laminar flow over a backward-facing step geometry*, Int. J. Numer. Meth. Fluids, 25 (1997), pp. 633–644.

[10] R. Becker, *An Adaptive Finite Element Method for the Incompressible Navier-Stokes Equations on Time-dependent Domains*, Ph.D thesis, Ruprecht-Karls-Universität Heidelberg, 1995.

[11] P. Bochev, M. Gunzburger, and R. Lehoucq, *On stabilized finite element methods for the Stokes problem in the small time step limit*, Int. J. Numer. Meth. Fluids, 53 (2007), pp. 573–597.

[12] D. Braess, *Finite Elements*, Cambridge University Press, London, 1997.

[13] E. Burman and M. Fernández, *Galerkin finite element methods with symmetric pressure stabilization for the transient Stokes equations: Stability and convergence analysis*, SIAM J. Numer. Anal., 47 (2008), pp. 409–439.

[14] E. Burman, M. Fernández, and P. Hansbo, *Continuous interior penalty finite element method for oseen's equations*, SIAM J. Numer. Anal., 44 (2006), pp. 1248–1274.

[15] E. Chizhonkov and M. Olshanskii, *On the domain geometry dependence of the LBB condition*, M2AN, 34 (2000), pp. 935–951.

[16] P. Clément, *Approximation by finite element functions using local regularization*, R.A.I.R.O. Anal. Numér., 2 (1975), pp. 77–84.

[17] E. Creusé, G. Kunert, and S. Nicaise, *A posteriori error estimation for the Stokes problem: Anisotropic and isotropic discretizations*, M3AS, 14 (2004), pp. 1297–1341.

[18] J. Douglas and J. Wang, *An absolutely stabilized finite element method for the Stokes problem*, Math. Comp., 52 (1989), pp. 495–508.

[19] D. Dunavant, *High degree efficient symmetrical gaussian quadrature rules for the triangle*, Int. J. Numer. Meth. Eng., 21 (1985), pp. 1129–1148.

[20] H. Elman, A. Ramage, and D. Silvester, *Algorithm 866: IFISS, a matlab toolbox for modelling incompressible flow*, ACM Trans. Math. Soft., 33 (2007), pp. 2–14.

[21] H. Elman, D. Silvester, and A. Wathen, *Finite Elements and Fast Iterative Solvers*, Oxford University Press, New York, 2005.

[22] L. Franca and T. Hughes, *Convergence analyses of galerkin least-squares methods for symmetric advective-diffusive forms of the Stokes and incompressible Navier-Stokes equations*, Comput. Methods Appl. Mech. Engrg., 105 (1993), pp. 285–298.

[23] D. Gartling, *A test problem for outflow boundary conditions - flow over a backward-facing step*, Int. J. Numer. Meth. Fluids, 11 (1990), pp. 953–967.

[24] V. Girault and P. Raviart, *Finite Element Methods for Navier-Stokes Equations*, Springer-Verlag, Berlin, 1986.

[25] P. Gresho, D. Gartling, J. Torczynski, K. Cliffe, K. Winters, T. Garratt, A. Spence, and J. Goodrich, *Is the steady viscous incompressible 2d flow over a backward facing step at re=800 stable?*, Int. J. Numer. Meth. Fluids, 17 (1993), pp. 501–541.

[26] M. Heil and A. Hazel, *Oomph-lib–an object-oriented multi-physics finite-element library*, Lect. Notes Comput. Sci. Eng., 53 (2006), pp. 19–49.

[27] P. Houston, D. Schötzau, and T. Wihler, *hp-adaptive discontinuous Galerkin finite element methods for the Stokes problem*, in Proceedings of the European Congress on Computational Methods in Applied Sciences and Engineering, P. Neittaanmäki, T. Rossi, S. Korotov, E. Oñate, J. Périaux, and D. Knörzer, eds., vol. II, 2004.

[28] T. Hughes and L. Franca, *A new finite element formulation for computational fluid dynamics: Vii. the Stokes problem with various well-posed boundary conditions: Symmetric formulations that converge for all velocity/pressure spaces*, Comput. Methods Appl. Mech. Engrg., 65 (1987), pp. 85–96.

[29] D. Kay, P. Gresho, D. Griffiths, and D. Silvester, *Adaptive time-stepping for incompressible flow part ii: Navier-Stokes equations*, SIAM J. Sci. Comput., 32 (2010), pp. 111–128.

[30] D. Kay and D. Silvester, *A posteriori error estimation for stabilized mixed approximations of the Stokes equations*, SIAM J. Sci. Comput., 21 (1999), pp. 1321–1336.

[31] N. Kechkar and D. Silvester, *Analysis of locally stabilized mixed finite element methods for the Stokes problem*, Math. Comp., 58 (1992), pp. 1–10.

[32] Q. Liao and D. Silvester, *A simple yet effective a posteriori estimator for classical mixed approximation of Stokes equations*, Appl. Numer. Math., pp. to appear, doi:10.1016/j.apnum.2010.05.003.

[33] R. Lin, *Natural superconvergence in two and three dimensional finite element methods*, PhD thesis, Wayne State University, 2005.

[34] R. Lin and Z. Zhang, *Natural superconvergent points of triangular finite elements*, Numer. Meth. Part. Diff. Equations, 20 (2004), pp. 864–906.

[35] ——, *Numerical study of natural superconvergence in least-squares finite element methods for elliptic problems*, Appl. Math., 54 (2004), pp. 251–266.

[36] R. Nochetto, *Removing the saturation assumption in a posteriori error analysis*, Istit. Lombardo Accad. Sci. Lett. Rend. A, 127 (1993), pp. 67–82.

[37] M. Randrianarivony, *Anisotropic finite elements for the Stokes problem: a posteriori error estimator and adaptive mesh*, J. Comput. Appl. Math., 169 (2004), pp. 255–275.

[38] R. Rannacher and S. Turek, *Simple nonconforming quadrilateral Stokes element*, Numer. Meth. Part. Diff. Equations, 8 (1992), pp. 97–111.

[39] D. Schötzau and C. Schwab, *Mixed hp-finite element methods on anisotropic meshes*, Math. Methods Appl. Sci., 8 (1998), pp. 787–820.

[40] D. Schötzau, C. Schwab, and R. Stenberg, *Mixed hp-FEM on anisotropic meshes II: Hanging nodes and tensor products of boundary layer meshes*, Numer. Math., 83 (1999), pp. 667–697.

[41] A. Sharma and V. Eswaran, *Heat and fluid flow across a square cylinder in the two-dimensional laminar flow regime*, Num. Heat Transfer, Part A 45 (2004), pp. 247–269.

[42] D. Silvester, *Optimal low order finite element methods for incompressible flow*, Comput. Methods Appl. Mech. Engrg., 111 (1994), pp. 357–368.

[43] D. Silvester, H. Elman, and A. Ramage, *Incompressible Flow and Iterative Solver Software (IFISS) version 3.0, Released 31 December 2009.* `http://www.manchester.ac.uk/ifiss`.

[44] S. Turek, *Efficient Solvers for Incompressible Flow Problems*, Springer-Verlag, 1999.

[45] R. Verfürth, *A posteriori error estimators for the Stokes equations*, Numer. Math., 55 (1989), pp. 309–325.

[46] ——, *A posteriori error estimation and adaptive mesh-refinement techniques*, J. Comput. Appl. Math., 50 (1994), pp. 67–83.

[47] ——, *A Review of A Posteriori Error Estimation and Adaptive Mesh-Refinement Techniques*, Wiley–Teubner, Chichester, 1996.

[48] O. Zienkiewicz and J. Zhu, *The superconvergent patch recovery and a posteriori error estimates*, Int. J. Numer. Meth. Eng., 33 (1992), pp. 1331–1364.

Appendix A

MATLAB Functions

The new error estimators for rectangle elements introduced in Chapters 2 and 3 are implemented in version 3.1 of IFISS [1]. The functions arising from this thesis are the following:

- **diffpost_q2_with_q4** computes the Q_4 estimator for the Q_2 approximation. The level of reduction can be specified by users, with the default being Level c (see Section 2.3.3);
- **stokespost_q2p1** computes local Poisson error estimator for the $Q_2 - P_{-1}$ approximation for the steady-state Stokes equations with the Q_3 correction space;
- **stokespost_q2q1** computes local Poisson error estimator for the $Q_2 - Q_1$ approximation for the steady-state Stokes equations with the Q_3 correction space;
- **navierpost_q2p1** computes local Poisson error estimator for the $Q_2 - P_{-1}$ approximation for the steady-state Navier-Stokes equations with the Q_3 correction space;
- **navierpost_q2q1** computes local Poisson error estimator for the $Q_2 - Q_1$ approximation for the steady-state Navier-Stokes equations with the Q_3 correction space.

The triangular version of IFISS (TIFISS 1.0) is currently being developed. We hope to release it before the end of 2010.

---

[1] This is due to be released in November 2010.